PASSIVE GAMMA SOURCE IMAGING

USING COMPRESSED SENSING PRINCIPLES

A Dissertation

by

NURASLINDA BINTI ANUAR

Submitted to the Office of Graduate and Professional Studies of
Texas A&M University
in partial fulfillment of the requirements for the degree of

DOCTOR OF PHILOSOPHY

Chair of Committee,	Craig Marianno
Committee Members,	Sunil Chirayath
	Ryan McClarren
	Krishna Narayanan
Head of Department,	Michael Nastasi

December 2021

Major Subject: Nuclear Engineering

ABSTRACT

A design concept for imaging radiation sources using compressed sensing (CS) principles was developed in this research. A proof-of-concept system model was designed using Monte Carlo N-Particle (MCNP) simulations. The resulting conceptual system comprised a collimator made of 11×11 polyvinyl chloride (PVC) pipes placed upright in the middle of a 250-gallon water-filled rectangular tank, and a detection system that consisted of six Geiger-Muller (GM) detectors. The collimator channels were modeled to be randomly filled with water or air to provide different measurement configurations. Image reconstructions were performed using l_1-minimization and non-negative least squares (NNLS) methods for four cases with varying ^{137}Cs source locations. Localization and shape identification were shown to be successful for a point source and ring-shaped sources using data from MCNP simulations. The NNLS method was selected to be applied in image reconstruction for model validation. The proof-of-concept system was physically assembled for collection of measurement data. Model validation with experimental measurements was performed by first refining the GM detector modeling. New methods of modeling GM detectors using the cell flux (F4) and the energy cell flux (*F4) tallies were proposed. The F4 method was selected to model GM detectors in this research and was validated with experimental measurements. The MCNP system model was shown to represent the experimental model based on the proven capability of localizing the gamma source. The MCNP system model was used as a baseline design model and design factors that can improve its performance were studied. These factors were found to be collimator

material and geometry, number and size of collimator channels, the source-to-detector distance and the type of detector used for measurements. A set of high-level design recommendations were derived based on these design factors, which can serve as guidelines for system developers to design and optimize a CS-based radiation source imaging system. The findings from this work contribute to the diversification of counter terrorism tools, encourage future research on NNLS technique application for image reconstruction and promote cheaper radiation source imaging system development. These research findings will also help motivate higher engagement among countries in strengthening global nuclear security initiative.

DEDICATION

To my late Mom, Norina Binti Abdullah @ Saripah anak Atan, who departed from this world on January 20, 2020. And my Dad, Anuar Bin Rahmat. Your love and prayers made this possible.

ACKNOWLEDGEMENTS

I would like to thank my committee chair, Dr. Marianno for being so kind and understanding, providing full support and guidance throughout this research. Thank you as well to my committee members Dr. Chirayath, Dr. McClarren and Dr. Narayanan for their valuable feedback and advice.

Thank you to my friends who were always there to work through research problems or class assignments, helped me destress by playing board games or going on impromptu trips, cooked delicious food whenever I craved for Malaysian food - thank you, Athena, Shu Ying, Syikin, Clement, Sarah, Fieza for bearing with me! To office mates; Matt, Jeremy, Jackson, Rob and the rest for helping out with my research. To those who helped me with my experiments; Ryan Stolt, Zachary Jones, Robert Kollman and Dalton Wise, and Dr. Kurwitz for letting us use his laboratory for the experiments.

Not forgetting the support from Universiti Tenaga Nasional for allowing me to go on a study leave. I'm thankful for the graduate assistantship provided by the Nuclear Engineering Department, as well as the Graduate Teaching Fellowship from the College of Engineering. Thank you, Prof. Kinra for believing in me.

Finally, to these people, the main reason this was all possible, the never-ending support and prayers from my late Mom, my Dad and my loving husband, Ang Wei Eng. Also, my family members! I am beyond lucky to have them in life and may everyone who I have mentioned here and those who had directly or indirectly contributed to this success be rewarded with all the good things in this life and beyond. Thank you, y'all!

CONTRIBUTORS AND FUNDING SOURCES

Contributors

This work was by a dissertation committee consisting of Professor Craig Marianno [advisor] and Professor Sunil Chirayath of the Department of Nuclear Engineering, Professor Krishna Narayanan of the Department of Electrical and Computer Engineering and Professor Ryan McClarren of the Department of Aerospace and Mechanical Engineering, University of Notre Dame.

All other work conducted for the dissertation was completed by the student independently.

Funding Sources

Graduate study was supported by a graduate assistantship funded by the Department of Nuclear Engineering and a fellowship funded by the College of Engineering, both of Texas A&M University. This work was also made possible in part by Universiti Tenaga Nasional through a paid study leave contract.

NOMENCLATURE

ADC	Analog-to-Digital Converter
ANS	American National Standard
ANSI	American National Standards Institute
ANSTO	Australian Nuclear Science and Technology Organization
CZT	CdZnTe
CS	Compressed sensing
DNDO	Domestic Nuclear Detection Office
EUROPOL	European Union Agency for Law Enforcement Cooperation
GPSR	Gradient Projection for Sparse Reconstruction
GSDs	Gamma search detectors
GM	Geiger Muller
IAEA	International Atomic Energy Agency
ICRP	International Commission on Radiological Protection
INTERPOL	International Criminal Police Organization
ITDB	Incident and Trafficking Database
MCNP	Monte Carlo N-Particle
MRDs	Mobile radiation detection systems
NaI	Sodium Iodide
NNLS	Non-negative least square
NTP	Normal temperature and pressure

NSDs	Neutron search detectors
PMT	Photomultiplier tube
PSD	Pulse shape discrimination
PVC	Polyvinyl chloride
RDD	Radiological dispersal device
RIDs	Radionuclide identification devices
RIP	Restricted isometry property
RPMs	Radiation portal monitor monitors
PRDs	Personal radiation detectors
SCA	Single-channel analyzer
SDEF	Source definition
TV	Total Variation
VISED	Visual Editor
WCO	World Custom Organization

TABLE OF CONTENTS

Page

LIST OF FIGURES

Page

LIST OF TABLES

Page

1. INTRODUCTION

1.1. Motivation

The International Atomic Energy Agency (IAEA) reported 3497 incidents between 1993 and 2018 that involved radioactive and nuclear material trafficking in the 2019 IAEA Incident and Trafficking Database (ITDB) [1]. There was an increase of 189 reported incidents by participating Member States in just one year (3686 incidents between 1993 and 2019) [2]. Radioactive and nuclear material could be used by terrorists to construct a radiological dispersal device (RDD) to explosively spread radioactive materials over a large area. In order to detect this type of illicit material, border crossings and shipping ports are equipped with monitoring systems. Currently, there are several established technologies available, but new technologies and methods are needed. This research offers a method to perform secondary monitoring to verify the alarm from primary monitoring system. Secondary monitoring systems are important in helping personnel to make the decision on how to handle the suspected radioactive source, especially when the shape of the radioactive material can be determined.

1.2. Research Objective

The main objective of this research was to develop a design concept for imaging radiation sources using compressed sensing (CS) principles. The resulting system was expected to localize the imaged radioactive source and provide its shape information. This core objective was broken down into more detailed objectives through the formation of six research milestones. The milestones to meet the objectives are listed in sequential order as follows;

i. Conceptualizing a radiation source imaging system,
ii. Designing an initial proof-of-concept system using Monte Carlo N-Particle (MCNP) simulations,
iii. Build the apparatus based on simulation results,
iv. Testing experimental apparatus and match to simulation results,
v. Modify simulation model or experimental design to validate simulation,
vi. Propose a better design or technique for a gamma source imaging system.

The conceptualization of a CS-based radiation source imaging system was initiated with a series of design processes for the system. Section 2 contains a published paper in 2020, which presents the proposed proof-of-concept design for a neutron source imaging system and outlines the procedure in creating an initial design using MCNP simulations. This peer reviewed article covers the first and the second milestones of this research.

The physical model was then built according to the simulation model and several preliminary experiments were performed with a 3.7-MBq ^{252}Cf neutron source. However, there were complications in terms of measurement interference with other neutron sources used for another experiment at the experiment location. It was decided to continue the study by experimenting with a gamma source instead. Section 3 outlines the design processes for a proof-of-concept system to image gamma sources and the experimental planning for model validation.

Experimental apparatus for gamma source imaging setup was tested and the results were presented as a journal paper (to be published) in Section 4. This paper suggested a novel way to model the Geiger Muller (GM) detectors used in the MCNP simulations and

validates the method with experimental measurements. Section 4 covers milestones 3, 4 and 5 with the enhancement of the simulation model's detection system to better represent real-life detection mechanism.

Section 5 presents the benchmarking of the proposed CS-based gamma source imaging system with experimental measurements. The MCNP model validation with experimental measurements is demonstrated in Section 5 (to be published) and allowed for milestones 4 and 5 to be completed. The trends and results from simulations were compared to experimental results in this section. Analyses concluded that the proof-of-concept model was validated as required in milestone 4.

Finally, Section 6 covers the final milestone through a study on design factors that can improve the system's performance. Several test models were built upon the previous one to study the effect of factors related to the design of the system on the reconstructed images. This led to a proposal of high-level design recommendations to guide the design process for a gamma source imaging system that utilizes compressed sensing principles, fulfilling the final milestone of this research.

1.3. Literature review

There are hundreds of imaging system designs that detect gammas, neutron or both as reported by the IAEA [3]. Each utilizes different combination of collimation, detection and image reconstruction methods. In order to determine the combination of collimation, detection and image reconstruction methods for this research, it is important to understand the basis of this work, which are the CS principles.

The CS applications in nuclear security involved the use of CS in the post-signal production stage. Studies have been carried out to show the possibility of sampling signal data below the so-called Nyquist sampling rate in reconstructing spectrometry [4]. However, there are limited studies on applying CS principles to the hardware design so that only a small number of measurements is needed, instead of sampling data from a massive amount of measurement data [5]. The proposed design in this research attempts to show the feasibility of incorporating CS principles in the physical system design so that only a small number of measurements is needed to estimate the image of interest accurately. Efforts in adopting CS for solving nuclear science and engineering problems reported are limited [6].

1.3.1. Compressed sensing

The foundation of this research are the CS principles. The design of the proposed system is based on CS requirements and the knowledge of radiation interaction. Compressed sensing is a method to recover an original signal or data from a small measurement set (data samples), which according to classical linear algebra is not possible because there are infinitely many solutions for an underdetermined system.

Candes, Romberg, and Donoho started discussing CS circa 2005 and 2006 [7]–[11]. These researchers also showed that CS principles allow for signal recovery from a much smaller amount of sampled output signals than the traditional requirement of the Nyquist sampling rate, which is at least twice the highest frequency of the signal [12], [13]. In the case of imaging, three examples of traditional scanning methodologies are the pixel array, raster scan, and basis scan, which require the same number of measurements,

m as the number of pixels, n to recover the original image signal, x. CS principles allow for $m \leq n$ to closely approximate the original image, x with high probability [14]. The achievement of sub-Nyquist image reconstruction presents one of the strengths of CS application in imaging methodology.

Mathematically, measurements using CS can be translated into another set of data that collectively form the recovered original signals, such as an image of the object of interest in an imaging application. The original data or signal, x is related to the measured data, y according to $Ax = y$ with A being a matrix that models the measurement process by mapping x to the measured signals, y. With sparsity in x and the randomness of A, original data or signal recovery is possible using several algorithms [15], [16]. The vector x in this research is the image of the radiation source.

Sparsity is a measure of the zero elements in a quantity. Hence, x is said to be sparse if most of its components are zero. In general, x is said to be k-sparse if there are at most k nonzero components. Most of the time, x is only sparse after being converted into a different basis, for example the discrete cosine or wavelet basis. By storing the largest discrete cosine or wavelet coefficients and setting the rest to zero, media such as images or songs can be stored as a much smaller data size. This is possible because these small number of coefficients can be recovered using some minimization methods [15].

Two examples of random matrices are the Gaussian matrix and the Bernoulli matrix. The Gaussian matrix is one with entries that are independent random variables that follow a normal distribution. The Bernoulli matrix is a matrix with entries that are independent random variables taking values of +1 and -1 with equal probability. Setting

matrix A to be a random matrix ensures the incoherence of the matrix is preserved and this is important because it would result in better likelihood for successful signal recovery [17]. Incoherence is the largest magnitude of the row or column entries of A, which is a rough measure of how concentrated the rows or columns of A are. With Gaussian or Bernoulli matrix as an example, the value of incoherence parameter would then be between 1 and $\sqrt{n}$, where n is the dimension of A matrix [17].

One important fundamental mathematical concept in CS is the l_p-norms, $||z||_p$ which are commonly used to measure the signal strength or the error size [13]. A popular program developed when CS was introduced is called *l_1-MAGIC*. This program has multiple methods to determine x depending on the type of problems to be solved using an l_1-minimization method [7]. All of the methods in *l_1-MAGIC* program estimate x by minimizing the l_1-norm of z, $||z||_1$ but each method has different constraints. The vector z obtained from these methods has been shown to be very close to or the same as the original data, x [7]. One example of the methods is called *basis pursuit*, in which $||z||_1$ is minimized subject to $Az = y$ using a standard convex programming algorithm [14].

Another method of interest to estimate x is the non-negative least square (NNLS) method by minimizing the l_2-norm of $y - Az$, written as $||y - Az||_2$, subject to $Az = y$ for $z > 0$. This method has been shown mathematically to work in estimating the original data, x [18] by solving for z according to the constraints defined. The non-negativity requirement is of interest in this research because the image of the radiation source would consist of only positive values to indicate the presence of gamma rays, based on the design

of matrix A. Consequently, x can be recovered using the *MATLAB* built-in function, *lsqnonneg* which executes a NNLS algorithm [18].

The recovery of x by l_1-minimization means that x is a unique solution that satisfies $Ax = b$. If x is nonnegative and sparse, the use of NNLS will typically solve for x, provided that the active Lawson-Hanson algorithm is used, which is employed by the *lsqnonneg* function in *MATLAB* [18]. Even though NNLS is not necessarily a CS technique, the proposed design for the system in this research was based on CS requirements. The possibility to use a built-in *MATLAB* function to reconstruct x is convenient. Therefore, the simplicity of this idea motivates the use of NNLS in the image reconstruction for this research.

$$m \geq Ck\,log(n) \qquad (1-1)$$

Other than randomness in A matrix, it is also required that A fulfills the restricted isometry property (RIP) in order to have robustness to noise in measurements [13]. If A satisfies this property, the distance between any k-sparse vectors is preserved. The amount of measurements necessary to ensure RIP is achieved and is determined by Eq. 1-1, where C is a small constant [13], [17]. Therefore, as an example, for a 64 × 64 image (n = 4096) with a poor sparsity of k = 600, the minimum number of measurements required to recover the image with high probability, assuming a conservative value of C = 1, would be 2167 measurements. This means that with the number of measurements that is 52.7% of the total pixels, the recovered image closely estimates the original image. With a much lower sparsity in x, less measurements would be needed. With these results, the choice of m in

the MCNP simulations for this research was taken to be more than 55% of the total pixels, n in order to ensure the success of image reconstruction.

1.3.2. Previous work

Previous related work is analyzed and summarized to form the novelty of this research. The following subsections describe selected publications and how this PhD research builds upon and improves inadequacies of these past related work.

1.3.2.1. Callas et al. 1995

A gamma ray imaging system using a germanium sensor and a coded aperture made of lead bricks was demonstrated in 1995 for a ^{22}Na gamma ray source [19]. The detected 511-keV flux was plotted over a 5×5 pixel-sized image using a nonnegative least squares algorithm. Measurements were taken with 10 rotations of the coded aperture that was positioned such that its elements were parallel to the detector segments. The vector of source pixel estimates was determined using a linear least squares approach and a Monte Carlo simulation to compute the forward response matrix.

The system showed the possibility to localize the source by accounting for the interference due to Compton scattering in the forward response matrix and changing detector background readings as the coded aperture rotation changed. The research however did not produce an image of the gamma source, but instead plotted the photopeak of interest in 9 pixels, deconvolved from 7×7 source field using spectral techniques. Unlike the work of Callas et al., this PhD research improved the use of nonnegative least squares algorithm by using data from a system that was designed according to CS

principles and then plotting the image of the source to facilitate source localization and its shape identification.

1.3.2.2. Gestner, 2013

A study was carried out at Sandia National Laboratories on the development of novel hardware for photomultiplier tube (PMT) output signal acquisition guided by CS [4]. The PMT was coupled to a scintillator material to convert the weak fluorescence to an electrical output signal. The motivation of this research was to reduce the acquisition system cost, power consumption and average data rate so that such a system could be remotely deployed and possibly incorporated into wireless sensor networks. This was claimed to be possible because sparse representation of the PMT output signals in the frequency domain was found to be sufficient [20].

Gestner attempted to incorporate CS framework to the existing empirical model of neutron and gamma ray pulses [21] in order to make the sampling rates much lower than the generally accepted minimum rate of 200 MHz. It was demonstrated successfully that the PMT output signals could be efficiently represented in the Discrete Haar Wavelet domain. Only eight out of 64 Discrete Haar Wavelet coefficients were required to reconstruct the pulse shape discrimination (PSD) plot for a set of 64 Analog-to-Digital Converter (ADC) samples. The reconstructed PSD plots contained sufficient pulse energy, pulse location and PSD information.

The study then mapped the CS framework to the proposed acquisition system and performed the experiment based on the representation of the PMT output signal in the Discrete Haar Wavelet domain. It was found that the compressive samples did not contain

enough PSD information even when 16 compressive samples were used for signal reconstruction. However, pulse energy and pulse location information were shown to be sufficient even when only eight compressive samples were used. The study by Gestner is an example that shows an attempt to apply CS principles in the output signal processing of a measurement system. This PhD research attempted to incorporate CS principles in the hardware and measurement process designs, instead of just the acquisition output signal processing, and it was proven to be a promising solution for future applications in nuclear security.

1.3.2.3. Ayzman, 2015

This graduate research simulated a neutron imaging system that consisted of a 32×32 collimator (n = 1024) made of borated polyethylene for a passive imaging system to localize a neutron source and a 64×64 collimator (n = 4096) made of a material called densalloy, mainly made of tungsten, for an active imaging system to image organic materials [22]. The end of the collimator, closest to the source, had simulated flaps made of neutron absorbing materials. These would be opened or closed to simulate a random mask for the measurement process.

The simulation was performed using MCNP with an FMESH tally (fluxes in meshed cells) placed at the other end of the collimator that represented a radiation detector. The fluxes in the meshed cells extracted from MCNP outputs were then manipulated to simulate measurements taken with random masks imposed by the collimator. The resulting 2D images were then reconstructed using a CS tool called the l_1-*MAGIC* Total Variation (TV) minimization solver [7]. Both passive and active designs were shown to work

through simulations at sampling rates between 30% and 60%, in which 100% sampling rate means that the number of measurements is the same as the total number of pixels.

The simulated designs proposed by Ayzman could not be physically constructed because the simulated model was oversimplified as the detectors were simulated with a void of the same cross-sectional size of the collimator array; the noise was assumed to be zero when the collimator mask elements were supposed to be absorbing neutrons (in reality the noise would not be zero); the active imaging system requires the use of a plane source emitting 14-MeV neutrons in the collimation direction, and that the physical measurement process was not simulated. This PhD research replaces these oversimplifications by simulating the detectors with available materials and equipment for an experiment to prove this method; designing an improved collimation system that would optimize the measurements' signal-to-noise ratio; designing a more practical system that can allow for experiments to be done to validate simulation data; and simulating as well as performing the designed measurement.

1.3.2.4. Boardman et al., 2020

At the end of 2020 when the experimental measurements for this PhD research was concluded at, a spectroscopic gamma-ray imaging technology using compressed sensing theory was released by the Australian Nuclear Science and Technology Organization (ANSTO) [23]. The research team had published the initial findings that drove the development of the technology [24]. The publication demonstrated experimental results from using 128 randomly patterned steel masks and a $1\times1\times0.5$ cm^3 CdZnTe (CZT)

detector to measure photon counts. Image reconstruction was performed using the Gradient Projection for Sparse Reconstruction (GPSR).

The imaging was done for two point sources with a 16-by-16 pixel field of view, and results showed that the system used only 10% of the total measurements required by an equivalent raster scanning system. An extended source imaging was also studied by having ^{99}Mo/^{99m}Tc and ^{67}Ga liquid radionuclides dispensed onto a piece of absorbent paper in the shape of 'A' and 'X', respectively. The images produced with 33% and 50% of the total measurements normally required for a 256-pixel image were compared. It was demonstrated that both measurements gave similar results, but the images for 50% of total measurement needed have less signs of degradation (better image quality).

Despite the similarities in their work and this PhD research, a major difference is in the use of the image reconstruction method. This research uses the non-negative least squares (NNLS) algorithm to reconstruct images instead of the GPSR algorithm. NNLS has been demonstrated in this PhD study to be an alternative method for image recovery. Additionally, the use of GM detectors in the imaging system was also studied and its results were compared with those of spectroscopic detectors. The success of employing relatively cheaper GM detectors in this study is promising as some nuclear security programs, especially in developing nations, have limited budget available to support their nuclear security initiative. The potential of using affordable GM detectors for imaging promotes technology transfer, which is important in establishing a stronger global nuclear security system [25]. The simplicity in the reconstruction method employed and the proof

of cheaper alternatives for radioactive source imaging system resulted from this PhD work can motivate new developments and improvements of such system in the future.

1.4. References

[1] "IAEA Incident and Trafficking Database (ITDB): 2019 Fact Sheet." International Atomic Energy Agency (IAEA). [Online]. Available: https://www.iaea.org/sites/default/files/19/04/itdb-factsheet-2019.pdf

[2] "IAEA Incident and Trafficking Database (ITDB): 2020 Fact Sheet." International Atomic Energy Agency (IAEA). [Online]. Available: https://www.iaea.org/sites/default/files/20/02/itdb-factsheet-2020.pdf

[3] International Atomic Engergy Agency, Ed., *Safeguards techniques and equipment*, 2011 edition. Vienna: International Atomic Energy Agency, 2011.

[4] B. J. Gestner, "Compressive sensing for nuclear security," Sandia National Lab. (SNL-CA), Livermore, CA (United States), SAND2013-10506, Dec. 2013. doi: 10.2172/1121944.

[5] R. F. Marcia and R. M. Willett, "Compressive coded aperture superresolution image reconstruction," in *2008 IEEE International Conference on Acoustics, Speech and Signal Processing*, Mar. 2008, pp. 833–836. doi: 10.1109/ICASSP.2008.4517739.

[6] E. W. Larsen, "Opportunities and challenges in applying the compressive sensing framework to nuclear science and engineering," *Transport Theory and Statistical Physics*, vol. 40, no. 4, pp. 225–242, Oct. 2011, doi: 10.1080/00411450.2011.610205.

[7] E. Candes and J. Romberg, "l1-magic : Recovery of Sparse Signals via Convex Programming." [Online]. Available: https://statweb.stanford.edu/~candes/software/l1magic/downloads/l1magic.pdf

[8] E. J. Candès, "Compressive sampling," in *Proceedings of the International Congress of Mathematicians*, Madrid, Spain, 2006, pp. 1433–1452.

[9] D. L. Donoho, "Compressed Sensing," in *IEEE Transactions on information Theory*, Apr. 2006, vol. 52, pp. 1289–1306. doi: 10.1109/TIT.2006.871582.

[10] E. J. Candes, J. Romberg, and T. Tao, "Robust uncertainty principles: exact signal reconstruction from highly incomplete frequency information," *IEEE Transactions on Information Theory*, vol. 52, no. 2, pp. 489–509, Feb. 2006, doi: 10.1109/TIT.2005.862083.

[11] E. Candes, J. Romberg, and T. Tao, "Stable Signal recovery from Incomplete and Inaccurate Measurements," *Wiley Periodicals, Inc.*, vol. LIX, pp. 1207–1223, 2006.

[12] M. F. Duarte and Y. C. Eldar, "Structured Compressed Sensing: From Theory to Applications," *IEEE Transactions on Signal Processing*, vol. 59, no. 9, pp. 4053–4085, Sep. 2011, doi: 10.1109/TSP.2011.2161982.

[13] M. A. Davenport, M. F. Duarte, Y. C. Eldar, and G. Kutyniok, "Introduction to compressed sensing," in *Compressed Sensing: Theory and Applications*, G. Kutyniok and Y. C. Eldar, Eds. Cambridge: Cambridge University Press, 2012, p. 5. doi: 10.1017/CBO9780511794308.002.

[14] M. F. Duarte *et al.*, "Single-pixel imaging via compressive sampling," *IEEE Signal Processing Magazine*, vol. 25, no. 2, pp. 83–91, Mar. 2008, doi: 10.1109/MSP.2007.914730.

[15] S. Foucart and H. Rauhut, "Basic Algorithms," in *A Mathematical Introduction to Compressive Sensing*, S. Foucart and H. Rauhut, Eds. New York, NY: Springer, 2013, pp. 61–75. doi: 10.1007/978-0-8176-4948-7_3.

[16] M. Blasche and C. Forman, "Compressed Sensing – the Flowchart."

[17] E. Candès and J. Romberg, "Sparsity and incoherence in compressive sampling," *Inverse Problems*, vol. 23, no. 3, pp. 969–985, Apr. 2007, doi: 10.1088/0266-5611/23/3/008.

[18] S. Foucart and D. Koslicki, "Sparse Recovery by Means of Nonnegative Least Squares," *IEEE Signal Processing Letters*, vol. 21, no. 4, pp. 498–502, Apr. 2014, doi: 10.1109/LSP.2014.2307064.

[19] J. L. Callas, W. A. Mahoney, R. T. Skelton, L. S. Varnell, and W. A. Wheaten, "Gamma-ray imaging laboratory measurements using externally segmented germanium detectors," *IEEE Transactions on Nuclear Science*, vol. 42, no. 3, pp. 121–129, Jun. 1995, doi: 10.1109/23.387351.

[20] G. Liu, M. J. Joyce, X. Ma, and M. D. Aspinall, "A Digital Method for the Discrimination of Neutrons and γ Rays With Organic Scintillation Detectors Using Frequency Gradient Analysis," *IEEE Transactions on Nuclear Science*, vol. 57, no. 3, pp. 1682–1691, Jun. 2010, doi: 10.1109/TNS.2010.2044246.

[21] S. Marrone *et al.*, "Pulse shape analysis of liquid scintillators for neutron studies," *Nuclear Instruments and Methods in Physics Research Section A: Accelerators, Spectrometers, Detectors and Associated Equipment*, vol. 490, no. 1, pp. 299–307, Sep. 2002, doi: 10.1016/S0168-9002(02)01063-X.

[22] Y. J. Ayzman, "Single Pixel Neutron Camera Using Compressive Sensing," Thesis, 2016. Accessed: Sep. 20, 2021. [Online]. Available: https://oaktrust.library.tamu.edu/handle/1969.1/187398

[23] "CORIS360 Online Brochure." Australian Nuclear Science and Technology Organisation (ANSTO), Aug. 2021. Accessed: Sep. 13, 2021. [Online]. Available: https://www.ansto.gov.au/sites/default/files/2021-08/CORIS360-Online-Brochure-Aug2021.pdf

[24] D. A. Boardman, A. Sarbutt, A. Flynna, and M. C. Guenette, "Single pixel compressive gamma-ray imaging with randomly encoded masks," *J. Inst.*, vol. 15, no. 04, pp. P04014–P04014, Apr. 2020, doi: 10.1088/1748-0221/15/04/P04014.

[25] C. Englefield, "Radioactive source security: Why do we not yet have a global protection system?," *Nuclear Engineering and Technology*, vol. 46, no. 4, pp. 461–466, Aug. 2014, doi: 10.5516/NET.08.2014.713.

2. EMPLOYING MCNP TO OPTIMIZE EXPERIMENTAL DESIGN FOR COMPRESSED SENSING NEUTRON SOURCE IMAGING*

2.1. Introduction

Traditionally, an image with M pixels requires M measurements to reproduce it and this method is known as the raster scan method [1]. Compressed (or compressive) sensing theory however allows for smaller number of measurements, K, to recover information that was thought to be unrecoverable if $K < M$ [2]. This information acquisition method has been utilized in signal processing and data storage applications, but very few studies have been performed in nuclear imaging applications [3–5]. A neutron imaging technique was proposed to include the principles of compressed sensing in the collimator design [6]. It is emphasized that the objective of this research is to image a neutron source to determine its shape and size as this is useful for nuclear security applications.

This novel technique would be helpful in the efforts to monitor contraband nuclear materials transportation at shipping ports or land borders. Neutron source imaging may be better than just neutron detection as it would help in determining the level of response that is needed if the shape of the suspected neutron source could be visualized. One advantage of this design is that it allows for the use of only one or two neutron detectors to image a source with fast neutrons. The materials used for this proposed system design are also

*Reprinted with permission from "Employing MCNP to optimize experimental design for compressed sensing neutron source imaging," by N. Anuar, C. Marianno, and R. G. McClarren, Feb. 2020. *Nuclear Instruments and Methods in Physics Research Section A: Accelerators, Spectrometers, Detectors and Associated Equipment*, Vol. 954, p. 161446.

inexpensive and ubiquitous, making it inexpensive to acquire and implement. A system utilizing this technique could also be employed at nuclear installations to compare neutron image signatures for nuclear safeguards purpose.

The fundamental principle that allows for this technique to work is the fact that mathematically, signals obtained by measurements using compressed sensing can be translated into another set of signals that collectively form the image signals, x. Compressive sensing works because x is required to be s-sparse, which means that x can be represented using only s non-zero coefficients. As x is plotted as an image, lighter shades in x would represent the possible positions with stronger neutron intensity. Therefore, if a neutron source is present when the imaging takes place, x would be an s-sparse set of signals as it is expected that the neutron source is the dominant neutron emitter that would stand out from the surrounding.

The translation process utilizes incoherence of a sensing matrix, A, which maps x to the measured signals, b, the neutron counts. In linear algebra, coherence of a matrix is defined as the largest absolute normalized inner product between its different columns, and this characterizes the dependence between the matrix columns. A small value of coherence (higher incoherence) would result in a better likelihood for successful signal recovery. To ensure incoherence, the sensing matrix is required to have randomness as a property. It is shown later in the methodology section that A is assigned to be a random combination of zeros and ones. Solving for x would eventually produce a $2D$ resemblance that identifies the shape and location of the imaged neutron source.

The image signals, x, are recovered using non-negative least squares (NNLS), in which a requirement for the sparse x entries to be non-negative is imposed [7,8]. Nonnegative entries are required because it is assumed that the image signals would consist of only positive values as they would indicate the presence of a neutron source. Other materials surrounding the source are not radioactive, and therefore will not generate positive values. Using the relation $Ax=b$, x matrix recovery is achieved by using a built-in *MATLAB* function called *lsqnonneg* and is explained further in the methodology section. Monte Carlo N-Particle Transport Code (MCNP) [9] simulations were performed to determine the collimator array size (total pixels), dimensions and material for the experiment. Throughout this paper, the chronology of simulations that led to the final system design is elaborated and results are subsequently discussed.

2.2. Methodology

2.2.1. MCNP simulations

The preliminary simulations were based on a cylindrical water tank to determine the required water height to stop all thermal neutrons through scattering and absorption in water. A ^{252}Cf isotropic point source was placed 50 cm above the water and a measurement surface for the $F1$ tally was placed directly underneath the tank. The $F1$ tally defined in MCNP measures particle current (neutron in this case) at an assigned surface. This means that neutron counts will be tallied whenever a neutron, regardless of its energy, crosses the surface of interest. Only direct streaming of neutrons from the source will be used for image reconstruction. Simulations with varying $F1$ tally surface size were run to determine collimator dimensions that ensured minimal in-scatter from exterior neutrons.

The collimator was introduced vertically into the model at the tank's center as a 2×2 array. Simulations were run with three different types of collimator materials: stainless steel, polyvinyl chloride (PVC) and aluminum. Once the appropriate material was identified, an array size of 23×23 was arbitrarily chosen. A ring source was positioned at 50 cm above the water surface and was defined as a 1 μCi ^{252}Cf spontaneous fission neutron source emitting 4.31×10^3 ns^{-1}. A ring source was chosen so that the image quality could be evaluated by the easiness of source shape and position identification.

After the image produced using 23×23 array size was evaluated, the array size was reduced by half to see if there was any difference in the image quality. An acceptable image quality difference would mean that smaller array size may be employed as it would result in a more practical experiment. Another model with an 11×11 array size, but with a rectangular tank was simulated due to the availability of a rectangular tank for the experiment. The rectangular tank model used a 100 μCi of the same neutron source.

Table 2-1. The dimensions of MCNP simulation models. Reprinted with permission from "Employing MCNP to optimize experimental design for compressed sensing neutron source imaging.".

Item	Dimensions (cm)
Cylindrical tank	$31.48(R) \times 101(H)$
Parallelepiped tank	$101.6(W) \times 121.92(L) \times 137.16(H)$
23×23 pipe	$0.316(ID) \times 0.514(OD) \times 100(H)$
11×11 pipe	$0.635(ID) \times 0.912(OD) \times 100(H)$

A configuration is defined as a combination of air-filled (empty) pipes and water-filled pipes. Empty pipes are represented as 1's in the A matrix while water-filled pipes

are represented as 0's. This allows for neutron interactions to be defined as follows; the inner product of the A matrix with the image matrix, x, would then represent neutron absorption for multiplication with 0's and neutron streaming towards the $F1$ tally surface at the end of the tank (where the detector will be in the experiment) for multiplication with 1's. The average open channel fraction of the collimator is 0.5. Three hundred random array configurations were created by a Python code for the 23×23 array and 100 configurations for the 11×11 array. This resulted in the creation of 300 and 100 MCNP input files for the 23×23 and 11×11 array, respectively. Each file was run, producing a corresponding output file that contains the $F1$ tally results. These results form a abmatrix that corresponds to the respective array size.

Table 2-1 shows the dimensions used in the MCNP models. The proposed neutron source imaging system is illustrated in Fig. 2-1. This diagram shows the cross-sectional area of the proposed setup on the x–z plane and the x–y plane at z= 50, which is about halfway through the height of the tank. The collimator array is placed in the middle of the tank with rubber stoppers fixed at the bottom ends. Figure 2-1 shows the configuration with all pipes filled with water (matrix A entries are all zeros). For proposed experiments, two ^{3}He neutron detectors are placed beneath the tank and a neutron source is placed on or above the collimator. Depending on the row entries of matrix A, different configurations of collimator can be obtained by removing water (if the entry is 1) or adding water (if the entry is 0) into corresponding pipes.

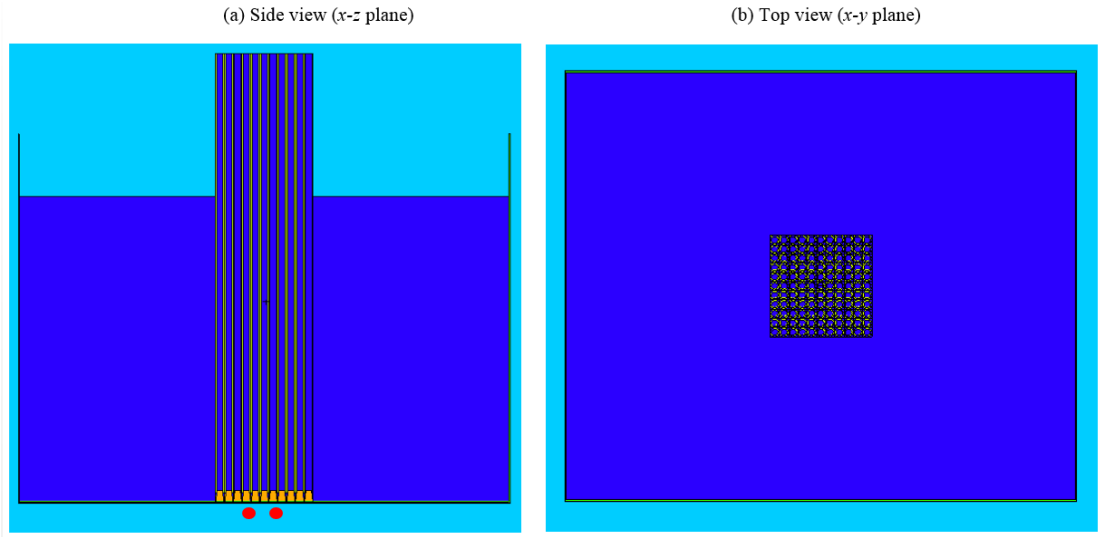

Figure 2-1. Illustration of the proposed neutron source imaging system displayed using the MCNP Visual Editor software showing the cross-sectional views on the x–z plane at $y = 0$, and the x–y plane at $z = 50$. Reprinted with permission from "Employing MCNP to optimize experimental design for compressed sensing neutron source imaging".

2.2.2. Image reconstruction

A Python code was created to extract the array configurations from the MCNP input files and to rewrite in an Excel spread sheet where each array configuration is stored as the row entry of the spreadsheet. The extracted data forms matrix$A$, which is therefore a 300×529 matrix for the 23×23 array and 100×121 for the 11×11 array. The $F1$ tally results were also extracted from the corresponding output files and rewritten as the row entry in another spreadsheet. These entries in a new Excel sheet make matrix b. Here, b is a 300×1 matrix for the 23×23array and 100×1 for the 11×11 array.

$$\min\left|\left|x\right|\right|_1 \text{ subject to } A\,x = b \qquad (2-1)$$

Image reconstruction in compressed sensing is usually solved using l_1-minimization. There are a few variations of l_1-minimization technique, depending on the

type of problem to be solved. The earliest code was developed using *MATLAB* program and is known as the l_1-MAGIC program [2]. An example of one way to solve for x=b/A by l_1-minimization is shown by Eq. 2-1, which is known as basis pursuit. If a nonnegative vector, x, is recovered by l_1-minimization, then itis the unique nonnegative vector that satisfies Ax=b. Therefore, x can also be recovered by NNLS by solving for x=b/A and minimizing the l_2 of the difference between b and the inner product of A and x as shown in Eq. 2-2. If the image, x, is nonnegative and sparse, the use of NNLS will typically solve for x if the NNLS uses the active Lawson–Hanson algorithm.

$$\min\left|\left|\mathrm{b}-\mathrm{Ax}\right|\right|_2 \text{ subject to } \mathrm{z} \geq 0 \qquad (2-2)$$

Solving for Eq. 2-2 using an active set is possible by solving an un-constrained least-square problem that includes only inactive variables, if the active variables are known [10]. This is done by attempting to find the nonnegative solution with some variables being assigned to zero. These variables are called an active set because of their non-negativity constraints being activated. The active set is modified by a single variable in each iteration and finally the unconstrained least-square problem is solved without the active set [11]. The *lsqnonneg* function in *MATLAB* executes the Lawson–Hanson algorithm that employs this active-set technique [8].

A comparison between the l_1-minimization solution and the NNLS solution is presented and discussed in the subsequent section for the 23×23 array with the ring source positioned near the top-right corner of the collimator array with K= 300.The recovered signal matrix, x, is shown as a gray-scaled image using the *imagesc* command in *MATLAB*.

For the 11×11 rectangular data, images were constructed with various numbers of measurements, K, starting from 100 and reduced to 30 with an interval of 10 measurements. The purpose of this was to observe the effect of K value on image quality.

2.3. Results and discussions

The initial simulations resulted in the requirement for a 100 cm height of water to stop all thermal neutrons (less than 0.025 eV) at the bottom of the cylindrical water tank. This was reflected by the zero value of MCNP tally output for thermal neutrons. The array was required to be smaller than 25.3 cm by 25.3 cm to avoid in-scattering from the sides of the tank into the $F1$ tally surface.

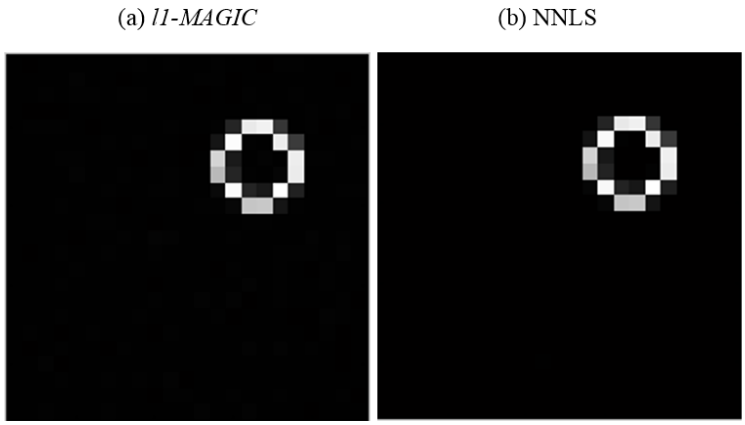

Figure 2-2. Comparison between the solution produced by *l1-MAGIC* and *lsqnonneg* for a cylindrical tank with 23×23 array for K= 300. Reprinted with permission from "Employing MCNP to optimize experimental design for compressed sensing neutron source imaging".

Placing a different material in the tank might cause some neutrons to reach the $F1$ tally surface because of its lower neutron absorption cross section compared to that of water. Since most of the thermal neutrons are supposed to be absorbed by the determined

water height, a material that would result in minimal number of neutrons to reach the $F1$ tally surface would be preferable. Stainless steel was found to be the best collimator material as it caused minimal neutrons traveling through the length of the collimator compared to PVC and aluminum. However, there was only a 0.17 ± 0.09 ns^{-1} average-count-rate increase when PVC was used as the collimator material. Since PVC pipes are less expensive than the stainless-steel pipes, PVC was selected as the collimator material for the proof-of-concept experiment.

With these requirements, the neutron source image was reconstructed successfully by the 23×23 array size using all measurements (K= 300). The reduced array size to 11×11 resulted in a source image with lower resolution as expected using all measurements (K= 100), but with an image quality that still allows for source localization and shape identification. The reconstructed image, x using l_1-*MAGIC* is compared with using *lsqnonneg* function in *MATLAB* in Fig. 2-2. It can be seen here that the NNLS technique gives the same solution as the l_1-minimization technique. Due to this similarity, all images in this work were then processed with the *lsqnonneg* function in *MATLAB*, with matrices A and b as its inputs. NNLS was chosen to solve for$x$because this technique is faster and readily available in *MATLAB*, while also producing a verisimilar solution as l_1-minimization solvers do.

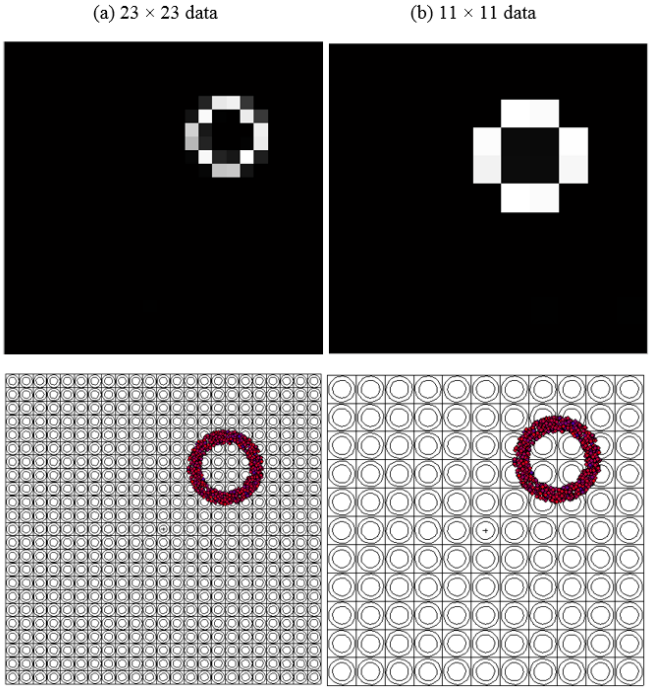

Figure 2-3. The image produced using a cylindrical tank for a ring source at top-right corner by (a) 23×23 simulation data with$K$= 300, and (b) 11×11 simulation data with K= 100. The dotted plot depicting a ring in the bottom figures is the source plot displayed using the MCNP Visual Editor software with the top view of the array. Reprinted with permission from "Employing MCNP to optimize experimental design for compressed sensing neutron source imaging".

A comparison between the images produced by the 23×23 array and the 11×11 array is shown in Fig. 2-3. It was determined that an 11×11 would be a suitable and practical array size for a physical experiment. Due to availability of a rectangular 250-gallon water tank, another MCNP model with these new characteristics was built. The images produced as a function of K are depicted in Fig. 2-4 which shows that significant degradation of image quality was observed below K= 60. The source shape and location were changed to a larger ring placed in the middle of the collimator to facilitate better comparison of image quality as a function of K.

For measurements with low count rates, large relative error in b is expected. This will in turn result in large uncertainties in x. Ideally, the determination of the minimum K would be more precise by performing many reconstructions from multiple data sets (each data set contains measurements for 100 configurations). However, the simulations done so far are meant to serve as a benchmark for the actual experiment. For example, it should be possible to start seeing the source shape or location when at least K= 50 measurements have been obtained. In the future, multiple data set reconstructions will be implemented for final design optimization.

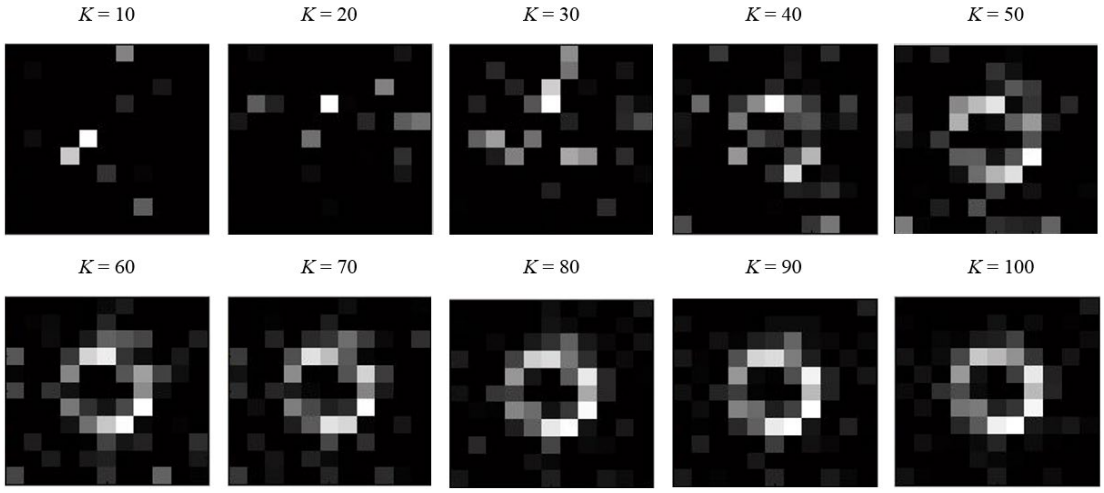

Figure 2-4. Images produced at different K values for a simulation of a ring source at the center of a rectangular tank with an 11×11 array. Reprinted with permission from "Employing MCNP to optimize experimental design for compressed sensing neutron source imaging".

MCNP simulations for this rectangular water tank show that for a ring source strength of 100 μCi with ^{252}Cf fission spectrum, the average total number of neutrons crossing the bottom of the tank for all of the configurations is 2.58 ± 1.6 ns^{-1}. Assuming a neutron background of 0.5 ns^{-1} and a detector efficiency of 0.01, a 10-minute

measurement for one configuration would result in an expected average count of 15.5 ± 3.9 and an expected background count 3.0 ± 1.7. These measurements are not statistically the same within 2σ of each other, hence a 10-minute count (or longer) would be sufficient for analysis through the image reconstruction process.

2.4. Conclusion

MCNP simulation results indicate that an 11×11 array of PVC pipes would be sufficient and feasible to perform a physical experiment for neutron source image reconstruction. Simulations showed that image quality allowing for neutron source shape and location determination is obtained with as low as 50% of the total pixels compared to the conventional raster scan method. This proves to be useful in realizing system that is less expensive and more efficient in localizing and identifying the shape of a neutron source. This system is considered as inexpensive as it can only be built using water, PVC pipes, a water tank, and a water pumping system.

2.5. Acknowledgements

This research did not receive any specific grant from funding agencies in the public, commercial, or not-for-profit sectors.

2.6. References

[1] W.S. Yeo, Raster scanning, Online, 2006. URL https://ccrma.stanford.edu/~woony/research/raster/ (Accessed on 31.07.18).

[2] E. Candes, J. Romberg, l1-MAGIC: Recovery of Sparse Signals via Convex Programming, l1-MAGIC User Guide (2005).

[3] D. Vargas, R.C. Kurwitz, I. Carron, K.R. DePriest., Development of a neutronspectroscopic system utilizing compressed sensing measurements, EPJ Web Conf.106 (2016) http://dx.doi.org/10.1051/epjconf/201610607002.

[4] W. Jin, Z. Liu, G. Li., Block-based compressed sensing for neutron radiation imageusing WDFB, Adv. OptoElectron. (2015) http://dx.doi.org/10.1155/2015/496863.

[5] B. Gestner, Compressive sensing for nuclear security, Tech. rep., Sandia NationalLaboratory (2013).

[6] Y.J. Ayzman, Single Pixel Neutron Camera Using Compressive Sensing, (Master'sthesis), Texas A&M University, 2015.

[7] P.D. O'Grady, S.T. Rickard, Compressive sampling of non-negative signals, in: IEEEWorkshop on Machine Learning for Signal Processing, 2008, pp. 133–138.

[8] S. Foucart, D. Koslicki, Sparse recovery by means of nonnegative least squares, IEEESignal Process. Lett. 21 (4) (2014).

[9] T. Goorley, M. James, T. Booth, F. Brown, J. Bull, L. Cox, et al., Initial MCNP6release overview, Nucl. Technol. 180 (3) (2012) 298–315.

[10] J. Chen, C. Richard, J.C.M. Bermudez, P. Honeine, Nonnegative least mean squarealgorithm, IEEE Trans. Signal Process. 59 (2011).

[11] TNT-NN: A fast active set method for solving large non-negative least squaresproblems. Procedia Comput. Sci., 2017, 108, 755–764, https://doi.org/10.1016/j.procs.2017.05.194.5.

3. MODELING A PROOF-OF-CONCEPT SYSTEM FOR IMAGING GAMMA SOURCES

3.1. Introduction

Preliminary measurements for the imaging of a ^{252}Cf source with the physical proof-of-concept system were complicated by interference from another experiment that was ongoing at the same experiment location. It was decided that the validation of the system model was continued with the imaging of a gamma source instead. The availability of a 14.8 MBq ^{137}Cs and Geiger Muller (GM) detectors for an experiment to be set up called for a design update on the previous proof-of-concept system. The procedure of modeling the system for imaging gamma sources is outlined in detail in this section. Fortunately, it was found that there were not any changes needed for the collimation system.

3.2. Method

3.2.1. MCNP modeling

This section consists of the steps taken in designing for a proof-of-concept system for imaging gamma sources. The design is started by defining the system requirements. The gamma source imaging system is required to produce data that will allow for a 2D image of a radiation source to be constructed. The image produced must be able to show the shape and position of the radiation source. In addition, the system must be easy to assemble and have minimal cost to assemble and operate. From here onwards, the phrase "successful image reconstruction" or other similar phrases will be used to indicate the

performance of the system design. Image reconstruction is said to be successful if the shape of the radiation source and its location can be determined correctly from the reconstructed image. For example, measurement data for a small point radiation source placed in the middle of the collimator is expected to produce an image that shows a dot in the middle of the image.

3.1.1.1. The design processes

The design processes followed a logical sequence of systems engineering process which consists of these activities: identifying system requirements (based on the product objectives), determining functional requirements, defining functional architecture, allocating function(s) to the defined subsystems, and performing simulations of the proposed subsystems (synthesis) [1]. Every simulation result will be verified against the higher-level requirements and this whole process will eventually result in the specifications of the system architecture.

There were multiple factors that needed to be determined in deciding the required functional architecture, such as the amount of attenuating material needed; how to turn the *A* matrix into a physical product (collimator); and the radiation detection method. These three factors lead to the introduction of three subsystems that would perform the determined functional requirements; attenuation, collimator and detection subsystems. The attenuation component must be able to attenuate efficiently and easily be removed or placed. The collimator must be a good photon attenuator, does not break easily, as well as lightweight. The detection system must be simple and easy to set up. All of these three

subsystems also are required to be made of materials that are easily available and not expensive. Next is the process of defining the physical architecture for each subsystem.

3.1.1.2. The attenuation subsystem

There are several options for the material that will be used for the photon attenuation subsystem. Some of the well-known materials used in gamma shielding are lead, concrete, glass, water, and polyethylene. Based on the defined system requirements and constraints, the best candidate for attenuation material was found to be water. With this selection, MCNP simulations were performed for a cylindrical-shaped water of radius 30.48 cm, placed 10 cm above a concrete floor with surface current and cell flux tallies (F1 and F4 tally in MCNP) in a cylindrical measurement cell placed at the bottom of it. The energy bins for both tallies were set to 0.6619 and 0.6621 MeV to track the 662-keV photons.

3.1.1.3. The collimator subsystem

MCNP simulations were also performed to determine the maximum collimator dimensions (cross-sectional area) by varying the current and flux tally size. The tally was defined with a cylindrical measurement cell made of air and the radius of the cell, r, was varied in an increment of 5 cm. Ideally, the bigger the collimator dimensions are (the bigger the tally size is), the more information can be gathered for the radiation source imaging. MCNP simulations were performed to see if there was any undesired indirect (scattered) photon detection in the measurement cell at the bottom. If the current across the top surface of the measurement cell was smaller than the current calculated from cell

flux value (F4 tally), it can be said that there was a contribution from undesired scattered photon in the detection.

For the collimator subsystem, there are two aspects that needed to be addressed; its material and pixel configuration. The materials considered to carry out the allocated functions were lead, stainless steel, aluminum and polyvinyl chloride (PVC). Based on the functional requirements, lead was removed from the consideration due to its high density that would affect workability with the material. Next is the pixel configuration, with two methods of collimation in consideration; coded aperture mask and an array of pipes allowing for pixels to be represented. Based on the functional requirements, a pipe array was chosen because the coded aperture mask would have to be manufactured, while pipes are readily available in retail stores and can be filled with water, the selected attenuation material. Therefore, MCNP simulations for a 3×3 pipe array of three different materials with the determined array dimensions were performed to select the most suitable material.

In order to ensure enough pixels to portray the imaged radiation source, the number of pixels, n had to be determined. An arbitrary size of 23×23 was chosen, totaling to n = 529 pixels for the collimator. This means that instead of the previously simulated 3×3 array, the PVC pipes were modeled to be arranged in a 23×23 array. With the current physical architecture determined, another set of simulations were performed by having the 23×23 PVC collimator filled with water over a 25 cm × 25 cm area and surrounded by varying width of water, w at a fixed water height, 70 cm. The water width, w was varied by changing the radius of the cylindrical tank. This was to establish the amount of water needed around the collimator to prevent interference from photons scattered off of

materials surrounding the imaging system. This ensured that only the photons directly from the radiation source, through the air-filled pipes, were being detected at the base of the collimator and the scattered photons at lower energies are minimized.

Lower energy photons are more likely to interact and get detected by the detectors and thus contribute to the noise in the measurements. Therefore, it is important to optimally minimize these photons against the buildup photons resulted from the increase of water volume around the collimator. The currents from photons with energies less than 662 keV were analyzed because these photons were more likely to contribute to noise in the measurements. The currents of 662 keV photons remained constant for all water width, w values. Similar to the previous analysis, the difference between the photon currents calculated from the F4 tally and the F1 tally for less than 662 keV was used to observe any undesired contribution of lower energy photon detection through the sides of the measurement cell.

An updated model with a cylindrical tank of 55 cm radius and the 23×23 collimator array was then prepared to simulate the imaging of a ring gamma source. The collimator pipes were modeled to be filled with either water or air randomly, and each random combination is called a configuration. It was envisioned that the bottom end of the pipes would be sealed with rubber corks to enable the random filling of water and air. A Python code was compiled to generate 300 configurations for the collimator in the form of a 300 ×529 matrix. This matrix is the sensing matrix A as explained earlier in the Foundation section. The A matrix consists of only “1” and “0” values, in which “1” represents air and “0” represents water.

Mathematically, “0” represents the attenuation of photons by water and “1” results in the photons to travel along the pipes and get detected at the bottom of the collimator. It was envisioned that pipes would have been sealed at the bottom of the collimator to make the pipes that are assigned with the value “1” in matrix A to be filled with air. Therefore, the MCNP model for the experiment included rubber corks at the bottom end of the collimator.

The matrix A has 300 rows, representing the 300 different configurations. It has 529 columns because there is a total of 529 pipes representing the pixels, n. Hence, each row in matrix A describes the water-air combination for each configuration. The number of measurements, m = 300 (56.7% of n) was chosen as it was expected according to Eq. 1 that accurate image reconstruction was achievable with measurements that are at 55% of the pixel amount. Each configuration was simulated using MCNP for the 23×23 collimator array and the 662 keV photon current tally resulting from each simulation becomes the row entry for matrix b with the dimension of 300×1.

The source was defined as a ring-shaped gamma source with an energy of 662 keV, placed on top of the collimator with the ring’s center aligned with the center of the collimator’s cross-sectional area. A ring shape was chosen so that it would be easier to qualitatively judge the quality of the reconstructed image as the image was expected to have pixels highlighted in locations that collectively resemble the shape of a ring and show the location of the imaged source. A gamma source with an energy of 662 keV was chosen due to the availability of a 14.8 MBq (400 μCi) ^{137}Cs gamma source for experimental use. The image of the source, x was then reconstructed using both l_1-*MAGIC* code and

lsqnonneg in *MATLAB*. The image, x was plotted on a grayscale using the *MATLAB imagesc* built-in function, which plots the normalized values of elements in x.

The size of the array was further reduced by half and another set of simulations were performed with an 11×11 collimator array. The corresponding reconstructed image was compared to that of the 23×23 array. The 11×11 array has a total of n = 121 pixels with the matrix A being a 100×121 matrix and matrix b being a 100×1 matrix. Again, the choice of m that is at least half of n, which is 121 for the 11×11 array, resulted in the decision to take m = 100 (82.6% of n) for this array size to ensure that the image recovery is successful.

Based on the determined width of water needed around the collimator, the only shape for a water tank that can hold the required amount of water was found to be rectangular. It was found that a suitable water tank available for the experiment is a 250-gallon industrial-grade reusable container known as the intermediate bulk container (IBC). The consequent simulations would be performed with the IBC as the container that hold the water and the PVC collimator, including a metal cage that supports the IBC and the rubber corks that seal the bottom end of the collimator.

3.1.1.4. The detection subsystem

Next is to determine the physical architecture for the detection subsystem. The types of detector considered to be used are scintillator, semiconductor and Geiger Muller (GM) detectors. The IBC comes with a metal cage that surrounds it and is attached to a pallet base mount. The space between the metal cage and the concrete floor would be the space where the detection subsystem is placed. This limited space presents a constraint for

the detection subsystem. It was determined that a collection of GM counters would be suitable as it would make a relatively small and easy to assemble system compared to the other two types of detector.

It was also important to determine the quantity and the arrangement of the detectors to optimize image reconstructions. Simulations were performed for groups of two, four, six and eight cylindrical air volumes to model the GM detectors. These volumes were designated with a flux tally (F4 tally in MCNP) to count the total flux in the volumes, which would then be converted to expected counts. The availability of only six GM detectors for the experiment becomes another design limit for the subsystem. With six GM detectors, another set of simulations was performed for different arrangements which were block, radial and "fishbone" arrangements.

3.1.1.5. Defining test cases

The final set of simulations address the test cases that will be compared against experiment results. Four different cases that describe different source positions are defined in order to demonstrate the system's ability to localize and identify the source shape, to see the effect of distance from the collimator to the reconstructed image, and to observe the effect of shielding on the radiation source. These four cases used the same 300 collimator configurations but with different source positions.

The first case was defined as the gamma source positioned on top of the collimator in the middle of the cross section. The second case had the same definition as the first case but the gamma source was placed 27.94 cm above the collimator. This will be realized in

the physical experiment by using a plastic source holder of the same height. The third case was defined as the second case but with a piece of aluminum alloy positioned underneath the gamma source by placing it on top of the collimator. The fourth case was defined as the gamma source positioned somewhere near the bottom right part of the top of the collimator. These cases are depicted in Fig. 3-1.

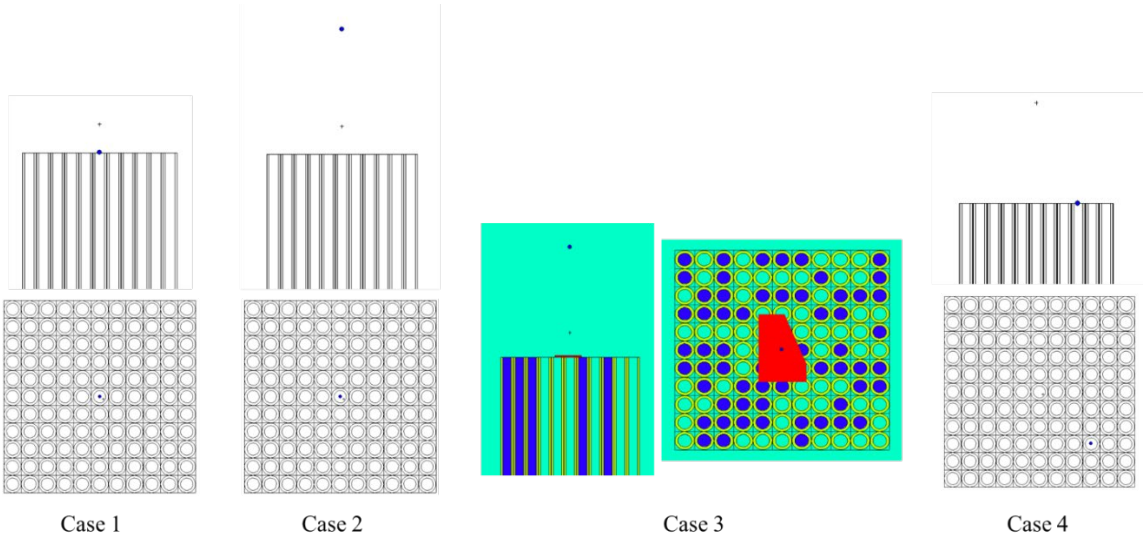

Figure 3-1. The test cases defined with different positions of gamma source (blue dot) for comparison between simulations and experimental results. Blue area represents water, red aluminum alloy, yellow PVC and cyan air.

A 14.8 MBq (400 μCi) ^{137}Cs gamma source in the shape of a small pellet with a diameter of 0.5 cm and a height of 1 cm is available for use in the experiment. This source can be considered as a point source because the detection of the source will be done at least three times the largest source dimension away [2]. Hence, simulations with the final model were performed with a point ^{137}Cs source instead of a ring source used in previous simulations.

The four cases of different source positions are summarized in Table 3-1. For Case 3 in the experiment, an aluminum alloy piece will be placed on top of the collimator and below the gamma source. This will be done to observe the effect of shielding of the gamma source and if object (active) imaging was possible with this system. The shape of the aluminum alloy piece, which is available for use in the experiment, is shown in Fig. 3-2. These test cases were simulated and the source image, x for each of the four cases was recovered using the built-in NNLS algorithm in *MATLAB*.

Table 3-1. The gamma source position for each case, with the "above" position being 27.94 cm above the collimator (held by a plastic source holder).

Case	Source position
1	On top of collimator, middle
2	Above the collimator, middle
3	Above the collimator, middle, with an aluminum alloy piece below it
4	On top of collimator, near bottom right corner

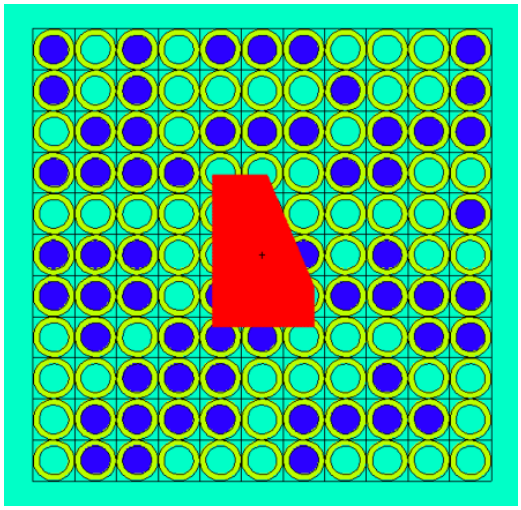

Figure 3-2. The shape of the aluminum alloy piece used in Case 3.

3.3. Results and Discussion

3.3.1. The attenuation subsystem

The water height was varied to find the needed height to attenuate 662 keV photons from a point source positioned 130 cm above the concrete in the middle of the cylindrical water's cross-sectional area by at least 99.5%. The minimum height was determined to be 60 cm, as shown in Table 3-2, which caused a reduction of 99.45% of 662 keV photons, presenting roughly 2.77% of the average annual background dose of 3 mSv/year. A water height of 70 cm was chosen for the consequent sets of simulation.

Table 3-2. The calculated attenuation and dose rate at the bottom of a 60.96 cm wide water cylinder of various height.

h (cm)	F1 (662 keV γ s^{-1})	F4 (662 keV γ cm^{-2} s^{-1})	Attenuation (%)	Dose rate (mSv yr^{-1})
0	444212	153.21	0.00	15.035
10	186648	64.3743	57.98	6.317
20	78293.2	27.0014	82.38	2.650
30	32800.8	11.319	92.61	1.111
40	13900.9	4.79726	96.87	0.471
50	5915.74	2.04068	98.67	0.200
60	2440.52	0.842385	99.45	0.083
70	1031.56	0.356189	99.77	0.035
80	427.72	0.147295	99.90	0.014
90	165.112	0.056947	99.96	0.006
100	56.61	0.019684	99.99	0.002
110	34.595	0.012031	99.99	0.001

3.3.2. The collimator subsystem

Figure 3-3 shows that the currents calculated from the F4 tally were statistically the same as the F1 tally currents in terms of the trend even though magnitudes are different; there were no significant contribution from undesired photons coming from the sides of the measurement cell in the detection. The error bars are so large because uncertainties were propagated from multiplication with the measurement cell area and subtraction of the value of currents. The increasing propagated uncertainties were mainly contributed by the measurement cell area which was treated as a constant and this constant value increased with the cell radius by r^2. This result shows that the dimensions of the collimator are only limited by the dimensions of the water tank as the collimator must be smaller than the water tank. Therefore, the collimator dimensions were set to be 25 cm × 25 cm as these dimensions were deemed to be practical for the proposed proof-of-concept system.

MCNP simulations for a 3×3 pipe array of three different materials with the determined array dimensions were performed to select the most suitable material. These simulations resulted in PVC to be selected because as shown in Fig. 3-4, the PVC has a good photon attenuation capability compared to the other two materials when the pipes were all filled with water, and it did not excessively absorb the photons when the pipes were all empty, which was good to ensure high signal-to-noise ratio. PVC pipes are also the least expensive material compared to the other two materials.

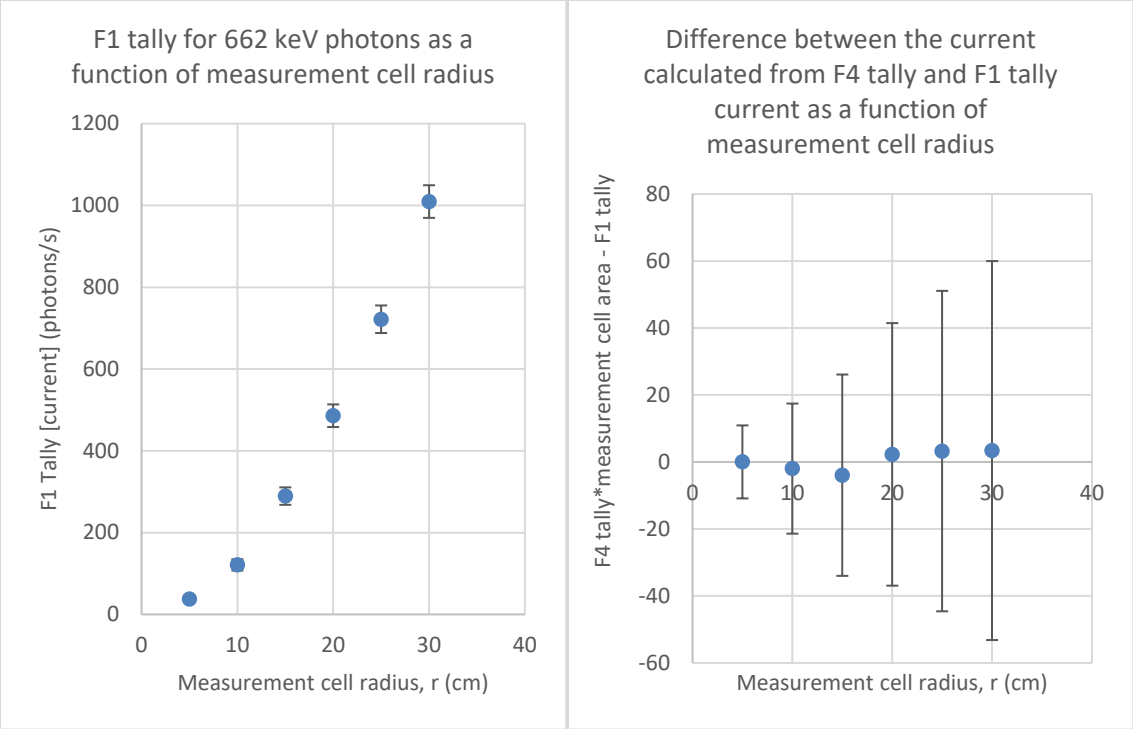

Figure 3-3. The 662 keV photon current from F1 tally plotted against the measurement cell radius, r (top) and the difference between the current calculated from F4 tally and the F1 tally current plotted as a function of r (bottom).

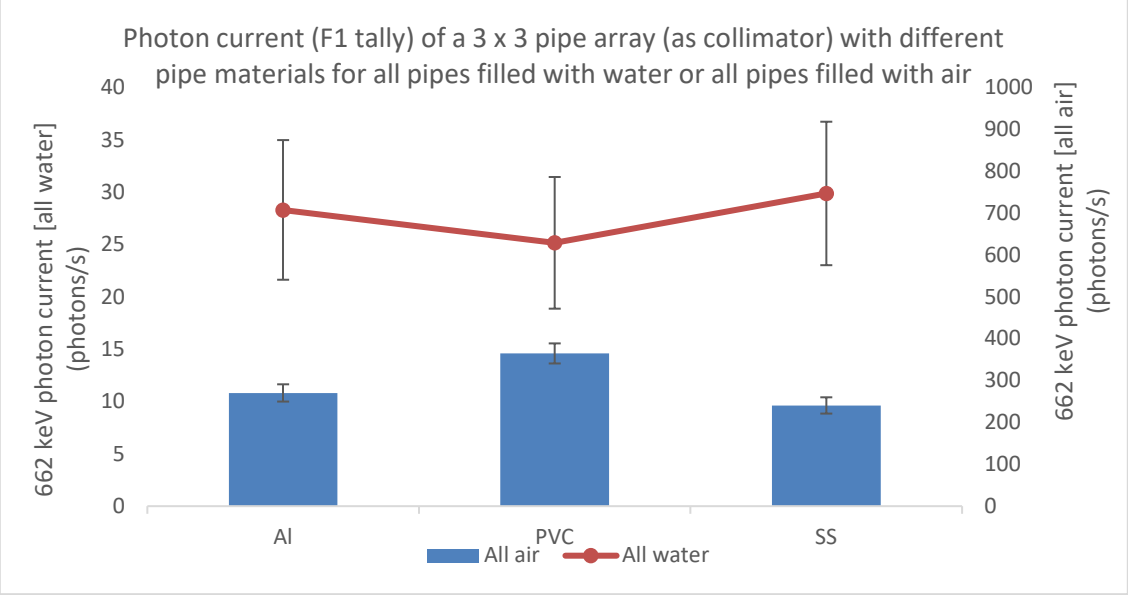

Figure 3-4. The calculated attenuation and dose rate at the bottom of the cylindrical water of various height.

The minimum radius of water around the sides of the collimator was found to be 55 cm. Figure 3-5 shows the possible photon interactions with the concrete floor and within the measurement cell. The difference between the F4 tally multiplied by the area of measurement cell and the F1 tally across the top of the measurement cell area gives a rough estimation of the scattered photons into the measurement cell.

Figure 3-6 shows that the difference in currents for photons that are less than 662 keV became statistically the same starting at w = 55 cm as w was increased. The error bars are large because uncertainties were propagated from the multiplication and subtraction operations. The approximately similar magnitudes of error bars are due to the use of the same measurement cell area in computing the difference between the current calculated from the F4 tally and the F1 tally current. The difference in currents also decreased significantly at w = 55 cm compared to when w = 30 cm. This indicates that interference from these lower energy photons (<662 keV) within the measurement cell was minimized at w = 55 cm.

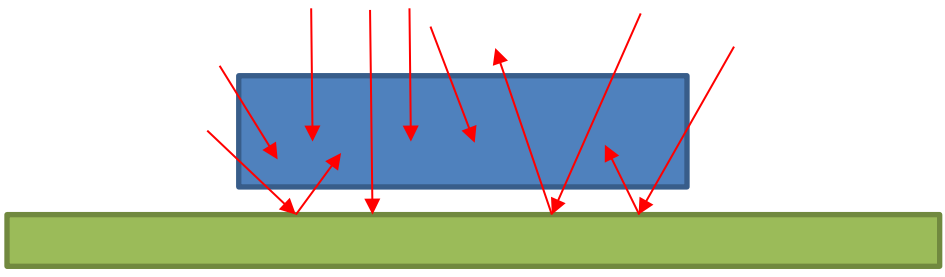

Figure 3-5. The schematic of photon interactions with the concrete floor and within the measurement cell.

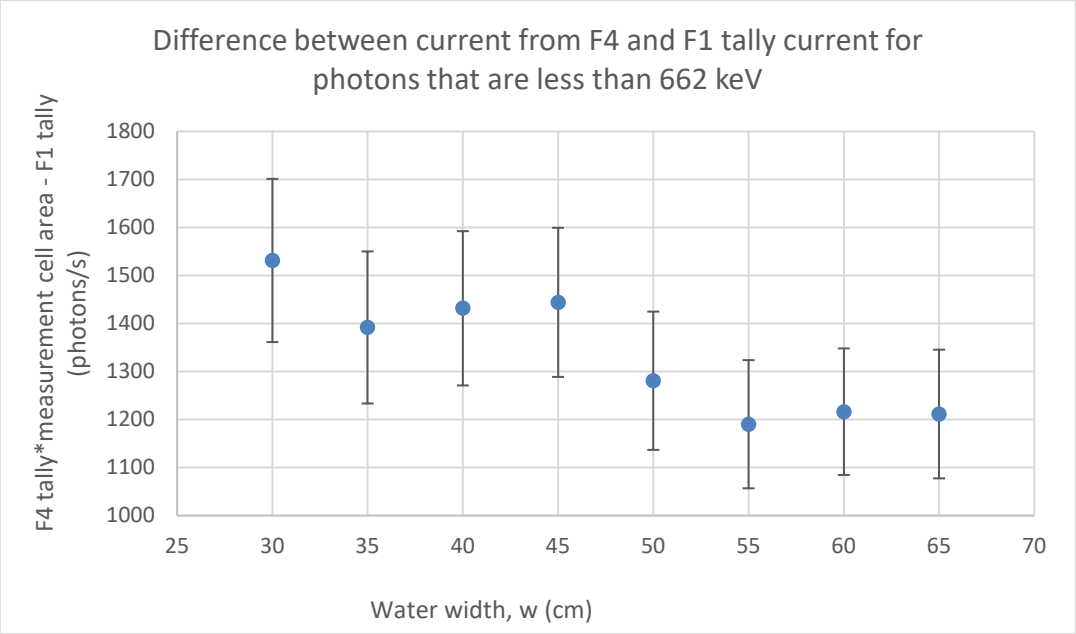

Figure 3-6. The calculated attenuation and dose rate at the bottom of the cylindrical water of various height.

The image of the ring-shaped source, x was reconstructed using both l_1-*MAGIC* code and *lsqnonneg* in *MATLAB*. It was found that the image reconstruction was a success as shown in Fig. 3-7. Images produced by using the *lsqnonneg* function were found to be better and this had led to the use of image outputs from the *lsqnonneg* function for the remaining of the simulation results.

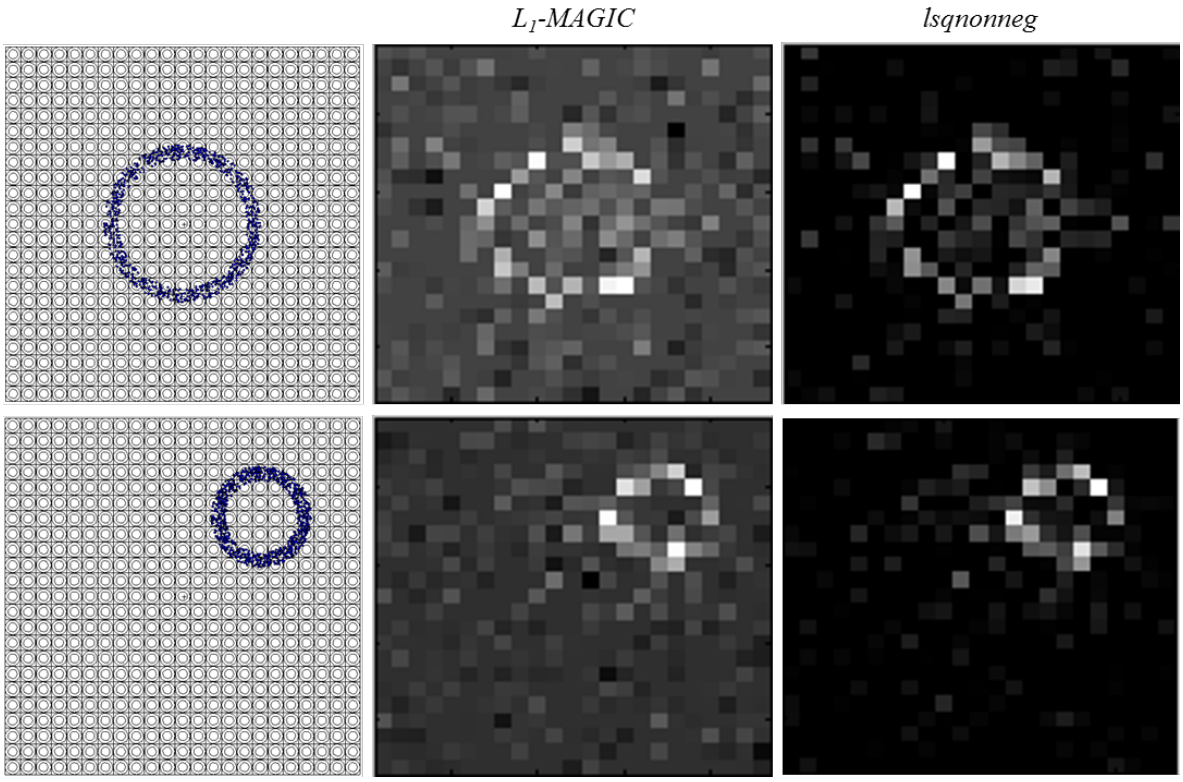

Figure 3-7. The reconstructed image using 23×23 array of a ring gamma source, placed in the center of the collimator top and of a smaller ring gamma source placed in the first quadrant of the collimator's cross-sectional area using l_1-*MAGIC* code and *lsqnonneg* func*tion in MATLAB.*

It was expected that the image resolution produced with lower number of pixels would result in a less defined image. This is evident when comparing the images in Fig. 3-8. Even though the resolution was degraded for the smaller array size, the ring shape was still distinguishable and the position was accurately located. It was decided that the 11×11 size would be a suitable and practical choice for an experiment.

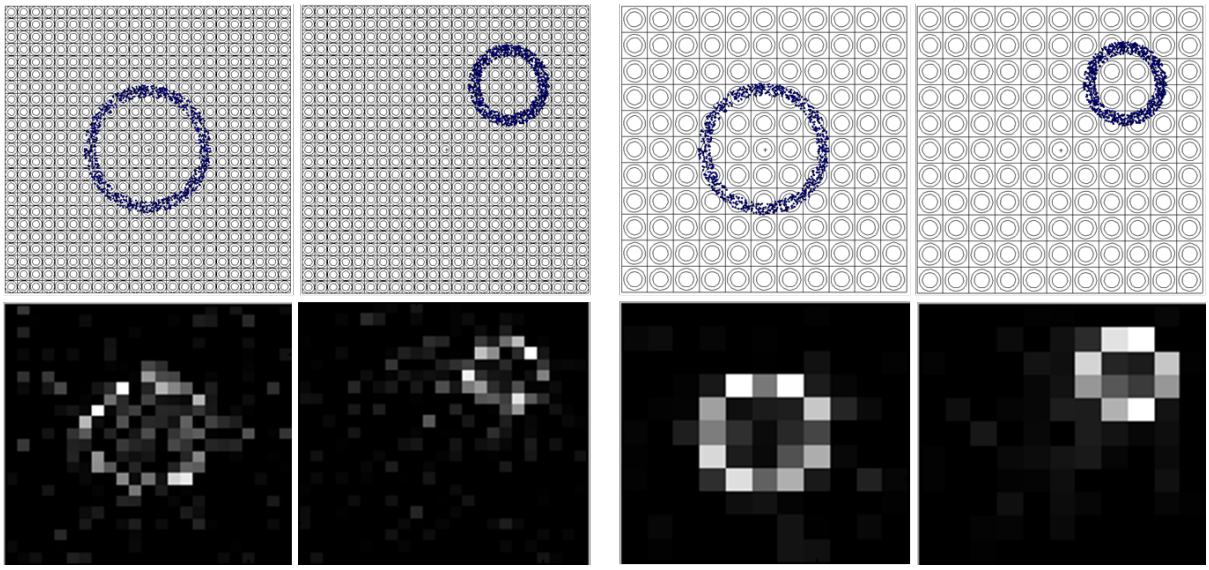

Figure 3-8. A comparison between the images reconstructed using the 23×23 array (left) and the 11×11 array (right) using the same ring gamma source, reconstructed using *lsqnonneg* function in *MATLAB*.

3.3.3. The detection subsystem

Simulations were performed for groups of two, four, six and eight cylindrical air volumes to model the GM detectors. It was found that the more the detector used, the better the image quality. Figure 3-9 shows that there needs to be at least six detectors that must be used in order to have image quality that allows for correct localization and shape identification.

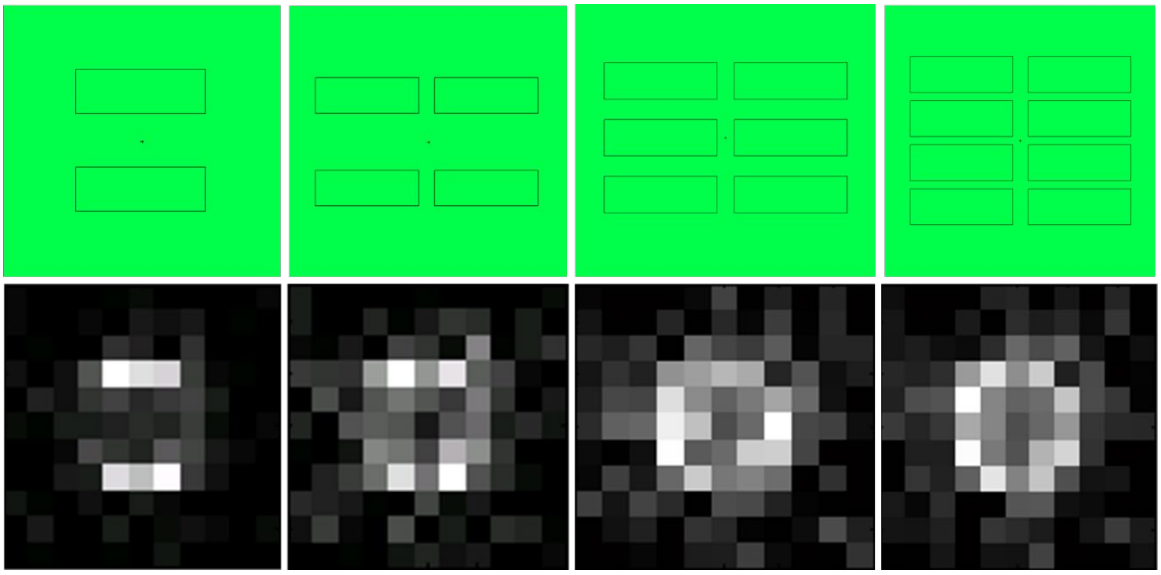

Figure 3-9. The reconstructed images for different numbers of GM detectors used in the simulated measurements.

With six GM detectors, another set of simulations was performed for different arrangements which were block, radial and "fishbone" arrangements. Figure 3-10 shows the results for each corresponding arrangement. It was found that the radial arrangement allows for better shape identification. With these simulations results, it was decided that the six GM detectors in radial arrangement would be employed for the experiment to validate the simulation results.

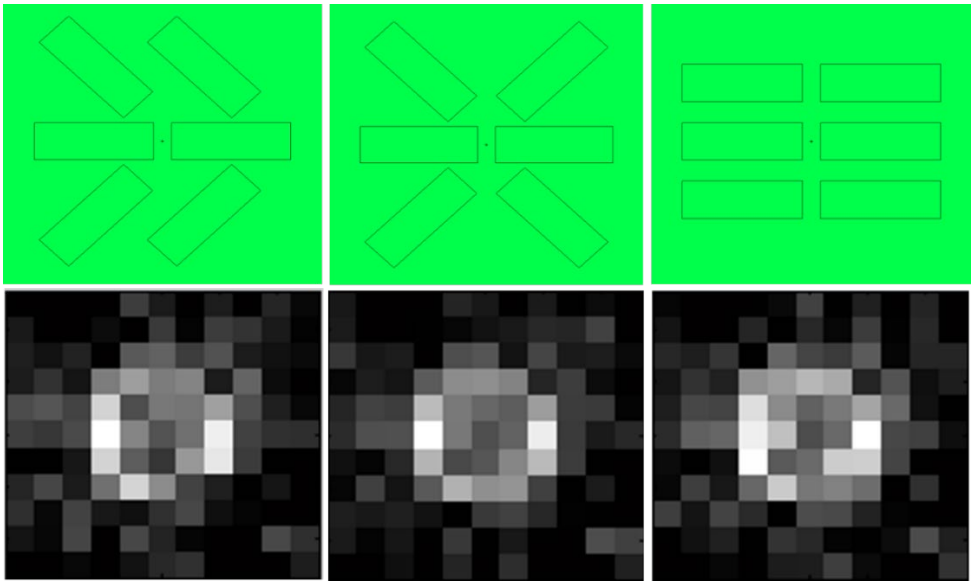

Figure 3-10. The reconstructed images for different detector arrangements used in the simulated measurements; (from left) “fishbone”, radial and block.

The complete MCNP model with all attenuation, collimator and detection subsystems based on the available materials for the experiment is shown in Fig. 3-11. The complete system shown in Fig. 3-11 includes the modeling of the rubber corks at the end of the pipes and the metal cage that holds the tank. The cross-sections of the metal tubes that make up the cage are visible in the Visual Editor (VISED) image. However, the material color that was assigned to the metal cage is not visible as the thickness of the metal tubes is small compared to the overall dimensions of the whole system.

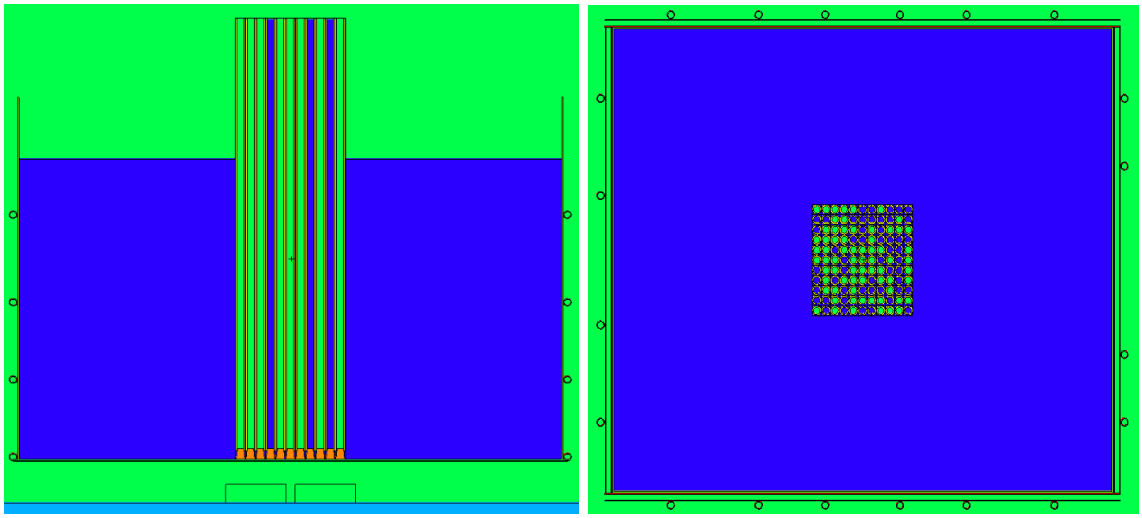

(a) (b)

Figure 3-11. The MCNP model of the source imaging system generated by the MCNP Visual Editor software, showing (a) the cross-sectional view of the system on the x-z plane at y = 10, and (b) the top view of the system, both pictures showing an example of the collimator's random configuration. Blue color represents water, green air, orange rubber corks, cyan concrete and red polyethylene (water tank).

3.3.4. Test cases simulation results

These test cases as listed in Table 3-1 were simulated and the source image, *x* for each of the four cases was recovered using the built-in NNLS algorithm in *MATLAB*. The results in Fig. 3-12 show that image reconstruction of the point gamma source was simulated to be successful. Case 1 and Case 4 reconstructed images accurately showed the correct location and shape of the gamma source. Even at almost 30 cm away, the reconstructed image in Case 2 accurately showed the position of the point source even though the image was relatively noisy.

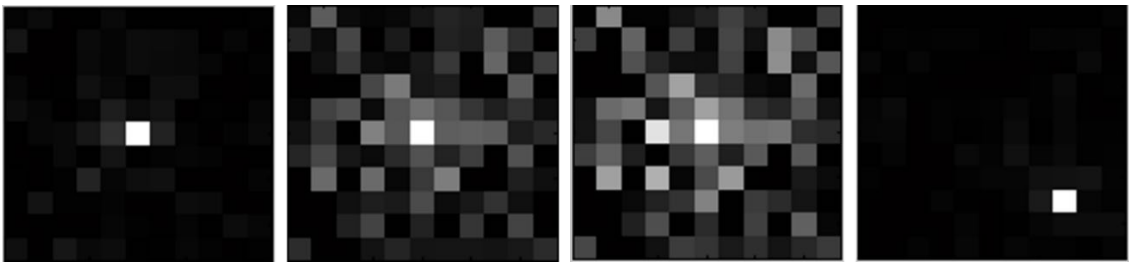

Figure 3-12. The results of image reconstruction using NNLS, from left to right, for case 1 (on top of collimator, middle), 2 (above the collimator, middle), 3 (above the collimator, middle, with an aluminum alloy piece below it), and 4 (on top of collimator, near bottom right corner).

The third case showed that if a point gamma source was shielded by a 1-cm thick aluminum alloy and was placed further away from the collimator, it was still possible to localize the source. However, the shape of the aluminum alloy was not visible in the reconstructed image, indicating that active imaging may not be feasible for this particular setup. The results depicted in Fig. 3-12 serve as the expected results from the physical experiment which is planned to be performed.

3.3.5. Experimental planning

The radiation source imaging system has been prepared based on the design activities using the systems engineering process and MCNP simulations. This setup is shown in Fig. 3-13 (a). There are six Ludlum Model 44-7 GM detectors, each connected to a Ludlum scaler-ratemeter Model 2200 (Fig. 3-13 (b)). Water is filled in the tank to a height of 79.38 cm and the collimator is placed upright in the center of the tank. Water and air combination is based on the same configurations used in simulations, and is made possible with the help of water pumps. The preliminary result comparison between simulation and experimental results will be performed for two initial collimator

configurations: an all-empty and an all-full configurations. The experiment will then be performed for four different cases as summarized in Table 3-1 and depicted in Fig. 3-14.

One hundred measurements for each case defined in Table 3-1 will be performed, corresponding to the 100 different collimator configurations simulated. For every measurement, the GM detector counts will be collected and summed, representing the elements in matrix b. Experimental images reconstructed from the 100 different collimator configurations will then be compared with simulated images developed using the same reconstruction techniques. The data from simulations and experiments will be analyzed and discussed to determine the feasibility of the proposed radiation source imaging concept. Based on the analysis results, design improvements will be suggested, if necessary, for potential testing in the future. These suggestions might include some constraint relaxation such as the removal of minimal cost as one of the design requirements.

(a) (b)

Figure 3-13. The experimental setup showing (a) the radiation source imaging system without the source, and (b) the arrangement of six GM detectors placed beneath the tank (not connected to ratemeters in the picture).

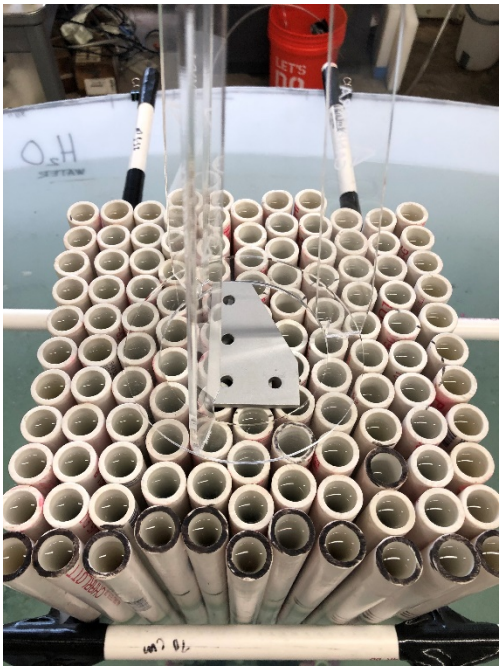

Figure 3-14. The experimental setup for Case 3 (source above the collimator, in the middle, with an aluminum alloy piece below it). This is the same setup for Case 2 but without the aluminum alloy piece. For Cases 1 and 4, the plastic source holder is removed and the source is placed directly on the collimator in the middle for case 1, and near the corner of the collimator (marked-black pipe) for Case 4.

The experiment is expected to take seven weeks to complete. Each measurement will take a total of 45 minutes; 15 minutes to remove and fill water in the pipes according to the matrix A used for simulations, 15 minutes for the actual measurement, and 15 minutes for background measurement without a source. Each day will be allocated with three measurements that will take at most three hours to complete. The experiment will be completed in roughly seven weeks if measurements are performed every working day. Data processing will take another one to two weeks and discrepancies will be expected because of the difference in the environment, geometry and heterogeneity of the materials involved.

The data trend is expected to be the same and similarity in the data trend will indicate that the simulation and physical systems are behaving similarly. Any major discrepancies in the actual and expected measurements will be solved by making amendments to the simulation model so that the expected results match the experiment results. This is because the simulation model is a much simpler representation of the actual components and it is more realistic to increase the complexity of the simulation model rather than decreasing the complexity of the actual system components. Once the results statistically match, further investigation on collimator and detector systems will be made to improve image reconstruction capability.

3.4. Conclusion

The incorporation of CS principles in imaging system designs, especially in the hardware design, is new in nuclear or radiological security. This research will present a novel design concept that can be applied in creating an alternative system to support monitoring and interception of radiological sources or nuclear materials illegal movements across nations. This would be done by validating the simulation results against experimental measurements and identifying aspects that can be enhanced and improved in both the system design and the system simulation model. The process of designing a radioactive source imaging system using CS principles and the performance of the proposed prototype based on the design constraints of the research have been demonstrated using MCNP simulations. Successful cross-validation between these experimental and simulation results will hopefully encourage further exploration of CS principles application in nuclear security.

3.5. References

[1] "Systems Engineering Fundamentals." Defense Acquisition University Press, Jan. 2001. Accessed: Sep. 20, 2021. [Online]. Available: https://loyp.ru/images/documents/systems_engineering_fundamentals_(defense _acquision_university).pdf

[2] J. J. Bevelacqua, "Appendix II: Basic Source Geometries and Attenuation Relationships," in *Contemporary Health Physics*, John Wiley & Sons, Ltd, 2009, pp. 565–571. doi: 10.1002/9783527626809.app2.

4. VALIDATION OF MCNP-SIMULATED GAMMA MEASUREMENTS USING GM DETECTORS

4.1. Introduction

There are several publications on the Monte Carlo N-Particle (MCNP)[1] radiation transport simulation of Geiger-Müller (GM) detectors [2], [3] and [4]. However, these publications did not provide the details on how to process the MCNP output results (or tallies) to accurately estimate radiation count rate in the GM detector. In addition, the tallies used in these aforementioned publications are different than the ones suggested in this paper. The use of surface current (F1 tally) and pulse height (F8 tally) estimators are found in literature to estimate radiation count rate in the GM detector.

This paper offers a different method to estimate the GM detector's gamma response by using tallies other than F1 and F8, which would be beneficial for certain types of problems. For example, using F1 tally requires the need for cosine binning option that would track photons crossing the designated surface in only one direction to avoid multiple counting due to backscattering interactions. However, this method would then assume that any photons crossing the surface will result in a pulse signal. Depending on the energy of the photons, a pulse signal might not result in the detector especially for photons with lower interaction probabilities. The F8 tally works best for spectroscopy, in which energy distribution of pulses registered in the designated cell is often utilized to plot the resulting spectrum. GM detectors function as counters that do not preserve energy information of the photons. Modeling a GM detector using the F8 tally would not be accurate because this assumes that the simulated GM detector does not utilize the Geiger

discharge process. As an alternative, this paper suggests the use of the cell flux tallies to model GM detector response.

The objective of this paper is to investigate two methods of simulating GM detectors for gamma radiation detection and to determine which method better represents physical measurements from a proposed gamma source imaging system that uses compressed sensing principles [5–9]. This validated system model, described in Section 3.1.4., could serve as a baseline model in which design modification can be made to improve and test the system prior to time-consuming physical experiments.

The two methods demonstrated in this paper employed the cell flux (F4 tally) and energy cell flux (*F4 tally) estimators in quantifying the GM detector's gamma radiation response using a set of experiments. The differences in the estimated radiation counts using these tallies are analyzed and discussed by comparing them with experimental results. One of the methods was selected to be used in the validation of the proposed system for imaging gamma radiation sources. The validation compares the expected radiation counts derived from MCNP simulations, using the selected MCNP tally-processing method, to physical measurements for two experimental configurations.

Since model validation is easier for a simple geometry, this research started with a simple source-detector geometry. Based on the results of this simple arrangement, the complexity of the system was increased by adding the collimator and water-filled tank, with the collimator channels either fully filled with water or fully filled with air. These two configurations (all-full and all-empty) are the most basic configurations of the proposed gamma source imaging system. This is important because model validation helps

to establish a transparent and verifiable method for design improvements of the proposed system. The validated model can then be applied to other areas in the fields of nuclear security, safety, and nonproliferation. One example is the integration of the proposed system in monitoring transport of radioactive materials through ports of entry. A thoroughly validated and verified simulation model would be valuable in implementing the system's integration into the existing nuclear and radiological materials security program.

4.1.1. Overview of how GM detectors work

GM detectors (also known as GM tubes) are widely used for radiation detection. The radiation types detected by GM tubes are gamma, beta, and alpha radiation. Alpha and beta radiation interact with the gas in the GM detector through ionization and excitation. The resulting ion-pairs are then accelerated across the potential applied between the anode and the cathode of the detector. The electrons move towards the anode, and positive ions move towards the cathode. The accelerated electrons cause further ionization in the gas of the GM detector, resulting in signal multiplication, eventually creating the Townsend avalanche.

The creation of a Townsend avalanche can induce multiple other avalanches at different positions along the anode. The collection of multiple avalanches is called the Geiger discharge, which gives the same pulse size regardless of the energy or type of incident radiation [10]. The electrons are collected at the anode and produces a signal that denotes the presence of a radiation interaction in the detector. These signals are counted by a single-channel analyzer (SCA) over a pre-set period of time. The count rate from the

source can then be divided by the system's efficiency to determine the activity of a radioactive source.

Unlike alpha and beta radiation, gamma radiation primarily interacts with the tube's aluminum casing, ejecting electrons from the metal into the fill gas (neon) [10]. These energetic electrons then interact the same way in the fill gas (ionization and excitation), resulting in signal output as explained previously.

4.1.2. Detector and source arrangements of the study

The detector arrangement in this study is adopted from that of the proposed system. Two source arrangements are used in this study; one is denoted as the floor measurement and another as the holder measurement. Both consisted of six GM detectors radially placed on a concrete floor as shown in Fig. 4-1. These arrangements differed by the source position in relation to the GM array. A 14.8-MBq (0.4-mCi) ^{137}Cs source is used in both arrangements. Due to the large dimension of the proposed system, a high-activity source was needed to account for the long distance between the detection system and the source. The same gamma source was used for the simplest geometry validation as well.

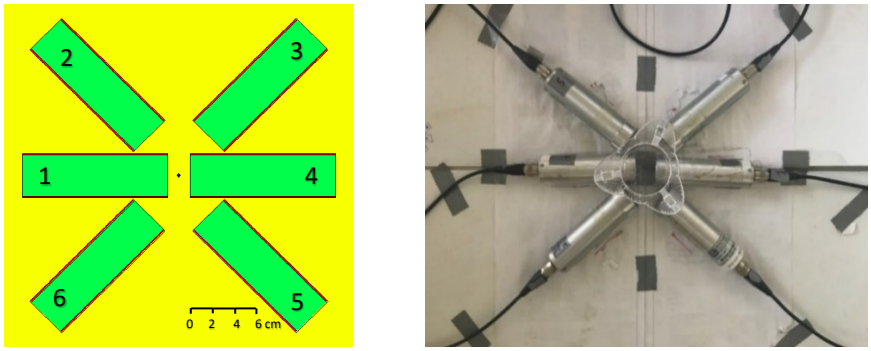

Figure 4-1. The top view (x-y plane) of the detector placement on a concrete floor illustrated in the MCNP Visual Editor (VISED) program (left) and a top view of the detector arrangement with a plastic source holder above the detectors. (right).

In the floor measurement, the ^{137}Cs source was placed on the floor in the middle of the detectors' radial arrangement. This set-up is shown in Fig. 4-2 (a). In the holder measurement, the ^{137}Cs source was placed 27.94 cm above the center of the detector arrangement as shown in Fig. 4-2 (b). In the physical experiment, the source was placed on a source holder made of plastic. Radiation counts from each detector were obtained for one minute.

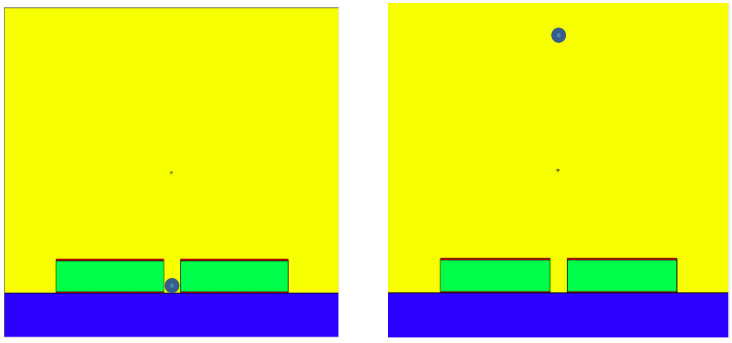

(a) (b)

Figure 4-2. The side view (x-z plane) of the two parallel detectors for (a) floor configuration, and the (b) holder configuration. The blue dot shows the position of the ^{137}Cs source.

4.1.3. Compressed sensing technique using non-negative least squares

Compressed sensing is a technique that allows for the sampling of limited data to reconstruct a complete data set. The simplest example is the way pictures are stored in a computer memory. Current software stores high-quality pictures in smaller data files. This is done by converting the image matrix into a sparse matrix, that contains very few non-zero elements. A typical criterion is that the number of non-zero elements is, at most, equivalent to the number of rows or columns of the image matrix. Only non-zero elements are stored compared to the total elements that make up the whole image. When the user opens the image file, the system then performs the reverse of the conversion process from the stored non-zero elements, producing the original image.

There are different ways of performing this conversion such as [11], [12] and [13]. An alternate non-negative least squares method is employed in this research to an under-determined system (a mathematical problem with more unknowns than the number of equations or constraints available to obtain a unique solution) by l_2-minimization with a non-negative elements requirement. Traditionally, measurements as many as the total number of elements representing the solution (pixels) is needed for image reconstruction. The proposed system, utilizing compressed sensing, allows for an image of a gamma radiation source to be reconstructed from a number of measurements that is less than the total amount of pixels that represent the image. The total number of pixels is equivalent to the total channels in the collimator array of the proposed system.

4.1.4. Proof-of-concept gamma source imaging system

The proposed system was initially developed using the Monte Carlo N-Particle (MCNP) code for imaging neutron sources [14]. Design adjustments are made to the proposed system for the application of imaging gamma radiation sources instead. A primary component of the proposed system is a collimator array made of 11-by-11 polyvinylchloride (PVC) pipes of 1.27-cm radius. It is placed upright in the middle of a water-filled 250-gallon rectangular tank. Beneath the tank, six GM detectors are placed in a radial arrangement with each connected to its own ratemeter. The details of the design process are discussed by Anuar et al. [14].

The PVC pipes that make the 11-by-11 collimator are filled with either water or air in a random combination. The random water-air combination is generated using a Python code and as many as 100 combinations are generated. Each combination is called a configuration and measurement readings from the GM detectors beneath the tank are recorded for each configuration. The gamma source to be imaged is placed above or on top of the collimator. The counts recorded are processed using the non-negative least squares algorithm in MATLAB to produce an image with a total of 121 pixels. The resulting image indicated the location and shape of the gamma source, which was a point source in this research.

Before experimental measurements are completed, initial validation of the proposed system model was needed. Validation was done by comparing the MCNP-simulated response to the measured counts collected from the proposed system. Two

collimator configurations were investigated: the all-full and all-empty configurations. An illustration of these two configurations is shown in Fig. 4-3.

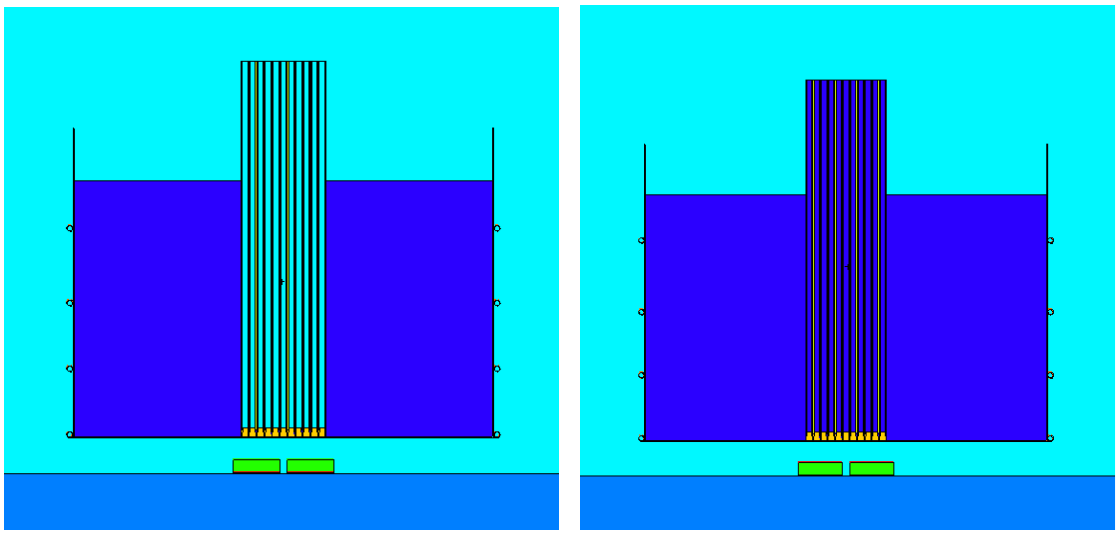

(a) (b)

Figure 4-3. The side view of (a) an all-empty and (b) an all-full configuration.

4.2. Methods

4.2.1. Estimate of the analytical solution of the expected counts

Firstly, the detector counts are estimated by analytical calculations. This is useful because it offers transparency to the problem as the effect of the defined variables on each other can be assessed in the formulation. The analytical solutions for the expected detector counts provided an upper and lower bound of the estimated counts. These values, together with the expected counts from simulations and the actual measurements allowed for validation to be performed.

Mathematically expressing radiation interactions with matter accurately is difficult. To aid in the calculation, several simplifications and assumptions are made in

deriving the equations. The expressions for the detector expected counts are as shown in Eq. 4-1 and Eq. 4-2. Figure 4-7 helps in visualizing the interactions in both arrangements.

$$\text{Expected counts (floor)}, \mathrm{N}_{sf} = \left[\begin{array}{c}\text{photons that interact only with aluminum} \times \text{scattering probability} \\ + \text{photons that interact only with gas}\end{array}\right] \times \text{time} \qquad (4-1)$$

$$\text{Expected counts (holder)}, \mathrm{N}_{sh} = \left[\begin{array}{c}\text{photons that interact with aluminum} \times \text{scattering probability} \\ + \text{photons that do not interact with aluminum but then do with gas}\end{array}\right] \times \text{time} \qquad (4-2)$$

To accurately calculate the expected counts, these equations should be integrated over the relevant energy range, which depends on the type of radiation source, as well as over the thickness and volume of the two different materials that make up the detector. This is cumbersome to solve; hence a set of assumptions are made to simplify the equations.

The first assumption made is that all of the photons interacting in the detector have an energy of 662 keV being emitted by ^{137}Cs source. The second assumption made is that the average distance traveled, $\tilde{t}$ by the photons in the respective detector materials is constant. The parameter $\tilde{t}$ is not the mean free path of the photon. Instead, it is just an average distance assumed for these calculations based on the geometry of the setup (floor or holder). These assumptions reduced Eqs. 4-1 and 4-2 to Eqs. 4-3 and 4-4. Table 4-1 shows the approximated parameters for both arrangements.

$N_{sf}\,[min^{-1}]$ =

$$\frac{S}{4\pi} \times \Omega_f \times \left[(e^{-\mu_{Ne} \times \tilde{t}_{Ne,f}}) \times (1\text{-}e^{-\mu_{Al} \times \tilde{t}_{Al,f}}) \times P_{scatt,f} + (1 - e^{-\mu_{Ne} \times \tilde{t}_{Ne,f}})\right] \times 60\ \text{s} \quad (4-3)$$

$N_{sh}\,[min^{-1}]$ =

$$\frac{S}{4\pi} \times \Omega_h \times \left[(1 - e^{-\mu_{Al} \times \tilde{t}_{Al,h}}) \times P_{scatt,h} + (e^{-\mu_{Al} \times \tilde{t}_{Al,h}}) \times (1 - e^{-\mu_{Ne} \times \tilde{t}_{Ne,h}})\right] \times 60\ \text{s} \quad (4-4)$$

Where:

S = source strength (gammas s^{-1})

Ω_f = solid angle for the floor arrangement (ster)

Ω_h = solid angle for the holder arrangement (ster)

μ_{Ne} = linear attenuation coefficient in neon (cm^{-1})

μ_{Al} = linear attenuation coefficient in aluminum (cm^{-1})

$\tilde{t}_{Ne,f}$ = mean distance traveled in neon for the floor arrangement (cm)

$\tilde{t}_{Al,f}$ = mean distance traveled in aluminum for the floor arrangement (cm)

$\tilde{t}_{Ne,h}$ = mean distance traveled in neon for the holder arrangement (cm)

$\tilde{t}_{Al,h}$ = mean distance traveled in aluminum for the holder arrangement (cm)

$P_{scatt,f}$ = probability of scattering from aluminum into neon for the floor arrangement

$P_{scatt,h}$ = probability of scattering from aluminum into neon for the holder arrangement

The solid angle, Ω and the probabilities of scattering from aluminum into neon, $P_{scatt.}$ in Eqs. 4-3 and 4-4 were calculated first. Figure 4-4 shows the dimensions of the GM detector. Figure 4-5 shows the details of the source position relative to detector 4 in Fig. 4-1. The Ω is determined by integrating ($\cos \alpha / r^2$) over the area viewed by the source (circular area in floor arrangement and rectangular area in holder arrangement).

The radius of the detector face, *a*, was 2.3 cm. The distance between the source and the detector face in the floor arrangement, *d*, was 1 cm while in the holder arrangement, *h*, was 30 cm. The ^{137}Cs source was placed 27.94 cm (11 inches) above the detectors, but an effective distance between the radiation source and the surface area viewed by the source was assumed to include an additional distance equal to the radius of the detector. The angle α is between the solid r arrow and the normal to the surface area viewed by the source (*d* in the floor arrangement, and *h* in the holder measurement).

For the floor arrangement, the $\tilde{t}_{Ne,f}$ was assumed to be a third of the detector's length (4.4 cm) and $\tilde{t}_{Al,f}$ was a third of the path length in aluminum at half the detector's length and an angle of $\tan^{-1}$ ($2a$-t/(λ/2+d)). For the holder arrangement, the $\tilde{t}_{Ne,h}$ was assumed to be a third of the detector's diameter (1.27 cm) and $\tilde{t}_{Al,h}$ was a third of the path length in aluminum at half the detector's length and an angle of $\tan^{-1}$ ((λ/2+d)/h).

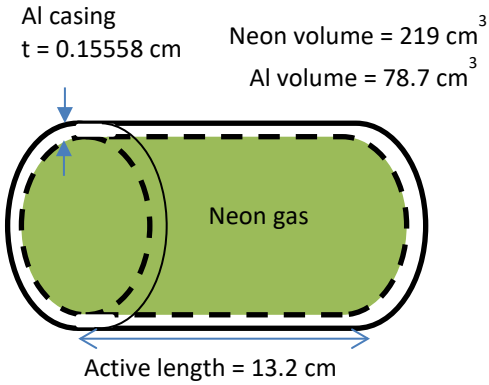

Figure 4-4 The dimensions of the GM detector according to Ludlum 44-7 model [15].

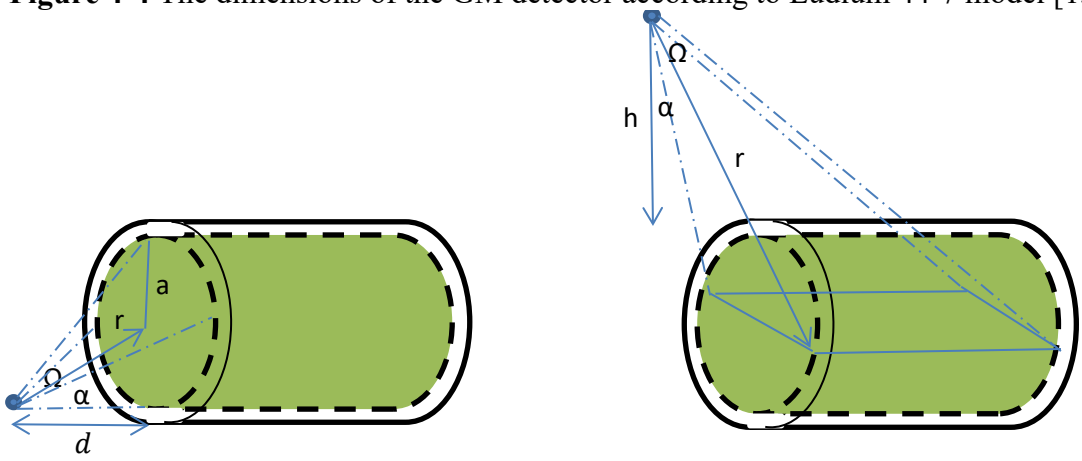

(a) (b)

Figure 4-5. Diagram showing the position of the gamma source relative to a GM detector. This visualization aided in the solid angle calculation in (a) the floor arrangement and (b) the holder arrangement.

The next parameter, P_{scatt}, is estimated using the Klein-Nishina differential cross-section formula as shown in Eq. 4-5. The photon's scattering angle, θ in Eq. 4-5 is determined using the Compton scattering equation as shown in Eq. 4-6. There is a range of θ corresponding to electron recoil angle, ϕ (Eq. 4-7), that contribute to the detector

counts. These ranges of θ and ϕ are determined next for both floor and holder arrangements.

$$\frac{d\sigma}{d\Omega} = \frac{{r_e}^2}{2}\left(\frac{E'}{E}\right)^2\left(\frac{E'}{E}+\frac{E}{E'}-sin^2\theta\right) \quad (4-5)$$

$$\frac{E'}{E} = \frac{1}{1+\frac{E}{m_e}(1-\cos\theta)} \quad (4-6)$$

$$\tan\phi = \frac{\cot\theta}{1+\frac{\lambda_c}{\lambda_0}} \quad (4-7)$$

Where:

$\frac{d\sigma}{d\Omega}$ = differential scatter cross-section (cm^2 $ster^{-1}$)

r_e = the classical electron radius (2.818×10^{-13} cm)

E' = energy of the scattered photon (MeV)

E = energy of the incident photon (MeV)

θ = the angle of scatter with respect to the incident photon's direction (°)

m_e = energy equivalent of electron rest mass (0.511 MeV)

ϕ = the angle of electron recoil with respect to the incident photon's direction (°)

λ_c = electron's Compton wavelength (2426 fm)

λ_0 = incident photon's Compton wavelength (1873 fm)

Figure 4-6 shows a visual depiction of how θ and ϕ are represented for use in Eqs. 4-6 and 4-7. A grazing hit is represented by θ = 0° where the photon is undeflected, resulting in ϕ = 90° (recoil electron arrow pointing downward in Fig. 4-6). A backscattered

photon is represented by θ = 180° where the photon is reflected back in the exact opposite of its initial direction, resulting in ϕ = -90° (recoil electron arrow pointing upward in Fig. 4-6).

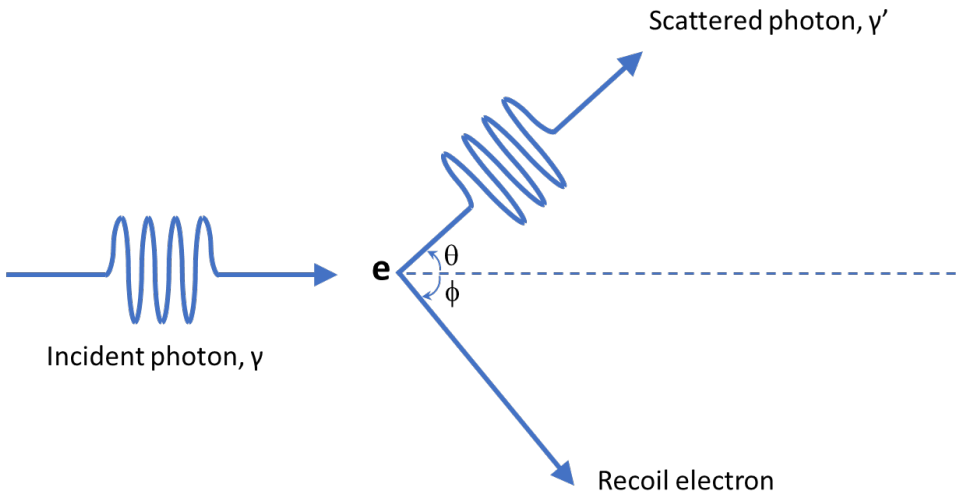

Figure 4-6. A schematic diagram depicting the definition of θ and ϕ in a Compton scatter.

For the floor arrangement, the ϕ that dominantly contributed to detector counts is assumed to be between 50° to 90° and for the holder arrangement, ϕ was between -20° to 20°. These angles corresponded to θ of 0° to 20° for the floor arrangement and 50° to 130° for the holder using Eq. 4-7. Fig. 4-7 shows the estimated ranges of ϕ that are of interest in the calculation of P_{scatt}.

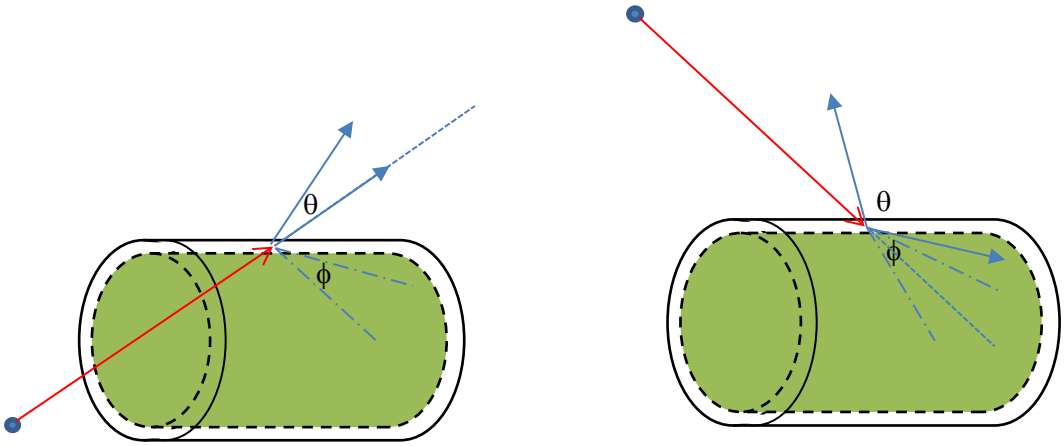

(a) (b)

Figure 4-7. Schematics showing the incoming photon directions (open arrow ⟶), ranges of scattered photon angle, θ (arrow ⟶) and ranges of recoil electron angle, ϕ (dashed-dotted lines – · – · –). The ranges of angles of interest in (a) the floor arrangement were $0 < \theta < 20$ and $50 < \phi < 90$ and (b) the holder arrangement were $50 < \theta < 130$ and $-20 < \phi < 20$. θ is measured counterclockwise from the dotted line ------ (representing the initial photon's direction) and ϕ clockwise.

Finally, the differential cross-sections at multiple discrete angles were calculated using Eq. 4-5 and normalized over the sum of differential cross-sections for θ from 0° to 180° to get the relative scattering probabilities as plotted in Fig. 4-8. P_{scatt} values in Eqs. 4-3 and 4-4 are the sum of relative probabilities over the corresponding θ range for each floor and holder arrangements.

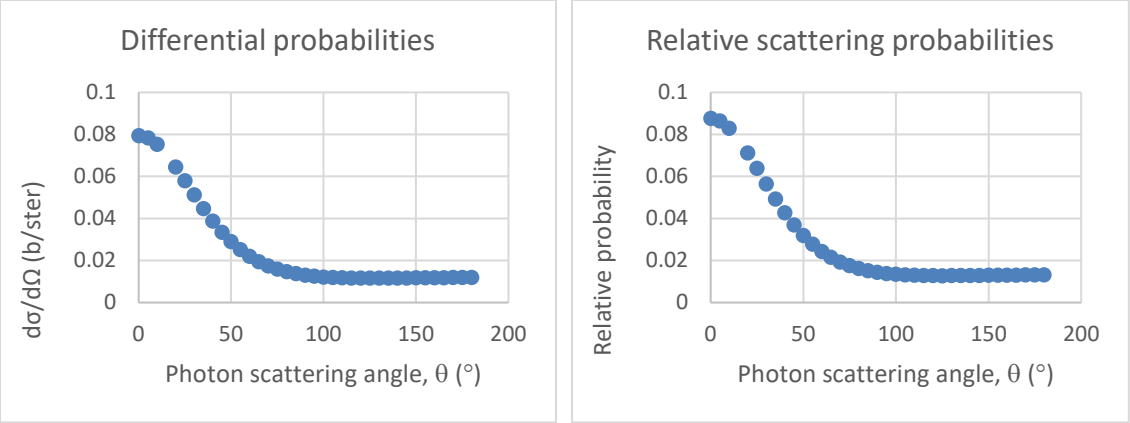

Figure 4-8. Plots of differential cross-sections and relative scattering probabilities for different θ values.

Table 4-1. The approximated parameters for floor and holder arrangements.

Parameters	Floor arrangement	Holder arrangement
Linear attenuation coefficient in neon, μ_{Ne} (cm^{-1})	0.00006463	
Linear attenuation coefficient in aluminum, μ_{Al} (cm^{-1})	0.1999	
Average distance traveled in Ne, $\tilde{t}_{Ne}$ (cm)	4.4	1.27
Mean path in Al, $\tilde{t}_{Al}$ (cm)	0.38995	0.39149
Solid angle, Ω	3.779	0.05815
Probability of scattering into gas volume, P_{scatt}	0.0821	0.5295

It is worth reiterating that, depending on the assumptions made, the analytical calculations give a lower or upper bound of the estimated counts. In this case, it was expected that the values obtained from Eqs. 4-3 and 4-4 would give the upper bound of the estimated counts due to the assumptions of single photon energy and the constant average distance traveled by photons in detector materials. In reality, photons interact in the detector at various energies lower than 662 keV and the distance traveled in the detector's materials varies according to the various photon energies. This means lower N_{sf}

and N_{sh}, hence the expected counts calculated using the outlined steps above serve as an upper bound of the expected counts. Furthermore, the efficiency of the counting system is not included because of the difference in individual detector's efficiency.

4.2.2. MCNP simulations

The detector and source arrangements were modeled in the MCNP simulations as shown in Fig. 4-1 and Fig. 4-2. The Ludlum 44-7 GM simulation has an active length of 13.2 cm with an aluminum casing thickness of 0.1556 cm. The radius of the neon gas volume was 1.905 cm [15]. The materials in the MCNP model are defined based on those listed in the Compendium of Material Composition Data for Radiation Transport Modeling [16]. The concrete floor is modeled as regular concrete (material 99) [16]. The gas in the GM tube was modeled as neon at normal temperature and pressure (material 203) (NTP) [16]. The air surrounding the arrangement is modeled as dry air (near sea level) without argon because the atom fraction is negligible (0.47%) (material 4) [16] and the metal casing of the GM tube is modeled as aluminum alloy 6061 (material 13) [16], which is the most commonly used aluminum alloy.

$$\text{Photon emission rate}, \gamma \left[\frac{photons}{s}\right] = 1.48 \times 10^7 \left[\frac{decay}{s}\right] \times 0.85 \left[\frac{photons}{decay}\right] \qquad (4-8)$$

Two different tallies are included in the MCNP input file. The first was the cell flux tally (F4) which gives the number of photons per area per simulated photon in the units of photons cm^{-2}, by using the formulation of average track length per unit volume of the cell. The second was the *F4 tally which produces energy cell flux per simulated

photon with units of MeV cm^{-2}. These tallies are employed for the active neon gas volume. The expected radiation counts estimated using each of these tallies are proposed to simulate the use of GM detectors for gamma radiation detection. Each type of tally was consistently multiplied with the photon emission rate of ^{137}Cs, which was 1.258×10^7 photons s^{-1} as calculated using Eq. 4-8. The photon transport simulations were performed using MCNP without any variance reduction techniques and the number of simulated particles were 2×10^7 photons.

5.2.2.1. Expected gamma radiation counts using F4 tally

For this simulation, the F4 tally in MCNP gives the average flux in a cell with the unit of photons cm^{-2} per simulated photon [17]. Within the MCNP deck, the F4 tally was modified using energy dependent dose response multipliers (DE and DF in the MCNP input file) [17] and an overall tally multiplier (FM in the MCNP input file). Two simulations were performed for the floor arrangement using two sets of dose response multipliers (1977 ANSI/ANS and ICRP-21). The dose response multiplier set that resulted in expected true counts closer to the measured true counts was selected to be used in this method.

The FM input (tally multiplier to scale up to the source strength) to MCNP considered the GM detector sensitivity and the conversion factor for rem hr^{-1} unit to mR hr^{-1} in tissue in addition to the photon emission rate shown in Eq. 4-8. The F4 tally given with the photon emission rate, DE and DF inputs have units of rem hr^{-1}. The conversion factor in units of photons $min^{-1}hr\ rem^{-1}$ multiplied by the photon emission rate for the FM

input is obtained using Eq. 4-10. The results of the F4 tally multiplied by the FM input value are in units of min^{-1}.

Table 4-2. The calculated GM sensitivity in the floor arrangement.

Detector	GM sensitivity (cpm hr mR^{-1})
1	2.74E+03
2	3.29E+03
3	3.21E+03
4	2.84E+03
5	3.06E+03
6	3.02E+03

The detector sensitivity value was given in the Ludlum 44-7 manual as cpm $(mR\ hr^{-1})^{-1}$ [15]. It was verified in the calibration report that the calibration geometry was different than the floor arrangement geometry. Therefore, this sensitivity value was only applied to the holder arrangement which has a similar geometry to the calibration geometry. For the floor arrangement, sensitivity for each detector is calculated by dividing the measured counts in one minute by the calculated exposure rate using Eq. 4-9 at a third of the detector's length. For detectors 1 and 4, the distance between the source and a third of the detector's length, r is 5.4 cm, while for the rest of the detector, r is 8.5 cm. The first term in Eq. 4-9 accounts for the w-value for neon, which is 36.2 eV per ion pair [18]. The GM sensitivity values calculated are shown in Table 4-2.

$$\dot{X}_c \left[\frac{mR}{hr}\right] =$$

$$\frac{4.914 \times 10^{-3}}{r^2}\left[\frac{mR\ g\ s}{MeV\ hr\ cm^2}\right] \times \gamma \left[\frac{photons}{s}\right] \times \text{Energy}\,[MeV] \times \left(\frac{\mu_{en}}{\rho}\right)_{Ne}\left[\frac{cm^2}{g}\right] \quad (4-9)$$

FM for F4 =

$$\gamma \left[\frac{photons}{s}\right] \times 1\left[\frac{rad}{rem}\right] \times 1000\left[\frac{mR}{R}\right] \times \frac{\left(\mu_{en}/\rho\right)_{air}}{0.877\left(\mu_{en}/\rho\right)_{tissue}}\left[\frac{R}{rad}\right] \times GM\ sensitivity\left[\frac{cpm}{mR/hr}\right] \quad (4-10)$$

4.2.2.2. Expected counts using *F4 tally

For the simulation in this research the *F4 tally gave the average energy flux in a cell with units of MeV cm^{-2} per simulated photon [17]. To reflect the expected counts using the *F4 tally, the FM input in MCNP includes the GM detector's sensitivity and an estimate of the exposure rate in addition to the photon emission rate as shown by Eq. 4-8. The mass linear attenuation of neon at 662 keV is assumed for exposure rate determination using Eq. 4-12 and this value is determined by linear interpolation to be 0.027594 cm^2g^{-1}. The conversion of exposure rate unit from C g^{-1} s^{-1} in Eq. 4-11 to mR hr^{-1} is shown by Eq. 4-12. Together with the FM input as calculated using Eq. 4-13, the *F4 tally given in the output file would be in units of min^{-1}. Similar to the F4 method, the GM sensitivity from the product manual is only applied to the holder measurement. The same values listed in Table 4-2 are used in Eq. 4-13 for the floor arrangement.

$$\dot{X}\left[\frac{C}{gs}\right] = {}^{*}\text{F4}\left[\frac{MeV}{cm^2 s}\right] \times \left(\frac{\mu_{en}}{\rho}\right)_{Ne}\left[\frac{cm^2}{g}\right] \times \frac{e}{W}\left[\frac{C}{MeV}\right] \quad (4-11)$$

$$\dot{X}\left[\frac{mR}{hr}\right] =$$

$$^{*}\text{F4}\ \left[\frac{MeV}{cm^2 s}\right] \times \left(\frac{\mu_{en}}{\rho}\right)_{Ne}\left[\frac{cm^2}{g}\right] \times \frac{1.602 \times 10^{-19}}{36.2 \times 10^{-6}}\left[\frac{C}{MeV}\right]$$

$$\times 3600\left[\frac{s}{hr}\right] \times 1000\left[\frac{g}{kg}\right]\frac{1}{2.58 \times 10^{-7}}\left[\frac{mR}{C/kg}\right] \qquad (4-12)$$

$$\text{FM for } ^{*}\text{F4} = \gamma\left[\frac{photons}{s}\right] \times GM\ sensitivity\left[\frac{cpm}{mR/hr}\right] \times \dot{X}\left[\frac{mR}{hr}\right] \qquad (4-13)$$

4.2.3. Validation measurements

The previous sections have shown how the expected counts from the GM detectors are analytically solved to get an estimate of the range of counts obtained from the simulation and measurements. The MCNP simulation model and two methods of transforming the MCNP output of cell average gamma radiation flux (F4 tally) and energy flux (*F4 tally) into expected radiation counts are also thoroughly explained. This section describes how the experimental counts are processed to account for detector's dead time and the procedure to select the tally-processing method to be employed in this research.

Experiments are conducted using six Ludlum 44-7 GM detectors and six Ludlum 2200 scaler ratemeters. The picture on the right in Fig. 4-1 shows the detector arrangement. Each GM detector is paired with a ratemeter using a type C cable connector. The GM detectors are arranged as close as possible to the simulated arrangements. Five consecutive 1-minute measurements are taken for each of the floor and holder arrangements. The counts are averaged and the standard deviation of the data is taken as the uncertainty.

Background counts are neglected because the measured counts in this geometry are orders of magnitude higher than the background counts.

For the floor arrangement, the high gamma radiation flux from the high-activity (14.8-MBq) ^{137}Cs source required the detector's dead time, τ, to be accounted for [19]. Each GM detector is assumed to have a τ of 200 μs based on Ludlum's 44-7 manual [15]. The true count rates, n of the measurements were determined by dividing the averaged measured count rate, m by $(1 - m\tau)$. The n values with the respective propagated uncertainties are then compared with the expected counts calculated using the simulated fluxes from MCNP simulations for both the F4 and *F4 tallies.

There are two requirements for one of the methods to be selected. The first one is the proposed method must have a simulated-to-measured-counts ratio, r above 0.8 as this represents an agreement within 20% between the simulated and measured counts. The second requirement is that the measured counts uncertainties must be less than the absolute difference between the simulated and experimental counts [20]. The latter requirement is designated as a validation metric in Section 4.2.5.

4.2.4. Simulations and experimental measurements of the initial collimator configurations

After a tally-processing method is selected, a validation is performed for two collimator configurations of the proposed system. As explained in the Introduction section, the tested collimator configurations consist of either an all-empty or an all-full collimator. MCNP simulations were performed with all PVC pipes that make the collimator filled with water (all-full) and filled with air (all-empty). The expected counts

obtained using the selected MCNP method are multiplied by 15 minutes to get the counts in the same time period as that in the measurement. For the experimental measurements, the six GM detectors placed underneath the tank in the same arrangement as in the MCNP simulation model are set for a 15-minute measurement for each source arrangement. Due to the bigger complexity in the geometry of these validation settings, the measurement time was set as 15 minutes to ensure enough data was obtained for statistical analysis, instead of one minute for the simple-geometry measurements described in Section 4.2.3.

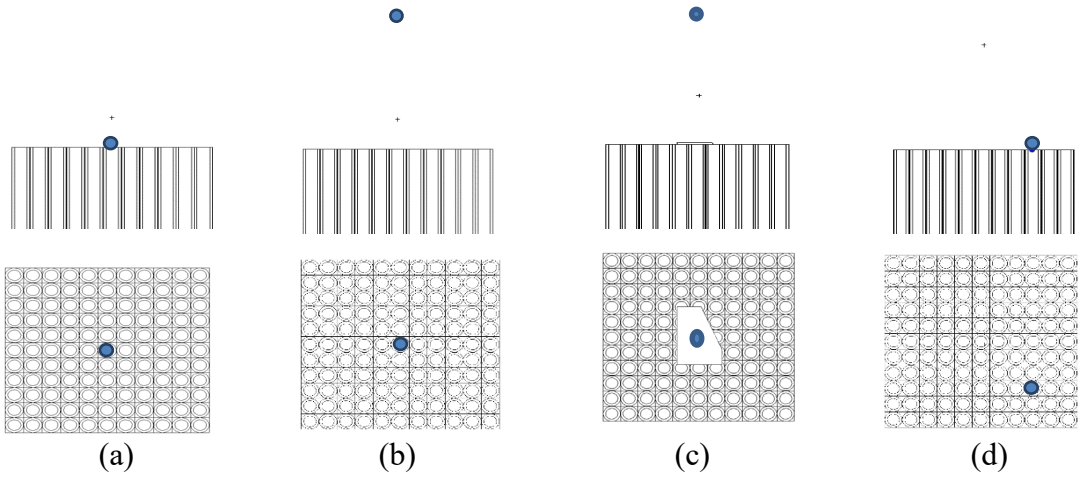

Figure 4-9. The gamma source position for each case and each configuration: (a) center, (b) above, (c) above metal and (d) corner.

Simulations and measurements are done for four ^{137}Cs gamma source positions corresponding to four cases. These source positions are shown in Fig. 4-9. In each sub-figure, the top image shows the side view and the bottom image shows the top view of the 11-by-11 PVC collimator. In (b) and (c), the gamma source position is 27.94 cm above the collimator. In (c), an irregular-shaped object in the middle represents an aluminum alloy piece placed on top of the collimator at the center. This is done to observe the effect

of a lightly shielded source on the detection counts. Furthermore, the effect of the shielding on the image reconstruction will be investigated in future validation experiments.

In addition to eight measurements for both configurations (four cases in each configuration), background counts are also needed for each measurement. A total of 16 measurements are made for the all-full and all-empty pipe configurations. Net counts from each detector are determined by subtracting the corresponding background counts from the gross counts obtained in each case. Errors are propagated for the subtraction, addition, and division operations performed on the data.

Comparisons of the simulated and measured gamma radiation counts are made between individual detectors and for the whole detector group as a detection system. The net counts from individual detector from simulation and experiment for each case are compared (Figs. 4-10 and 4-11). Analyzing all six detectors as a detection system, the summed net counts in the experiment, and the total simulated counts are compared including their respective error bars. Any discrepancies between the simulation and experiment results are discussed in detail later.

4.2.5. Validation metrics

In addition to the statistical analysis of the simulation and experimental comparisons, a validation metric as expressed in Eq. 4-14 is applied in analyzing the results [20]. The total propagated measurement uncertainties are compared to the discrepancy between the simulated counts and the measured counts. It should be kept in mind that the focus in achieving Eq. 4-14 was to minimize the experimental uncertainties instead of maximizing the gap between simulation and experimental results. A “good”

model has a minimal gap between simulation and experimental data, while having measurement uncertainties less than the difference between these results. Ultimately, if the discrepancy between simulation and experimental results are reduced, this should be accompanied by the reduction in experimental uncertainties in order for the model to be considered as accurate. Otherwise, this would indicate that the model was inadequate and needed to be redefined or different instruments are needed to perform the measurements.

The validation result is determined "acceptable" if Eq. 4-14 was met, or "risky" if Eq. 4-14 is not met. A "risky" validation result means that the current model is risky for practical application because of the discrepancy between the model data and experimental data being larger than the measurement uncertainty. This might indicate that a modification for the way the expected counts are obtained through the model is needed, or different instruments are needed to perform the measurements if one chose to utilize a method with a "risky" metric result.

$$\text{Experimental uncertainty, } \sigma_u < |\text{simulation data} - \text{experimental data} \qquad (4-14)$$

For the all-full configuration, it is difficult to evaluate the results based on Eq. 4-14 as it is expected that the measurement uncertainties are large compared to the measured net counts. This is due to the uncertainty propagation and the low net measured counts for this particular configuration. Another validation metric is defined specifically for the all-full configuration to validate whether the proposed design worked as intended.

$$N_{th} = 4.65\sigma_{BG} + 2.71 \qquad (4-15)$$

The all-full configuration should give minimal counts that would be indistinguishable from background counts. The Currie equation is used to define the threshold, N_{th} that would indicate a false-negative rate of no larger than 5% when the critical level was set to be $2.33\sigma_{BG}$, where $\sigma_{BG}$was the background uncertainty [21]. This threshold was defined as Eq. 4-15. The proposed system is said to be behaving as designed if the net measured counts are less than the N_{th} value, indicating that no radiation source is detected.

4.3. Results and Discussion

4.3.1. F4 and *F4 methods comparison

The plots of the expected true counts using the 1977 ANSI/ANS and ICRP-21 dose response multipliers and the measured true counts are shown in Fig. 4-10. The error bars on the simulated data points are three orders of magnitude smaller than the estimator values, resulting in their error bars to be obscured in the plots. The F4 estimator results using the 1977 ANSI/ANS dose response multipliers are within 2σ of the measured true counts, while the F4 estimator results using the ICRP-21 dose response multipliers are not within 2σ of the measured true counts.

These discrepancies were due to the known fact that there are more than 20% differences between the dose conversion factors for photons below 0.7 MeV [17]. The maximum discrepancy is by a factor of 2.3 and this occurs at 0.06-MeV photon energy [17], and this is reflected in Fig. 4-10 as the expected true counts across all photon energies using ANSI/ANS dose conversion factors are shown to be 1.2 times those of ICRP-21

dose conversion factors. The 1977 ANSI/ANS dose conversion factors were selected to be used in the F4 method.

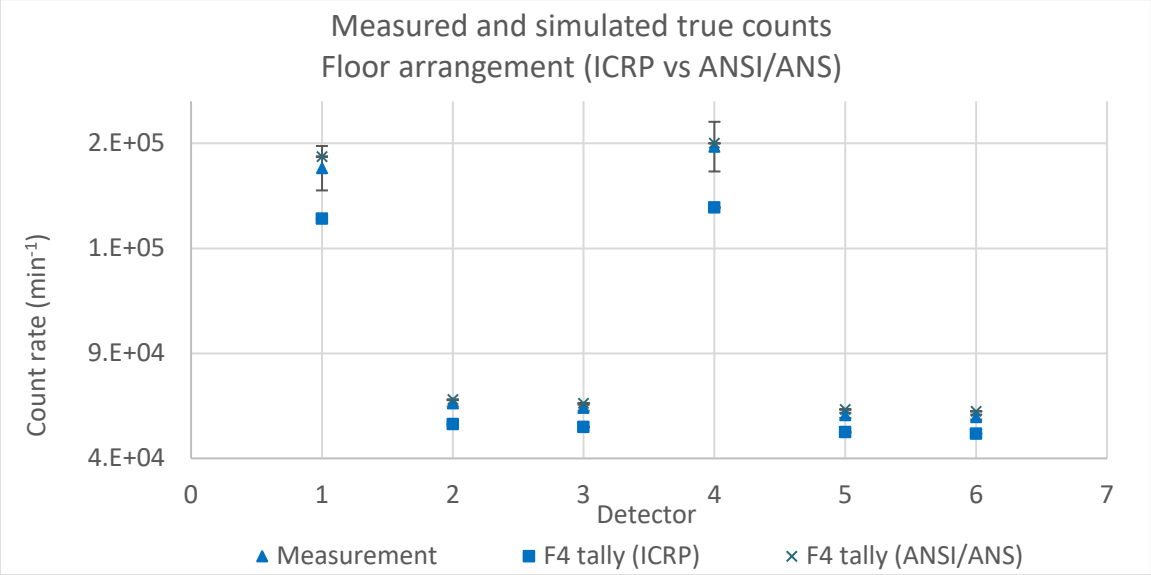

Figure 4-10. The comparison of measured and simulated true counts over a one-minute period for the floor arrangement on a semi-log scale. Error bars of 1σ were included on measurement data points.

Figures 4-11 and 4-12 show the plots of the individual detector's analytical estimate of expected counts for one-minute measurements, MCNP simulation results using the F4 and *F4 tallies, and the experimental measured counts. The analytical solutions, which serve as the upper bound of the expected count rates, were 4.24×10^5 counts per minute for the floor arrangement and 9.59×10^3 for the holder arrangement.

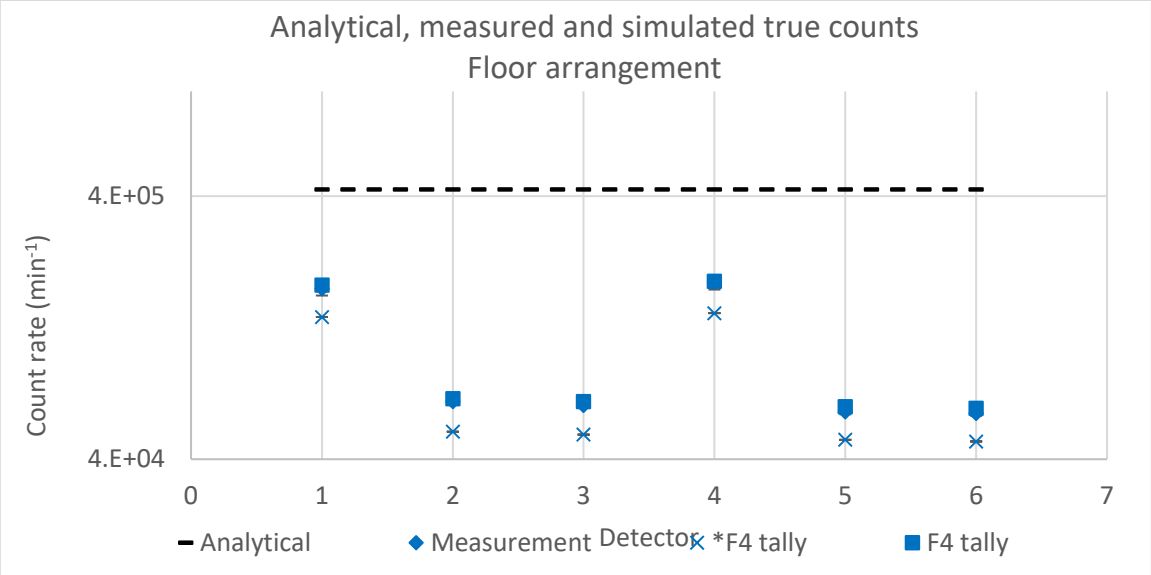

Figure 4-11. The comparison of analytically calculated, measured and simulated true counts over a one-minute period for the floor arrangement on a semi-log scale. Error bars of 1σ were included on measurement data points.

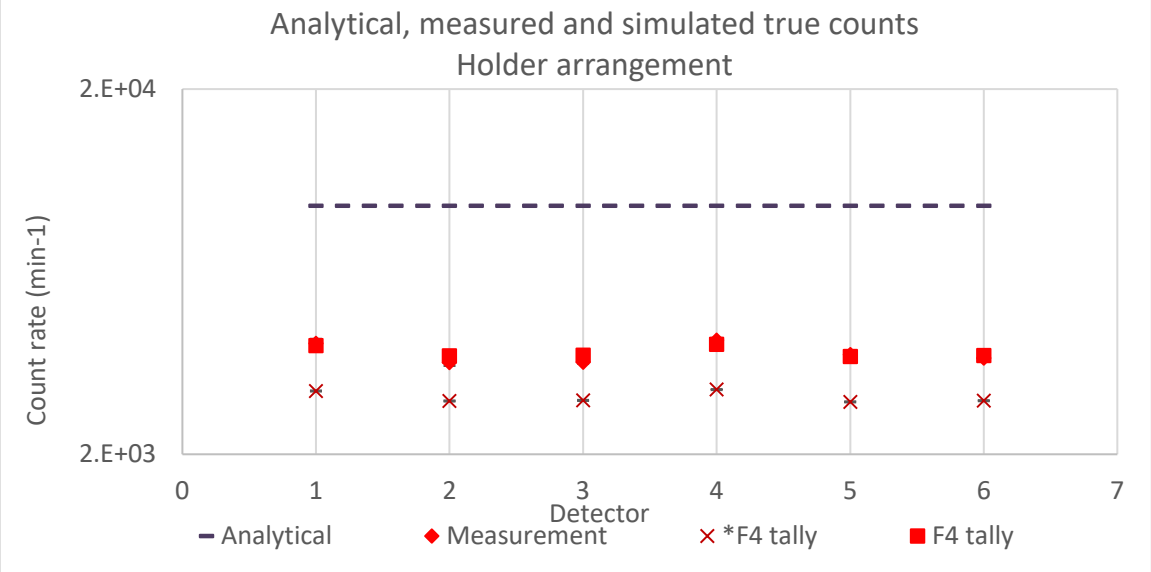

Figure 4-12. The comparison of analytically calculated, measured and simulated true counts over a one-minute period for the holder arrangement on a semi-log scale. Error bars of 1σ were included on measurement data points.

The plots show that the individual simulated counts using both methods have the same trend as the measured counts. Detectors 1 and 4 are placed in line of each other while the other four are placed diagonally on each side of detectors 1 and 4. Together, they make a radial arrangement as shown in Fig. 4-1. Detectors 1 and 4 are expected to give the highest counts for both the floor and holder measurements. This is indeed observed in both simulated and measured counts for both arrangements.

Table 4-3 displays the simulated-to-measured-counts ratio, r values for each method and shows that the experiment and simulated counts agreed within 20% of each other for the F4 method. However, for the *F4 method, the gap between simulation and experimental results is larger and the r values show that simulated and measured counts agreed within 30% of each other. The method using the *F4 tally underestimated the expected counts because the linear attenuation coefficient is assumed to be that of the 662 keV energy. Consequently, the estimated counts using Eq. 4-12 would underestimate the actual measurements and be lower than those determined using the F4 tally formulation.

Using Eq. 4-14, the F4 method showed that it met the validation metric inequality as the uncertainties of the measurements are less than the absolute difference between the simulated and measured counts. Table 4-4 summarizes this assessment for both F4 and *F4 expected gamma radiation count rate estimation methods.

Table 4-3. The simulated-to-measured-counts ratio, r for each method of estimating counts from GM detectors.

F4 tally						
Detector	Floor			Holder		
	Experiment counts	Simulated counts	r value	Experiment counts	Simulated counts	r value
1	1.78E+05	1.84E+05	1.03	4.03E+03	3.96E+03	0.98
2	6.62E+04	6.80E+04	1.03	3.57E+03	3.72E+03	1.04
3	6.41E+04	6.63E+04	1.03	3.57E+03	3.74E+03	1.05
4	1.88E+05	1.90E+05	1.01	4.11E+03	4.00E+03	0.97
5	6.05E+04	6.33E+04	1.05	3.75E+03	3.70E+03	0.99
6	5.97E+04	6.24E+04	1.05	3.67E+03	3.73E+03	1.02
*F4 tally						
Detector	Floor			Holder		
	Experiment counts	Simulated counts	r value	Experiment counts	Simulated counts	r value
1	1.78E+05	1.39E+05	0.78	4.03E+03	2.98E+03	0.74
2	6.62E+04	5.09E+04	0.77	3.57E+03	2.80E+03	0.78
3	6.41E+04	4.96E+04	0.77	3.57E+03	2.81E+03	0.79
4	1.88E+05	1.44E+05	0.76	4.11E+03	3.01E+03	0.73
5	6.05E+04	4.74E+04	0.78	3.75E+03	2.78E+03	0.74
6	5.97E+04	4.67E+04	0.78	3.67E+03	2.80E+03	0.76

The F4 tally method is selected to be the standard method to validate the proposed system model because the requirements stated in Section 4.2.3 are met. The simulated-to-measured-counts ratio, r values for the F4 method are all above 0.9 or below 1.1 for both floor and holder arrangements. This represents deviation of less than 10% from the

experimental counts. Additionally, the validation metric results are all “acceptable” for the F4 method in both arrangements. Therefore, the F4 method is applied in the validation tests for the two basic collimator configurations of the proposed system.

Table 4-4. The summary of the validation according to the defined validation metric in Eq. 3-14 for both F4 and *F4 methods in the floor and holder arrangements.

Method	Summed measured counts	Uncertainties of summed measured counts	Summed simulated counts	Validation result
F4 (floor)	6.17E+05	1.61E+04	6.34E+05	Acceptable
F4 (holder)	2.27E+04	1.60E+02	2.29E+04	Acceptable
*F4 (floor)	6.17E+05	1.61E+04	4.77E+05	Acceptable
*F4 (holder)	2.27E+04	1.60E+02	1.72E+04	Acceptable

4.3.2. Comparison between simulated and measured counts for the validation tests

The validation tests for the proposed system are divided into two comparisons. First one is the comparison between individual detectors and the other is the comparison of the summed counts from all six detectors for each case. The summed net counts from experimental measurements are compared to those of simulation because the sums of the net counts from all detectors are used in reconstructing the images of the gamma source. The individual detector comparison is also presented as it would be beneficial in demonstrating how variations in actual measurements could be compared to the simulated results.

4.3.2.1. Individual detector comparisons

Figure 4-13 shows the plots of the expected and measured net counts in 15-minute measurements of the four cases for the all-full configuration. Two main observations in this figure are the variations between each detector counts and zero net count given by some of the detectors. There are significant variations between each detector because of the different responses and sensitivities in these detectors. Unlike in actual measurements, the detectors modeled in MCNP behave similarly and represent a near-perfect detector. This is why simulated counts appear to be more consistent across all detectors. The actual detectors might have slightly different gas pressure, gas composition, and efficiency, resulting in them responding differently. Due to this, some detectors consistently gave lower counts, and some higher counts than others. Detectors 3, 4 and 6 are observed to be less sensitive in this geometry as they either gave zero net counts or lower counts than the other detectors. Detectors 1, 2, and 5 are the more sensitive ones in this geometry as they typically gave higher net counts compared to other detectors.

Certain detectors gave negative net counts and these were reported as zero net count in the plots. A zero net count on the plot means that the particular detector was not able to distinguish the counts contributed by the ^{137}Cs source from the background counts. While these detectors are reported to have zero net count, uncertainties associated with the measurements are still assigned to the zero net count data points. The uncertainty on each measured data point is between 26 to 34 counts. Therefore, all of these points are statistically the same between each detector. The measurement data points are also

statistically the same as the expected counts from MCNP simulations, except for detector 6 in the above case and detector 4 in the corner case.

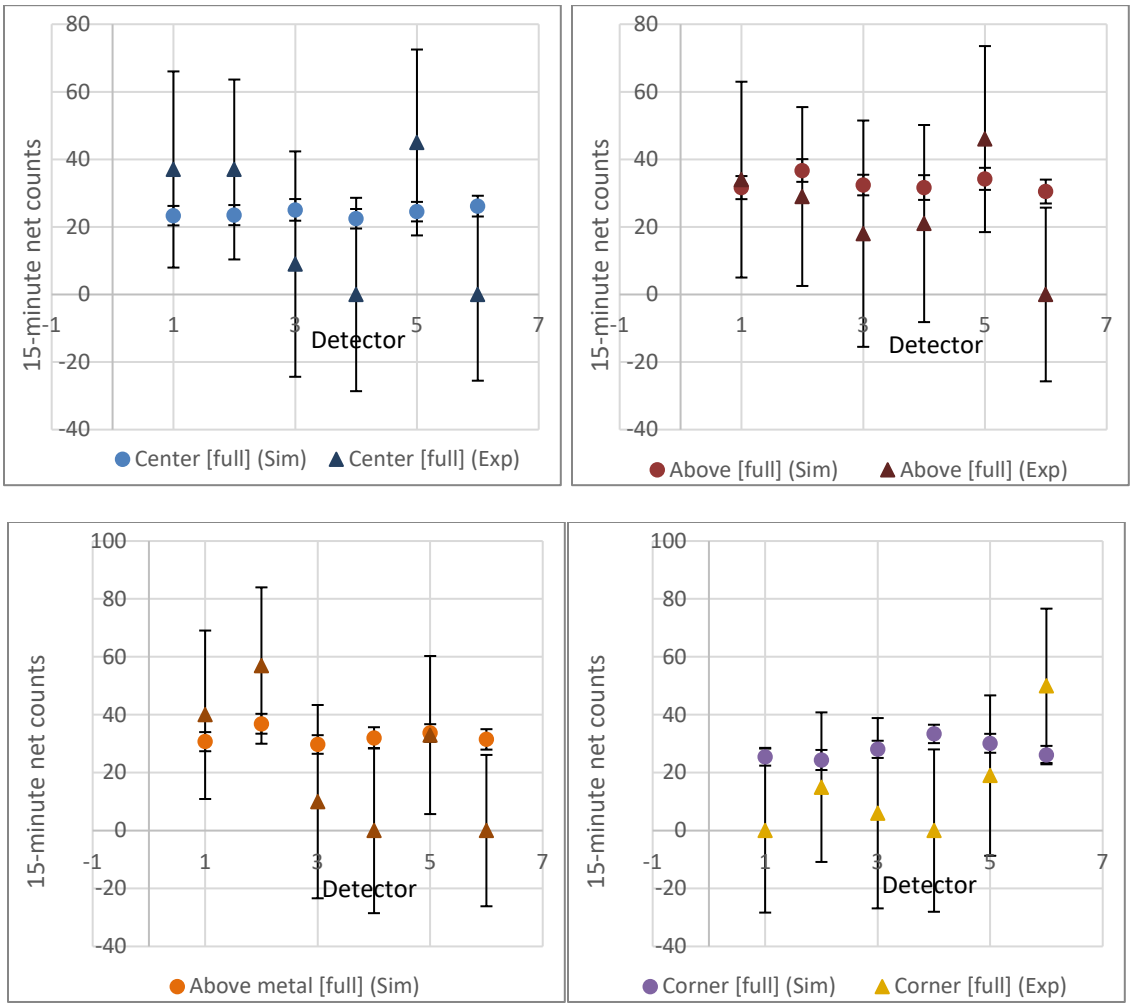

Figure 4-13. The individual measured net counts from each of the six detectors in each case for the all-full configuration compared to the simulated net counts. Propagated uncertainties of 1σ were included on measurement and simulated data points. Round markers represent experimental results.

It is also worth mentioning that since the all-full configuration was designed to minimize counts from the detectors, the measurement results would change if these measurements were repeated. Different detectors might give zero net count readings instead of those shown in the plots here. This is because of the random fluctuations in

radioactive decays and with these small net counts calculated over two different 15-minute measurement intervals, it is likely that different set of detectors would not detect the gamma source, if the same measurements were made again.

Figure 4-14 shows the plots of the expected and measured net counts in 15-minute measurements of the four cases for the all-empty configuration. Two main observations in these plots are that the measured net counts are always lower than the simulated counts and the detector that was directly below the source position in the corner case gave significantly higher counts than other detectors.

As observed in the all-full configuration, the simulated counts are higher than the measured counts due to some loss of counts because of the higher photon scattering in the experimental setting. This is also evident in the all-empty configuration plots, where the simulated counts are shown to be higher than the measured counts. However, the uncertainty on each measured data point is between 27 to 34 counts. Therefore, all of these data points are not within 2σ of each other in the center case. Five out of six data points are within 2σ of each other in the above case, three out of six in the above metal case and only one out of six in the corner case. The differences are by a factor of less than 4 for the detectors in all cases, except for detector 3 in the center case (4.41), detector 6 in the above case (4.22) and detector 1 in the corner case (4.11).

However, a more important indicator would be that the system is behaving as intended and expected. It is clear from Fig. 4-14 that detectors 1 and 4 gave higher net counts than the other detectors in the center case and that detector 5 gave the highest net counts in the corner case. The counts from the detectors in the above and above metal

cases are on average statistically lower than those of the center and corner cases because of the increased source-to-detectors distance. These results are as expected for the geometry of the all-empty configuration. Again, the analysis in this section is intended to show that statistically significant difference will be expected between simulated and measured counts for different detectors.

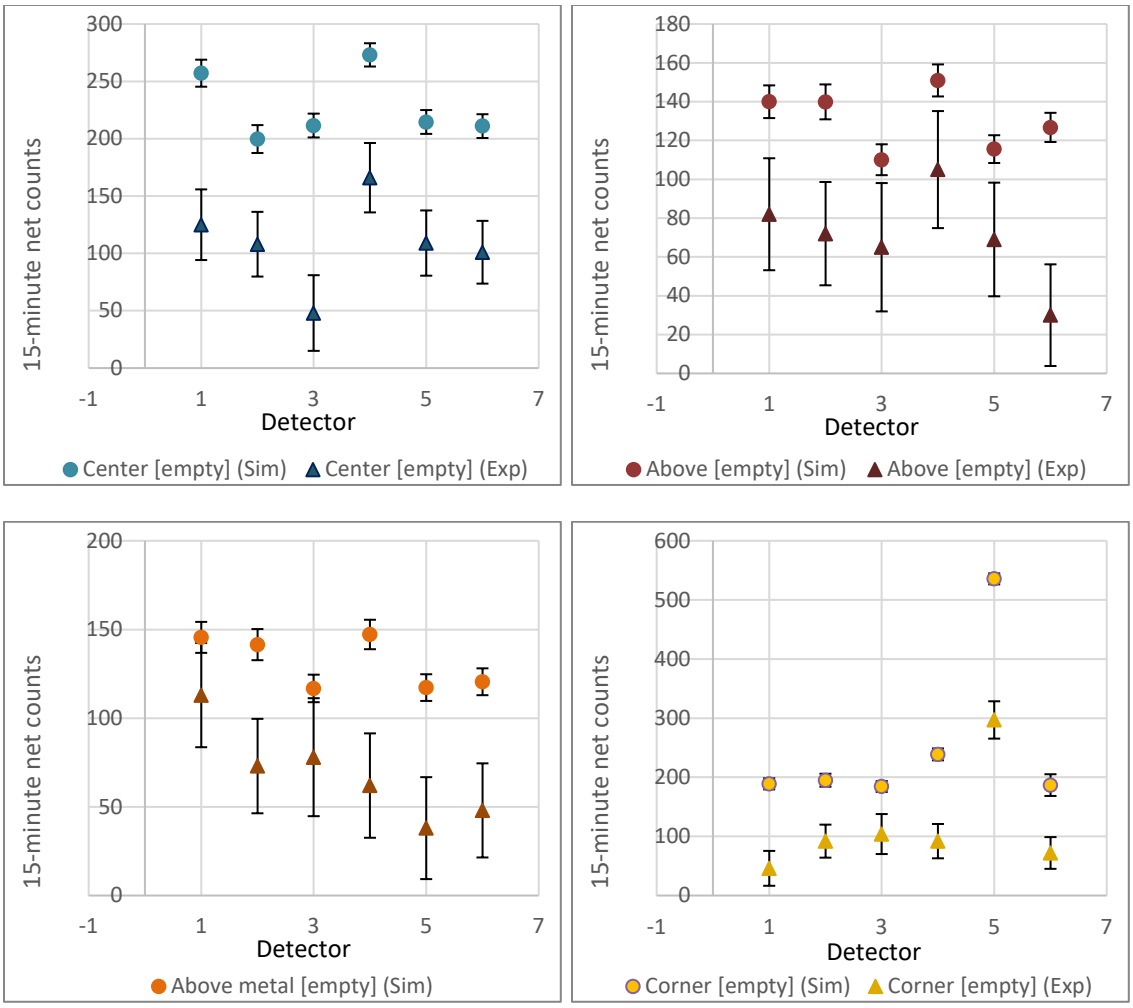

Figure 4-14. The individual measured net counts from each of the six detectors in each case for the all-empty configuration compared to the simulated counts. Propagated uncertainties of 1σ were included on measurement data points. Round markers represent expected counts from F4 method and triangle markers represent experimental results.

4.3.2.2. Summed net counts comparisons

Figure 4-15 shows plots of the summed expected counts in a 15-minute measurement for all-full and all-empty configurations, as well as the summed measured counts. The error bars shown on the plots represent uncertainties of 1σ. These error bars are large because the errors are propagated through the summation of six measured counts. In both configurations, the trends of the simulated and measured counts are similar. Each error bar in both cases has a value between 70 to 73 counts.

The proposed system is designed to have minimal counts when the collimator is completely filled with water. Consequently, the summed net counts for all cases for the all-full collimator configuration are expected to be the same. For the all-full configuration, counts for all cases are statistically the same, which is as expected. For the all-empty configuration, the summed experimental net counts for gamma source positions on top of the collimator are statistically larger than those of higher source positions. This can also be seen with the summed simulated counts. However, there is a large difference between the summed simulated counts and summed measured net counts in the center and the corner cases. This is evident from the all-empty plot where the summed simulated counts are shown to be not within 2σ from the measured summed net counts.

The difference might be due to the loss of counts in the actual measurements because of higher photon scattering resulting from the uneven arrangement of collimator. The PVC pipes are not perfectly assembled with straight edges as simulated in the MCNP model. Furthermore, some of the PVC pipes might not be perfectly straight or placed upright. These all could contribute the to the photons being scattered away from the

detectors underneath the tank and reducing the number of counts detected. This factor seemed to be less significant when the ^{137}Cs source was positioned 27.94 cm above the collimator as apparent in the all-empty plot. The summed simulated counts agree within 3σ of the summed measured net counts for above and above metal cases. The additional 27.94 cm distance resulted in less photons arriving at the collimator as well as more photons being scattered away from the detectors, which led to a better agreement between the summed simulated and measured net counts for the above and above metal cases.

In addition to the differences in the overall geometry of the system, discrepancies between simulated and measured results were also expected because of the way the GM tube was modeled. As mentioned in Section 4.1.1., the gas in the GM tube was modeled as neon because the GM tube manual does not specify the exact type of halogen used as quenching gas in the detector. Including quench gas in the simulation would result in lower counts as the fluxes are expected to decrease with the presence of quench gas that preferentially absorbs secondary photons.

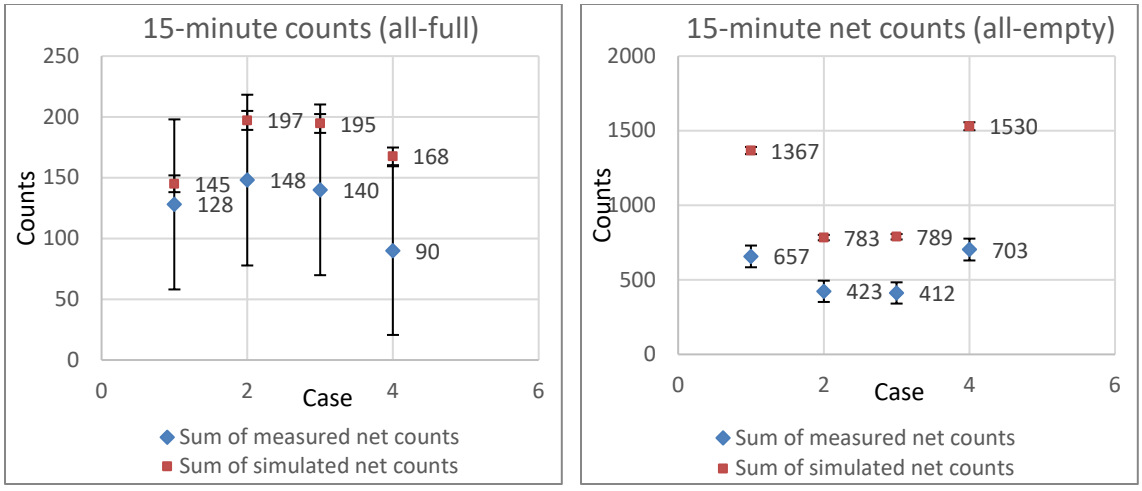

Figure 4-15. Plots of 15-minute summed net counts for all-full and all-empty configurations. Propagated uncertainties of 1σ were included on measurement data columns.

Despite the stark discrepancies in the all-empty configuration for center and corner source positions, the summed measured net counts are lower by a factor of 2.08 and 2.18 respectively. The summed measured net counts are lower than the summed simulated counts by a factor of 1.85 and 1.91 for the above and above metal cases respectively. These factors represented 46% to 54% loss in the simulated counts across all cases due to the imperfections in the experimental setting when the simulation model is translated to a physical product. Another way of viewing these discrepancies is that compared to the measured counts, a simulation model representing the experimental set up resulted in 185% to 218% additional counts, due to the idealization of the prototype. The idealization of the model included similar behavior of detectors, near-perfect properties of modelled detectors, homogeneity in materials simulated in the model and perfect symmetry or placements of equipment and radiation source.

Using the validation metric defined in Eq. 4-14, Table 4-5 summarizes that the suggested model is "acceptable" for the all-empty configuration cases. However, the validation result was determined "risky" for the all-full configuration cases, except for the corner case, as the total measurement uncertainties exceeded the absolute difference between summed simulated and measured net counts.

Table 4-5. The summary of the validation according to the defined validation metric in Eq. 3-14 for both initial collimator configurations.

Case	Summed measured net counts	Uncertainties of summed measured net counts	Summed simulated net counts	Validation result
Center (all-empty)	657	73	1367	Acceptable
Above (all-empty)	423	71	783	Acceptable
Above metal (all-empty)	412	71	789	Acceptable
Corner (all-empty)	703	73	1530	Acceptable
Center (all-full)	128	70	145	Risky
Above (all-full)	148	70	197	Risky
Above metal (all-full)	140	70	195	Risky
Corner (all-full)	90	69	168	Acceptable

Despite this violation of the Eq. 4-14 requirement, the suggested model might still be considered as acceptable because it would be difficult to reduce the measurement uncertainties for this particular configuration. The all-full configuration was designed in such a way that would result in minimal counts that would be indistinguishable from background. Furthermore, it was expected that the error bars would be as large as the net

counts because of the low net counts and the propagated uncertainties from using six separate detectors.

What is important to validate for the all-full configuration was that the system should determine that there was no ^{137}Cs source detected when all the collimator channels are filled with water. Table 4-6 summarizes the source detection validation metric as defined in Eq. 4-15 for the all-full configuration. It was concluded that the system behaved as expected and as required for the all-full configuration as it was proven that the counts were indistinguishable from the background counts when the collimator was completely filled with water.

Table 4-6. The summary of the validation according to the defined validation metric in Eq. 4-15 (source detection metric) for the all-full configuration.

All-full case	Net summed measured counts	Threshold net counts, N_{Th}	^{137}Cs source detected?
Center	128	328	No
Above	148	329	No
Above metal	140	329	No
Corner	90	325	No

In summary, it has been demonstrated that the MCNP simulation model of the proposed system utilizing the F4 method is validated for the two collimator configurations. In the case of the all-full configuration, both simulated and measured net counts agreed within 2σ uncertainties of the measurements for all the source positions. The summed measured net counts were less than the simulated counts by a factor of less than 2.5 for both configurations. The validation metric requirement was met for the all-empty configuration. While the all-full configuration results did not meet the validation

metric, the source detection metric was met, proving that the proposed system behaved as intended. These results show that the MCNP simulation model is validated for both all-empty and all-full configurations of the proposed system.

4.4. Conclusion

This paper has demonstrated two ways of estimating counts from GM detectors using MCNP simulations. The counts estimate using F4 tally method is found to resemble the measured counts more closely compared to the *F4 method. The F4 tally results are all less than 20% different from the measured counts in both floor and holder arrangements. In addition, the validation metric for the F4 method came out as "acceptable" for both arrangements.

The F4 tally method is therefore chosen to be used for the validation of the proposed gamma source imaging system model. Comparisons between the individual detector's simulated and measured counts are shown to be statistically the same in the all-full configuration but not in the all-empty configuration. However, in the all-empty configuration case, the trends of the count readings are the same in both simulation and experiment, and as expected in all cases. The summed measured net counts are less than the summed simulated counts by a factor of less than two for all four source positions in the all-empty configuration. Discrepancies are attributed to the imperfect assembly of the PVC collimator, as well as the difference in responses and sensitivities of the detectors used in the experiment.

The all-full configuration comparison showed statistical agreement between the simulated and measured net counts. The validation metric result is "acceptable" for the

all-empty configuration but not for the all-full configuration. However, the source detection metric is fulfilled for the all-full configuration showing that the system worked as intended. From the results and discussion presented, the MCNP simulation model is deemed as validated for the two collimator configurations of the proposed system. Based on the presented results, the modeling of GM detectors using the proposed F4 method has been shown to agree with the measurements, especially in terms of the behavior trends. It is therefore suggested that the F4 method to be utilized by researchers or students who are working with GM detectors simulations.

4.5. References

[1] T. Goorley *et al.*, "Initial MCNP6 Release Overview," *Nuclear Technology*, vol. 180, no. 3, pp. 298–315, Dec. 2012, doi: 10.13182/NT11-135.

[2] O. M. Noor, "Development of Energy Compensated Geiger Muller Detector Based on The T2416A Canberra Co. GM Detector," 2013.

[3] I. Meric, G. A. Johansen, M. B. Holstad, and R. P. Gardner, "Monte Carlo modelling of gamma-ray stopping efficiencies of Geiger–Müller counters," *Nuclear Instruments and Methods in Physics Research Section A: Accelerators, Spectrometers, Detectors and Associated Equipment*, vol. 636, no. 1, pp. 61–66, Apr. 2011, doi: 10.1016/j.nima.2011.01.083.

[4] S. Grujić, I. Đorđević, M. Milošević, and U. Kozmidis-Luburić, "Monte Carlo simulation of GM probe and NaI detector efficiency for surface activity measurements," *Radiation Measurements*, vol. 58, pp. 45–51, Nov. 2013, doi: 10.1016/j.radmeas.2013.08.002.

[5] E. J. Candès, “Compressive sampling,” in *Proceedings of the International Congress of Mathematicians*, Madrid, Spain, 2006, pp. 1433–1452.

[6] R. G. Baraniuk, “Compressive Sensing,” *IEEE Signal Processing Magazine*, vol. 24, no. 4, pp. 118–121, Jul. 2007, doi: 10.1109/MSP.2007.4286571.

[7] E. J. Candes and M. B. Wakin, “An Introduction To Compressive Sampling,” *IEEE Signal Processing Magazine*, vol. 25, no. 2, pp. 21–30, Mar. 2008, doi: 10.1109/MSP.2007.914731.

[8] E. Candes, J. Romberg, and T. Tao, “Stable Signal recovery from Incomplete and Inaccurate Measurements,” *Wiley Periodicals, Inc.*, vol. LIX, pp. 1207–1223, 2006.

[9] D. L. Donoho, “Compressed Sensing,” in *IEEE Transactions on information Theory*, Apr. 2006, vol. 52, pp. 1289–1306. doi: 10.1109/TIT.2006.871582.

[10] Glenn F. Knoll, “Geiger-Mueller Counters,” in *Radiation Detection and Measurement*, 4th ed., Wiley, 2017, p. 218.

[11] N. Dwork *et al.*, “Utilizing the Wavelet Transform’s Structure in Compressed Sensing,” *arXiv:2002.04150 [eess]*, Feb. 2020, Accessed: Dec. 13, 2020. [Online]. Available: http://arxiv.org/abs/2002.04150

[12] V. Britanak, P. C. Yip, and K. R. Rao, “CHAPTER 1 - Discrete Cosine and Sine Transforms,” in *Discrete Cosine and Sine Transforms*, V. Britanak, P. C. Yip, and K. R. Rao, Eds. Oxford: Academic Press, 2007, pp. 1–15. doi: 10.1016/B978-012373624-6/50003-5.

[13] M. Kapralov, A. Velingker, and A. Zandieh, “Dimension-independent Sparse Fourier Transform,” *arXiv:1902.10633 [cs]*, Feb. 2019, Accessed: Dec. 13, 2020. [Online]. Available: http://arxiv.org/abs/1902.10633

[14] N. Anuar, C. Marianno, and R. G. McClarren, “Employing MCNP to optimize experimental design for compressed sensing neutron source imaging,” *Nuclear Instruments and Methods in Physics Research Section A: Accelerators, Spectrometers, Detectors and Associated Equipment*, vol. 954, p. 161446, Feb. 2020, doi: 10.1016/j.nima.2018.10.124.

[15] “Model 44-7 Alpha-Beta-Gamma Detector Manual,” *Ludlum Measurements, Inc.* https://ludlums.com/images/product_manuals/M44-7.pdf (accessed Dec. 13, 2020).

[16] R. M. Jr, C. Gesh, R. Pagh, R. Rucker, and R. W. Iii, “Compendium of Material Composition Data for Radiation Transport Modeling,” Pacific Northwest National Laboratory, Richland, Washington, PIET-43741-TM-963 PNNL-15870 Rev. 1, Mar. 2011.

[17] C. J. Werner (editor), “MCNP® User’s Manual - Code Version 6.2,” Los Alamos National Laboratory, LA-UR-17-29981, Oct. 2017. [Online]. Available: https://mcnp.lanl.gov/pdf_files/la-ur-17-29981.pdf

[18] Glenn F. Knoll, “Proportional Counters,” in *Radiation Detection and Measurement*, 4th ed., Wiley, 2017, p. 176.

[19] Glenn F. Knoll, “Dead Time,” in *Radiation Detection and Measurement*, 4th ed., Wiley, 2017, p. 121.

[20] Semyon G. Rabinovich, “Postulates of the Theory of Measurements,” in *Evaluating Measurement Accuracy: A Practical Approach*, Springer, 2010, pp. 14–15.

[21] Glenn F. Knoll, “Counting Statistics and Error Prediction,” in *Radiation Detection and Measurement*, 4th ed., Wiley, 2017, p. 98.

5. BENCHMARKING OF NNLS APPLICATION TO A PROOF-OF-CONCEPT GAMMA SOURCE IMAGING SYSTEM

5.1. Introduction

This study aims to validate the simulation results of a proof-of-concept system for gamma source imaging with experimental measurements. The proposed system was envisioned to be applied in the nuclear security field, especially for the screening of illicit radioactive materials. The smuggling of radioactive materials is one of the main concerns addressed in most countries' national security strategy or policy. This is because the smuggled radiological sources can be used to create radiological dispersal device (RDD) to strike fear and create unrest among public citizens. This could inflict significant socioeconomic costs due to the evacuation and relocation processes, as well as the extensive decontamination efforts.

In the United States National Strategy for Counterterrorism for example, one of the efforts to support the strategic objectives is to integrate a broader set of tools to counter terrorism [1]. One of the main methods of scanning for illicit radiological materials is the use of the stationary radiation portal monitors (RPMs). There are close to 1400 RPMs deployed all across the United States, and these require maintenance and refurbishment at the end of the 10 to 13 years of estimated service life, involving hundreds of millions dollars of expenditure [2]. The latest sustainability studies done by the Domestic Nuclear Detection Office (DNDO) in 2016 found that the RPM fleet could remain operational until 2030 [2]. However, due to the expected reduced budget in the future which is mainly

caused by the global recuperation from the COVID-19 pandemic, the consideration of broader tools to counter terrorism is more important now.

One study proposed that the RPMs could be replaced by mobile radiation detection systems (MRDs) which was found to suppress the adversary's success rate due to its discrete operation [3]. Various related studies and detection system development were also done [4–6] that could help decision makers on the local, state, tribal, territorial government and international levels to place an optimal nuclear security program. Along with the aforementioned studies, the research presented in this paper offers one of the potential tools to support counterterrorism activities.

Compressed sensing principles were incorporated in the proposed system design. Instead of the typical application of compressed sensing in the signal processing of a system, this study is interested in the feasibility of compressed sensing application to the gamma source imaging system's design. The radiation source imaging concept developed in this research could allow for a monitoring system tool that determines the shape and localization of the imaged radiation source. This paper presents the benchmarking of the proposed system's simulation results against the experimental measurements for a point ^{137}Cs source in a proof-of concept setting. This serves as a validation for the simulation, allowing for further design improvements to be applied for potential real-life application.

5.1.1. Overview of the proof-of-concept gamma source imaging system

The proof-of-concept system consisted of a collimator array made of 11-by-11 polyvinylchloride (PVC) pipes of 1.27-cm radius, placed upright in the middle of a water-filled 250-gallon rectangular tank. Six Geiger-Mueller (GM) detectors were placed in a

radial arrangement beneath the tank. The gamma source to be imaged was placed above or directly on top of the collimator. The details of the design process that led to this system were presented for the imaging of a neutron source through Monte Carlo N-Particle (MCNP) simulations [7]. Similar process was followed for the imaging of a gamma source and the final design for benchmarking was selected. Figure 5-1 shows the setup of the selected system proposed in this research. The details of how measurement data was processed were also provided in [7] and a summary of the data-processing procedure is summarized next in this section.

The PVC pipes that make the 11-by-11 collimator were filled with either water or air in a random combination. The random water-air combination was generated using a Python code and as many as 100 combinations were generated. Each combination was called a configuration and measurement readings from the GM detectors beneath the tank were recorded for each configuration. These configurations were represented as a 100-by-121 matrix, labeled as matrix A, where each configuration was each placed in 100 rows.

The GM detector in counts corresponding to each configuration were represented as a 100-by-1 matrix, labeled as matrix b. The image of the gamma source was represented as an 11-by-11 matrix, labeled as matrix x, which was solved for using the relation $Ax = b$ with the non-negative least-squares method. The solution was obtained by minimizing the l_2 of b-Ax with the condition that $x > 0$. This was done using the *lsqnonneg* function in *MATLAB* and the solution was plotted as an 11-by-11 image, showing the position of the point gamma source.

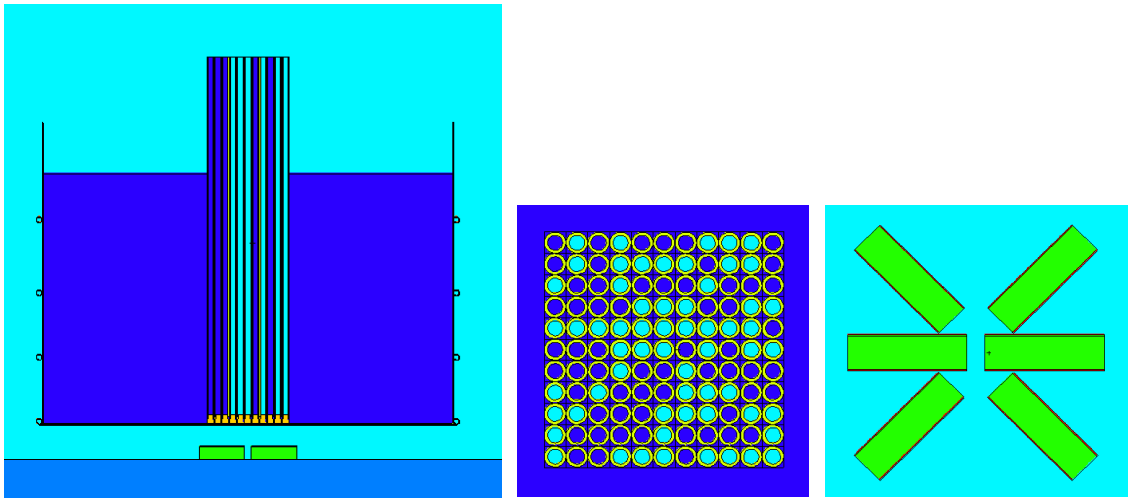

(a) (b) (c)

Figure 5-1. The x-z plane view of the system at y = 0 showing water (blue color) in the tank and in some of the collimator channels, as well as air (cyan color) in the surrounding and in some of the collimator channels (a), the top view of an example of a collimator configuration (b), and the arrangement of the GM detectors underneath the tank (c). Images were generated using the MCNP Visual Editor program.

5.2. Methods

MCNP simulations were performed for four different cases using a 14.8-MBq (0.4-mCi) point ^{137}Cs source. Experimental apparatus was built with parameters as close as possible to those of the MCNP simulation model. Qualitative and quantitative comparisons were made between simulation and experimental results.

5.2.1. Case definition

Four cases varying in source location were defined for the validation. The first case was defined as the ^{137}Cs source being placed on top of the collimator and at the center. The source placement of the ^{137}Cs in the second case was 27.94 cm above the collimator. The third case was similar to the second case but with an aluminum alloy piece placed beneath the ^{137}Cs source. This was done to observe the effect of shielding on the reconstructed image quality. Finally, the ^{137}Cs source was placed near one corner of the

collimator. Figure 5-2 shows the location for each case. These cases were defined for comparison between simulation and experimental results.

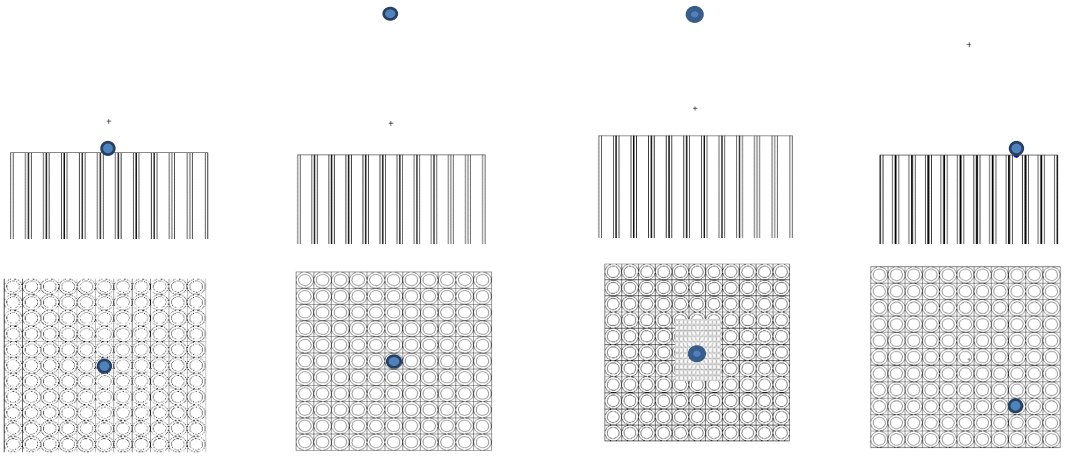

Figure 5-2. The location of the ^{137}Cs source (blue dot) for the center, above, above metal and corner case (from left to right). The top images show the side view of the collimator, and the bottom images show the top view.

An additional case was done for the physical measurements where the source was placed on top of the collimator, and between the middle and one edge of the collimator. This was designated as an "unknown" position without any prior simulation results to compare with. This position was shown in Fig. 5-3. The position of the ^{137}Cs source was referred to by the row and column position as (6, 8), corresponding to the sixth row from the top and the 8th column from the left of the collimator face.

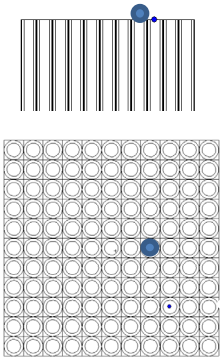

Figure 5-3. The "unknown" position (6, 8) in the experimental measurements, in addition to the four previously defined cases.

5.2.2. MCNP simulations

The MCNP model shown in Fig. 5-1 was completed with a simulated 14.8-MBq (0.4-mCi) ^{137}Cs point source. The F4 tally was used to determine the expected counts from the GM detectors according to the procedure outlined in Section 4. This method of processing the F4 tally from the MCNP output was validated against experimental measurements for simple geometries and two extremes of the collimator configuration, which were fully water-filled or fully empty configuration.

Each detector was represented in the MCNP model by a cylindrical neon gas, covered by an aluminum casing with the dimensions of the Ludlum 44-7 GM counter used in the physical experiment [8]. It was modeled with an active length of 13.2 cm, radius of the neon gas volume of 1.905 cm and aluminum casing thickness of 0.1556 cm.

F4 tallies were assigned to the neon volumes and the conversion from the F4 tally to the expected counts in 15 minutes was performed as outlined in Section 4. The summation of the expected counts from each detector in each configuration was

represented as the b matrix. The image reconstruction was carried out using *MATLAB* and the image matrix x was plotted using the *imagesc* function in *MATLAB*.

The image matrix resulted from using the *lsqnonneg* function in *MATLAB* was normalized to the largest element value before it was plotted using the *imagesc* function in *MATLAB*. The position of the largest element value in the matrix was the indicator of the imaged point gamma source location. The largest normalized element in x was represented by yellow and the smallest element value was blue according to the "parula" colormap setting in *MATLAB* as shown in Fig. 5-4.

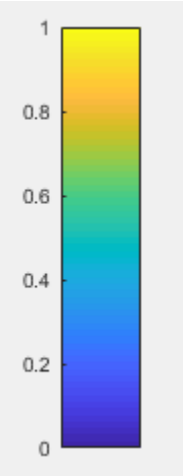

Figure 5-4. The assigned normalized values (0 to 1) of the pixels in the "parula" colormap in *MATLAB*.

5.2.3. Experimental measurements

Six Ludlum 44-7 GM detectors were placed underneath the 250-gallon water tank. Each of the GM detectors was connected to a Ludlum 2200 rate meter. The GM detectors were arranged as close as possible to the simulated arrangement. The measurement for each configuration was set to be 15-minute long with the source, and 15 minutes for

background. Using a water pump, each pipe was filled or emptied according to the matrix *A* used in the simulation.

The net counts for each measurement were calculated by subtracting the corresponding background counts from each measurement with a source in the location specified in Fig. 5-2 and Fig. 5-3. The net counts from all detectors were summed and put into the b matrix. The image was reconstructed after new measurements were taken every few days. When no more improvement in the image was expected with additional measurements, further measurements were ceased for the case that had successfully localized the source.

5.2.4. Validation metrics

The true solution, x_0 for each case with an ideal design and environment for the imaging of a point source should be an image consisting of only one brightly-lit pixel (yellow color) in the expected pixel location. The reconstructed images for all cases were compared to the true solution in both qualitative and quantitative analyses. The reconstructed images using simulation and experimental results were expected to portray visual artifacts due to the limitation of the non-negative least square method and imperfection in the overall design and assembly of the system. These artifacts, which are pixels in colors that represent non-zero values other than the value of "1" in positions that are supposed to have a value of "0" (blue color), are referred to as noises in the image. Both quantitative and qualitative metrics were utilized in evaluating the performance of the proposed system.

5.2.4.1. Quantitative metric

To derive the validation metric, the sample and model means were first defined. The sample mean was the average measurement from the experiment and the model mean was the simulated measurement using the MCNP model. The best estimate for the sample mean of counts from a collimator configuration in each case was the summed net counts measured. The model mean was the summed simulated counts for the corresponding configuration in each case. The plot of the sample mean, the model mean and 90% experimental confidence interval was presented for each of the four cases. This was done to roughly compare the simulated data trend to the experimental data trend.

$$\text{Estimated error, E} = \text{Model mean} - \text{sample mean} \qquad (5-1)$$

A validation metric, E was defined as the discrepancy between the simulated results (model mean, y_m) and the experimental results (sample mean, y). The E is also known as the estimated error. Equation 5-1 shows the definition of the estimated error. Based on the defined validation metric, two different plots were provided to help with future analysis of the proposed system as suggested in [9].

The first one was the plot of E and the 90% true mean confidence interval for each case. Two derived global metrics, the average relative error, $|\frac{E}{y}|_{\text{ave}}$ with 90% confidence interval and the maximum relative error, $|\frac{E}{y}|_{\text{max}}$ with 90% confidence interval, were also reported for each plotted case. The E and 90% true mean confidence interval plot would be useful in demonstrating whether model accuracy is comparable to the confidence interval associated with the average relative error.

The second plot presented for each case was the E and the 90% true error confidence. This plot helps in the assessment of the simulation model accuracy and identifying possible improvements of the proposed system model's performance. The global metrics and the 90% confidence intervals for the true mean and the true error were calculated according to the equations outlined in [9].

5.2.4.2. Qualitative metric

Qualitatively, the images reconstructed from the simulation and experimental results were visually compared to determine if localization of the ^{137}Cs source was successful. The localization was confirmed by identifying the pixel with the maximum value, which is the yellow pixel. Localization is said to be successful if the yellow pixel was identified in the right location for that particular case. The lowest number of measurements needed to correctly localize the ^{137}Cs source was identified for each case. The noise pixel is defined as any pixels that do not have the value of either 0 or 1. According to Fig. 5-4, pixels that are not yellow or blue in color (colors at both extremities in the "parula" colormap) are called the noise pixels. The number of noise pixels observed in each reconstruction was visually analyzed and compared between cases.

5.3. Results and Discussion

5.3.1. Quantitative analysis

Figure 5-5 shows the plots of y, y_m and 90% true mean confidence interval for the center, above, above metal and corner cases. The lower and upper boundaries of the 90% true mean confidence interval give the range that contains the true mean of the summed

net counts with 90% probability for each configuration. Figure 5-5 demonstrates that majority of the values from simulations does not fall within the true mean 90% confidence interval. Only 55%, 71%, 54% and 59% of the simulation datapoints fall within the 90% experimental confidence interval in center, above, above metal and corner cases, respectively. Despite the seemingly apparent disagreement between simulation and experiment results from Fig. 5-5, the discrepancy can be further scrutinized by plotting the estimated error, E and the 90% true mean confidence interval (Fig. 5-6), as well as the E and the 90% true error confidence interval (Fig. 5-7).

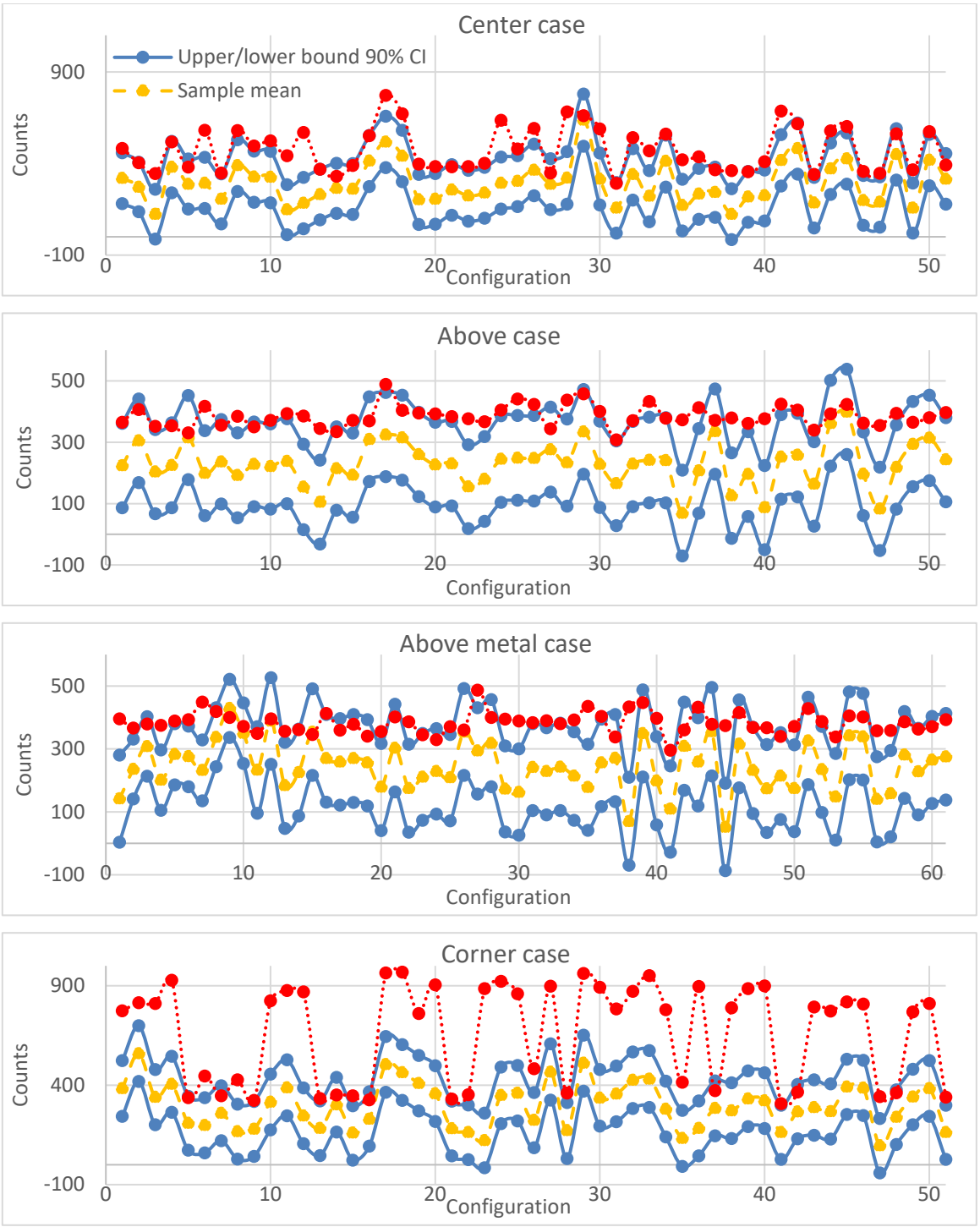

Figure 5-5. The plots of sample mean (dashed line), model mean (dotted line) and 90% true mean confidence interval (solid lines) for the center, above, above metal and corner cases.

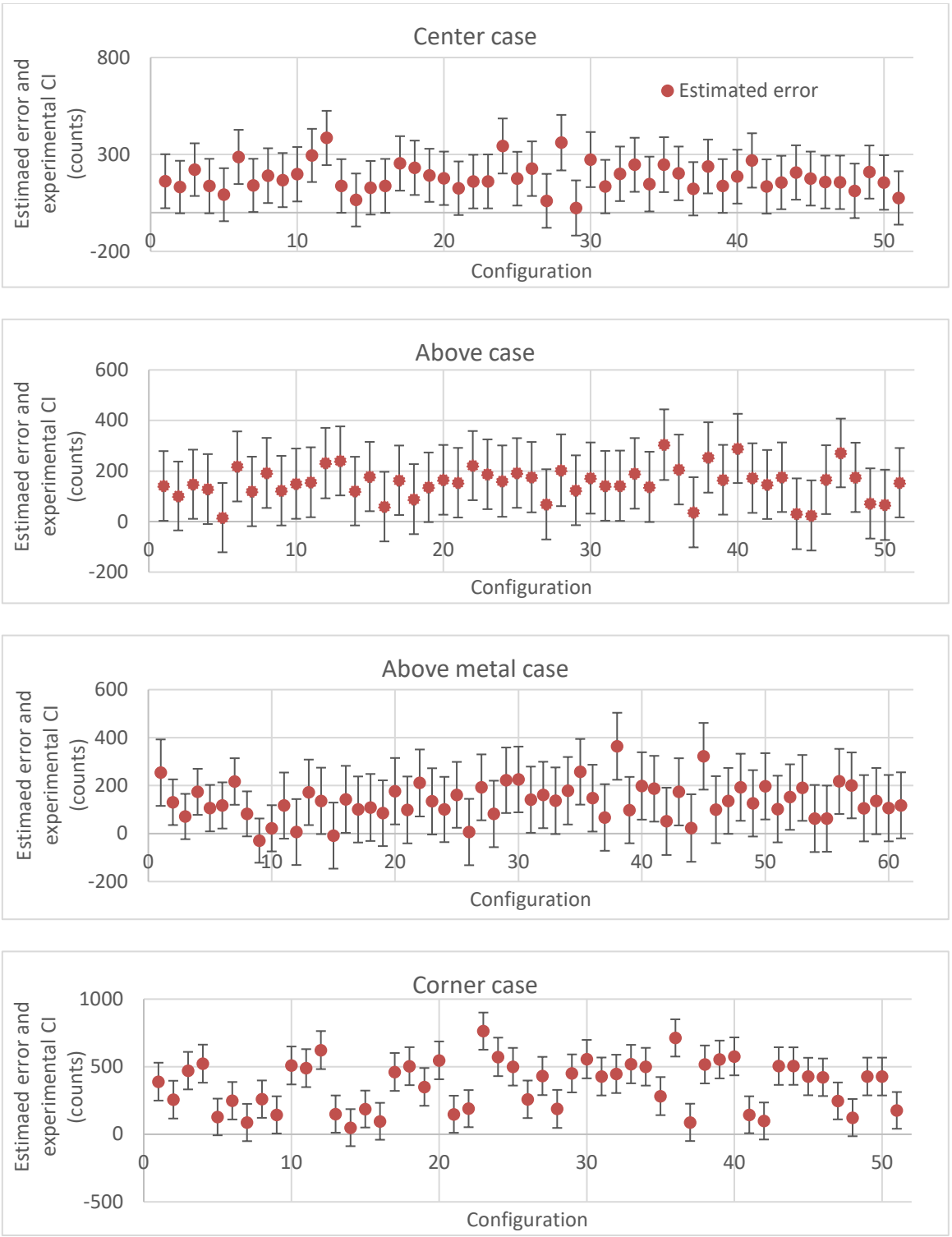

Figure 5-6. The plots for estimated error, E (red dots) and the 90% true mean confidence interval (error bars) for the center, above, above metal and corner cases.

Figure 5-6 shows 55% of the E values falls within 90% true mean confidence interval in the center case, 71% in the above case, 54% in the above metal case and 59% in the corner case. This indicates that modeling errors do exist and that the model could be further improved to represent the actual experimental set up. The MCNP model indeed was different from the physical system in terms of the material compositions, the assembly of the proposed system, and the detectors' responses. It was therefore expected that the estimated error to fall outside of the 90% true mean confidence interval. These differences are further discussed with respect to the qualitative evaluation in the next section.

The average relative error, $|\frac{E}{y}|_{ave}$ and the average maximum error, $|\frac{E}{y}|_{max}$ for each case are tabulated in Table 5-1. For all of these cases, there was a significant difference between the $|\frac{E}{y}|_{ave}$ and the $|\frac{E}{y}|_{max}$ as these values are not statistically the same. The significant difference between the $|\frac{E}{y}|_{ave}$ and the $|\frac{E}{y}|_{max}$ values indicates that the plots in Fig. 5-6 and Fig. 5-7 need to be examined carefully to evaluate the model trend with respect to the experimental data trend.

The $|\frac{E}{y}|_{max}$ occurs at configuration 12 ($|\frac{E}{y}|$ = 2.1) in the center case, configuration 35 ($|\frac{E}{y}|$ = 4.4) in the above case, configuration 45 ($|\frac{E}{y}|$ = 6.2) in the above metal case and configuration 23 ($|\frac{E}{y}|$ = 6.3) in the corner case. These points can be seen to be above the upper bound of 90% confidence interval blue line in Fig. 5-6. There are one datapoint that result in a relative error of more than two in the center case, five in the above case, two in the above metal case and three in the corner case. These datapoints consequently cause the average relative error to be higher and can be clearly seen for the above metal and

corner cases, where the largest discrepancy between the simulation and experiment results is more than six times the measurement value. Other than these extreme datapoints, the other $|\frac{E}{y}|$ values are consistently less than two, which means that the discrepancy between simulation and experimental results at each configuration is less than a factor of two when compared to the corresponding experiment measurement.

Table 5-1. The $|\frac{E}{y}|_{\mathbf{ave}}$ and uncertainty with 90% confidence interval and the $|\frac{E}{y}|_{\mathbf{max}}$ and uncertainty with 90% confidence interval.

Case	Average relative error, $\|\frac{E}{y}\|_{\text{ave}}$	Maximum relative error, $\|\frac{E}{y}\|_{\text{max}}$
Center	1.068 ± 0.540	2.092 ± 0.761
Above	0.878 ± 0.683	4.409 ± 2.025
Above metal	0.950 ± 0.751	6.197 ± 2.673
Corner	1.345 ± 0.550	6.257± 1.126

Figure 5-7 shows the validation metric, E with 90% true error confidence interval for each case. These plots provide useful information regarding the performance of the proposed system model in terms of the true error best approximation from the experiments. This plot allows for model assessment with the purpose of improving it. The largest estimated error occurs at configuration 12 (E = 385) in the center case, configuration 35 (E = 304 counts) in the above case, configuration 38 (E = 503) in the above metal case and configuration 23 (E = 763) in the corner case. These configurations happen to be the same ones at which the largest $|\frac{E}{y}|_{\text{max}}$ occur except for in the above metal case. This indicates that configuration 12, configuration 35, configurations 38 and 45, and

configuration 23 might not be suitable for use in the center, above, above metal and corner case, respectively.

While randomness typically results in incoherence in matrix A, which is one of the requirements for a better likelihood of successful signal recovery, it does not guarantee incoherence. The coherence of a matrix is the largest absolute normalized inner product between its columns, which characterizes the dependence between different columns [7]. To improve the image quality, these configurations could be substituted with different random configurations. This might require multiple testing attempts by taking measurements for the new configurations and comparing the results with those of MCNP simulations. Despite the statistically different results for these configurations, the images reconstructed using these results still correctly localized the gamma source, which demonstrates the robustness of the proposed system.

Alternatively, the MCNP model could be improved with the aim of reducing or minimizing the estimated errors for all of these cases. However, in this research, it was apparent and demonstrated in the next section that localization was successful with the current model. It was concluded that the MCNP model accuracy is sufficient for its intended use. Therefore, it would make more sense to remove the data corresponding to the configurations with large E and add new configurations if needed, instead of modifying the MCNP model to represent the physical set up more closely.

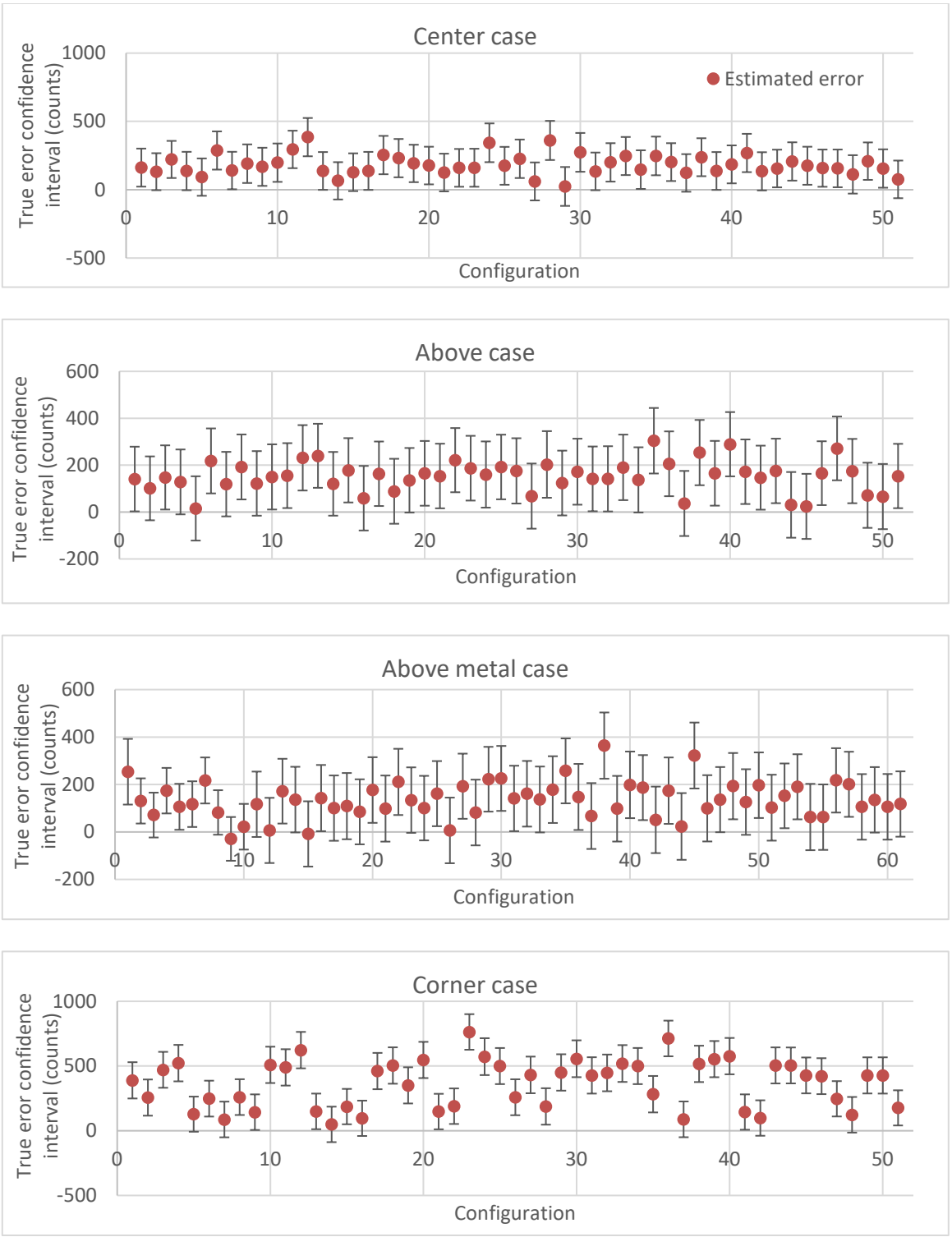

Figure 5-7. The plots for estimated error, E (red dots) and the 90% true error confidence interval (error bars) for the center, above, above metal and corner cases.

5.3.2. Qualitative analysis

Figure 5-8 shows the plot of the image matrix x for increasing number of measurements, m for all the cases. The ^{137}Cs source was localized with m = 21 in the experiment and m = 26 in the simulation for the center case. The localization for the above case was apparent starting at m = 46 in the experiment. While it is not visible in the plots that the ^{137}Cs source was localized at the maximum number of measurements performed, the localization was achieved at m = 55 in the simulation. For the above metal case, the localization was successful starting at m = 55 in the experiment and m = 61 in the simulation. For the corner case, the proposed system localized the ^{137}Cs source with m = 16 in both simulation and experiment.

The image reconstruction results for the cases with the ^{137}Cs source placed in contact with the collimator were visually more conclusive compared to the other two cases. This is characterized by the lower amount of apparent noise pixels (non-zero pixels other than the highest-valued pixel that are > 0.5) in reconstructed images. In the center and corner cases, the experiment image has no apparent noise pixels at maximum m. The number of apparent pixels for the above and above metal cases in simulation and experiment are shown in Table 5-2.

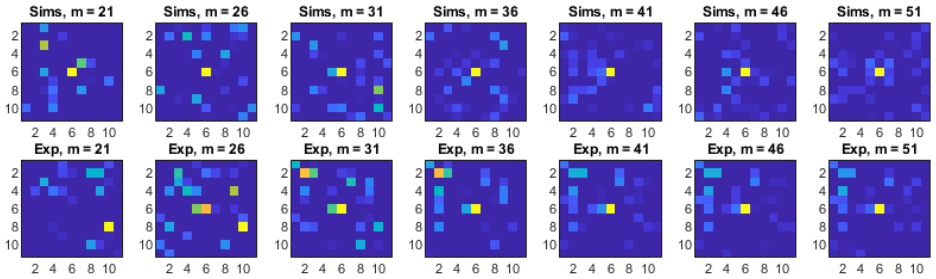

(a)

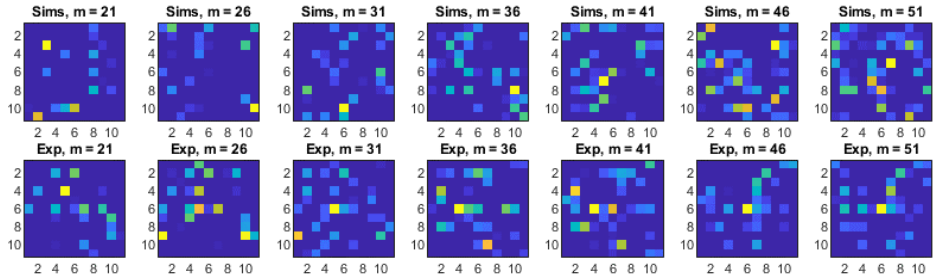

(b)

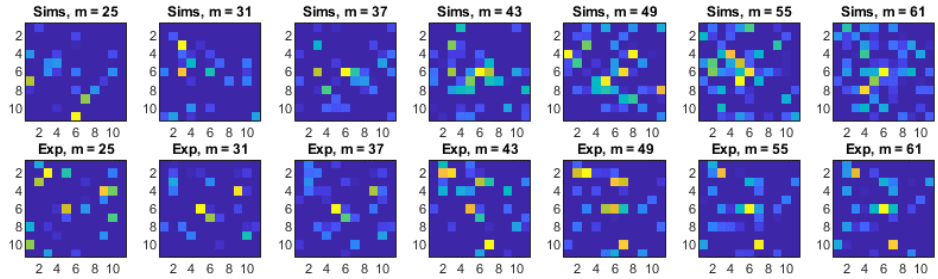

(c)

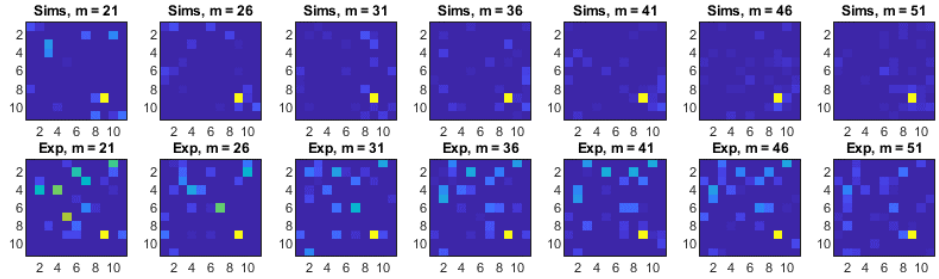

(d)

Figure 5-8. The comparison of reconstructed images with increasing number of simulated (Sims) and experimental configurations (Exp), m for the (a) center case, (b) above case, (c) above metal case and (d) corner case.

The fact that there are no apparent noise pixels in the center and corner cases after a certain number of measurements aligns with the visual results of these cases that appear more conclusive than those of the other two cases. It is worth noting that this is partly a limitation on the choice of colors for the plot's colormap. In the case of a point source, the colormap settings can be set to give an extreme contrast between the highest element value and the rest of the element values. However, information on the size or shape of an area source would be lost if this same colormap was applied.

Table 5-2. The amount of apparent noise pixels for each case in simulations (Sim) and experiments (Exp) and the number of measurements at which there were no more apparent noise pixels.

Case	Apparent noise pixels (Sim)	Apparent noise pixels (Exp)	m_0 (Exp)	m_0 (Sim)
Center	0	0	31	39
Above	9	3	None	None
Above metal	4	2	None	None
Corner	0	0	19	40

As shown in Table 5-3, despite having between 23.1% to 26.4% total noise pixels, a single highest-valued pixel (yellow pixel) was shown in the correct position in each of the cases in Fig. 5-9. It was expected that the images produced from the center case counts have clearer representation of the source location because of the shorter source-to-detector distance. With a greater source-to-detector distance, the buildup effect due to the scattering of the photons was more pronounced, resulting in higher counts detected for every configuration. This affected the reconstruction algorithm results in the form of noise

pixels, in which pixels that were supposed to have zero value ended up having a non-zero value.

This scattering effect can also be seen with the corner case where the source was placed closer to the surrounding water, causing the total noise pixels to be the highest. Regardless, the additional scattering effects in the experimental setting could have actually contributed to a better resolved image. The reason is these excess counts that occurred in the simulations were suppressed in the experiments. As photons lost their energy with every scattering event, absorption interactions were more likely to occur in the collimator material instead of being detected. This was evident from the fact that there were less noise pixels present in experimental images than in the simulation images by approximately a factor of two, as summarized in Table 5-3.

Table 5-3. The amount and percentage of noise pixels for each case in simulations (Sim) and experiments (Exp).

Case	Noise pixels (Sim)	% Noise pixels (Sim)	Noise pixels (Exp)	% Noise pixels (Sim)
Center	50	41.3	28	23.1
Above	50	41.3	31	25.6
Above metal	60	49.6	31	25.6
Corner	50	41.3	32	26.4

The discrepancies between the simulation and experiment images were expected because of the unavoidable differences between the MCNP simulation model and the physical system. While the physical system was assembled as close as possible to the MCNP model, several inevitable differences still exist. The detectors used in the

experiment had different responses and sensitivities, but the detectors in the MCNP model behave similarly. The collimator in the experiment was not assembled or placed perfectly as modeled in the MCNP simulations. The material compositions might be different in the physical system than the generic compositions used in the MCNP model.

All of these differences contributed to differences in the interaction rate of photons travelling towards the detectors. Imperfections in the physical system assembly would have resulted in different rates of photon scattering, leading to certain detectors registering more or less photons than in the idealized simulation. The resulting count readings caused the noise pixels to appear in different locations and intensity than in the simulation images. Nevertheless, localization of the gamma source occurred for all cases in both simulations and experiments.

Figure 5-9 shows the image reconstruction results as the number of measurements was gradually increased for the "unknown" position in the experiment. The correct localization at position (6, 8) was achieved with measurements starting at m = 11. Since the source-to-detector-array distance is the same as the center and corner cases, it was expected that the amount of noise artifact in the reconstructed image was similar to those of the center and corner cases. The noise pixels account for 23.1% of the total pixels for the "unknown" case. There were zero apparent noise pixels starting at m = 9. It was indeed visually demonstrated that the source localization was easily distinguishable compared to the above and above metal cases.

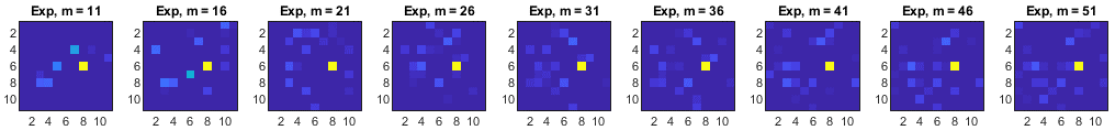

Figure 5-9. Experimental comparison of reconstructed images with increasing number of measurements, m for the "unknown" source position.

It was acknowledged that modeling errors do exist from the presented analysis but based on the qualitative analysis, the MCNP model accuracy was sufficient for its intended use, which was the correct localization of the imaged gamma source. The results presented here demonstrated that the imaging concept is robust as the proof-of-concept system was shown to successfully localize the gamma source both in simulations and experiments. This was possible even with the fact that modeling errors were shown to be significant. Further investigations that might be of interest would be to image multiple gamma sources, a line source or an area source. Aside from different source characteristics, an investigation on the use of different types of detectors might also be worthwhile. The validation process and results presented in this paper serve as a starting point to further expand and consolidate the available tools for counter-terrorism monitoring activities.

5.4. Conclusion

This paper has demonstrated the validation process for the MCNP model of a proposed gamma source imaging system with experimental measurements. The validation was done for four cases with different gamma source locations. The physical set up was tested with an "unknown" source position without any simulation results to compare with. Quantitative evaluations were made for the four cases by using the validation metric, defined as the estimated error, E. The plot of E and 90% experimental confidence interval

for each case was presented, together with the corresponding average and maximum relative errors with the respective 90% confidence interval. Analysis of this plot showed that the discrepancy between simulation and experimental results at each configuration was less than a factor of two when compared to the corresponding experiment measurement, except for at most five extreme datapoints (in the above metal case).

Another plot of E with the 90% true error confidence interval was also included to evaluate the performance of the proposed system model. This plot allowed for identification of one to two configurations that resulted in the highest E in each case. Qualitative evaluation was discussed by visually examining the reconstructed images resulting from MCNP simulations and experimental measurements. Even though total noise pixels in the reconstructed images are between 23.1% and 26.4% of the total pixels, a single highest-valued pixel (yellow pixel) was shown in the correct position in each of these cases.

Differences between the simulation and experimental results were also discussed in detail, leading to the conclusion that the system model was shown to represent the experiment model based on the similar and proven capability of correctly localizing the gamma source. The localization was successful in both simulations and experiments for all four cases, as well as the “unknown” source location in the experiment. These results have demonstrated that the proposed system is a promising alternative in supporting the development or integration of a new technique or technology to existing counter-terrorism efforts.

5.5. Acknowledgements

We thank Ryan Stolt, Zachary Jones, Robert Kollman and Dalton Wise for assistance in conducting the experimental measurements. We also thank Dr. Cable Kurwitz for providing a laboratory space for our experiment to be completed.

5.6. References

[1] "National Strategy for Counterterrorism of the United States of America." The White House, Oct. 2018. [Online]. Available: https://www.dni.gov/files/NCTC/documents/news_documents/NSCT.pdf

[2] "Report to the Ranking Member, Committee on Homeland Security, House of Representatives: Radiation Portal Monitors.," United States Government Accountability Office, GAO-17-57, Oct. 2016. [Online]. Available: https://www.gao.gov/assets/690/680706.pdf

[3] R. Coogan, C. Marianno, and W. Charlton, "A strategic analysis of stationary radiation portal monitors and mobile detection systems in border monitoring," *Nuclear Engineering and Technology*, vol. 52, no. 3, pp. 626–632, Mar. 2020, doi: 10.1016/j.net.2019.08.010.

[4] L. Caballero *et al.*, "Gamma-ray imaging system for real-time measurements in nuclear waste characterisation," *J. Inst.*, vol. 13, no. 03, pp. P03016–P03016, Mar. 2018, doi: 10.1088/1748-0221/13/03/P03016.

[5] C. Pană, S. Severi, and G. T. F. de Abreu, "Super-accurate source localization via multiple measurement vectors and compressed sensing techniques," in *2018 IEEE*

Wireless Communications and Networking Conference (WCNC), Apr. 2018, pp. 1–5. doi: 10.1109/WCNC.2018.8377451.

[6] K. Vetter, R. Barnowksi, A. Haefner, T. H. Y. Joshi, R. Pavlovsky, and B. J. Quiter, "Gamma-Ray imaging for nuclear security and safety: Towards 3-D gamma-ray vision," *Nuclear Instruments and Methods in Physics Research Section A: Accelerators, Spectrometers, Detectors and Associated Equipment*, vol. 878, pp. 159–168, Jan. 2018, doi: 10.1016/j.nima.2017.08.040.

[7] N. Anuar, C. Marianno, and R. G. McClarren, "Employing MCNP to optimize experimental design for compressed sensing neutron source imaging," *Nuclear Instruments and Methods in Physics Research Section A: Accelerators, Spectrometers, Detectors and Associated Equipment*, vol. 954, p. 161446, Feb. 2020, doi: 10.1016/j.nima.2018.10.124.

[8] "Model 44-7 Alpha-Beta-Gamma Detector Manual," *Ludlum Measurements, Inc.* https://ludlums.com/images/product_manuals/M44-7.pdf (accessed Dec. 13, 2020).

[9] W. L. Oberkampf and M. F. Barone, "Measures of agreement between computation and experiment: Validation metrics," *Journal of Computational Physics*, vol. 217, no. 1, pp. 5–36, Sep. 2006, doi: 10.1016/j.jcp.2006.03.037.

6. PROPOSED DESIGN RECOMMENDATIONS TO IMPROVE A COMPRESSED-SENSING-BASED GAMMA SOURCE IMAGING SYSTEM

6.1. Introduction

The objective of this paper was to study design factors to improve the performance of a gamma source imaging system. The preliminary system design originally consisted of an array of 11-by-11 polyvinylchloride (PVC) pipes that served as a collimator, and placed vertically in a water-filled 250-gallon rectangular tank. The detection system comprised of six GM detectors that were placed in a radial arrangement beneath the tank and collimator. The gamma source to be imaged was placed either directly on top of the collimator or above it. Measurements were taken for multiple collimator configurations in order to have sufficient information for image reconstructions. Results and comparisons between simulation and experimental measurements for the proposed system were discussed in depth in Section 5.

6.1.1. Motivation and Objectives

The original proof-of-concept design was a bulky system that required an area of 2-by-2 m^2 to operate. It was designed with a limited budget resulting in a very basic representation of the idea of imaging using the compressed sensing principles. This led to the creation of a proof-of-concept system that weighed more than 0.8 tons, causing it to be a stationary system that cannot be easily transported. Since the proposed system model was experimentally validated, one of the most desirable improvements of the model was to reduce the size of the overall system. Two main factors were studied in order to make

the system more portable, which were the choice of the materials and to reduce the number of detectors.

Once a much smaller system was demonstrated to perform well, sensitivity analyses were done for the collimator channel size and the source distance from the collimator or detector. The study on the collimator channel size was important to identify its effects on the image artifacts (noise pixels), as well the number of measurements required to obtain sufficient information for image reconstruction. The radiation source distance from the collimator or detector was studied to determine if there were any significant effects to the localization accuracy.

Next, a different type of detector was examined with the use of the improved model design. The reconstructed images from the use of a sodium iodide (NaI) detector were then compared with those of a GM detector. Discussions on the advantages of utilizing spectroscopy with the system are provided in this paper.

Finally, an example of a design improvement for the model was presented based on the latest available technology [1]. Based on these results, high-level design recommendations were proposed to guide the design process for an improved model. These serve as general guidelines in encouraging new and better designs that adopt the proposed design concept as the design baseline.

6.1.2. Radioactive source imaging for nuclear security

There were various news reports on clandestine black-market operations circa 2010 [2–5]. While these criminals were apprehended and more information was gathered through extended investigations, the fact that multiple attempts of illegal transactions of

nuclear and radioactive materials were ongoing within a span of ten years was concerning. The attempted sale of a small amount of highly-enriched uranium sample for hundreds of thousands of dollars suggested that real demand for these materials exists and that the unlawful suppliers have significant inventory or network access to these materials. There was no report on the syndicate being completely brought down, which indicates that these activities could still be ongoing or will likely continue if or when attention on this syndicate gets shifted.

It was also reported that some of these offenders believed that radioactive materials had high value but ended up struggling to look for buyers. These resulted in improper disposal of radioactive materials which posed risks to public health [6]. The International Atomic Energy Agency (IAEA) Incident and Trafficking Database (ITDB) reported an average of 130 incidents per year between 1993 to 2019 for incidents unrelated to malicious use [7]. These incidents and other undetected operations of the same nature call for the need to strengthen nuclear security frameworks and international co-operations.

Detection and imaging in nuclear security serves to provide timely and accurate identification, as well as evidence to support legal proceedings against the offenders with the aim to eliminate trafficking networks [6], [8]. These objectives can be fulfilled by a combination of multiple radiation detection systems while ensuring minimal exposure to personnel on duty. There are four basic types of radiation detection equipment. These are fixed radiation portal monitors (RPMs), personal radiation detectors (PRDs), hand-held gamma and neutron search detectors (GSDs and NSDs), and hand-held radionuclide identification devices (RIDs) [6].

Some of the main factors to be considered when selecting the types of technology for radiation detection include the ability to identify and localize radioactive sources, the field of view, the targets and time constraints. There are recommendations by the IAEA in collaboration with World Custom Organization (WCO), EUROPOL and INTERPOL on the requirements for gamma-ray systems. One of the requirements is for the system to have a false alarm rate of less than one in every 12 hours for pocket instruments, less than six per hour for handheld instruments and less than one per day for fixed-installation instruments [9].

Factors affecting the proof-of-concept system model were studied with the aim to fulfill the objectives of radioactive source imaging in nuclear security. An example of an improved design that falls between the fixed installation category and a handheld category is presented in this paper, based on the findings on the investigated factors. This design example was inspired by a product developed by the Australian Nuclear Science and Technology Organization (ANSTO) [1].

The scope of this paper is limited to the design factors of the collimator and the type of detectors used. Therefore, improvements related to the image reconstruction method and the system requirements are not discussed in this paper as they have been discussed in earlier work [cite]. However, it is emphasized here that in a complete design process for a finalized radioactive source imaging system design, the IAEA recommendations for alarm activation and false alarm rate requirements should be included [9].

6.2. Methods

Changes in the original system model were made according to three phases. The first phase aimed to reduce the system size by at least half (Section 6.2.2). The second phase used the material and dimensions obtained from the first phase. Changes were made to the model to study the effect of the collimator channel size and the source distance from the detector on the reconstructed images (Section 6.2.3). The third phase studied the use of a different type of detector to be employed with the results obtained in phases one and two (Section 6.2.4).

The models with particular changes added in each phase were called test models. Comparison metrics were defined to ensure standardized and clear contrast between the original model and the test models, or between the cases with the same test model. Both quantitative and qualitative metrics were used in evaluating the results from changes made to the original model in each phase.

For all of the reconstructed images, the position of the highest-valued pixel in the image matrix indicates the imaged gamma source location. The procedure of image reconstruction was outlined in Section 5. The highest-valued pixel has a value of 1 and is represented by yellow and the smallest has a value of 0, represented by blue according to the “parula” colormap setting in *MATLAB* as shown in Fig. 6-1.

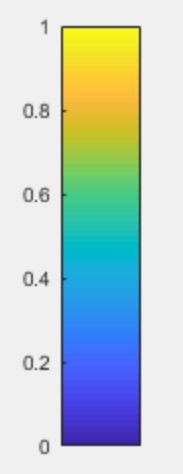

Figure 6-1. The assigned values (0 to 1) of the pixels in the "parula" colormap in MATLAB.

6.2.1. Comparison metrics

The comparison metrics were defined as the differences between the true solution and the test model solution. Test models were the models with specific changes added with the intention to improve a certain aspect of the original model. Two different metrics were defined for each test model, which were comparisons in (1) the percentage of noise pixels, which are pixels with a non-zero value in locations where the pixel is supposed to have a value of 0; (2) and the visual analysis of the reconstructed images from test models with the expected (true) image solution. In addition to (1), the percentage of noise pixels with values more than 0.2 were also reported for the models' reconstructed images. Based on the chosen colormap in Fig. 6-1, noise pixel values that are larger than 0.2 are visually different than the blue color of zero value. These pixel values also represent a more than 20% deviation from the zero value. Therefore, it is useful to track the number of these pixels as it can be an indicator of the reconstructed image accuracy.

6.2.2. System model size reduction

The original system model that consisted of a 250-gallon rectangular water tank, an 11-by-11 PVC collimator and six GM detectors is shown in Fig. 6-2 (Section 5). Simulations were first performed by substituting water with material candidates of four mean free paths as the thickness. An example of the test model 1 is shown in Fig. 6-3. These materials were aluminum, iron, copper, tungsten and lead. The thicknesses of the material candidates are listed in Table 6-1. Four mean-free-path values were chosen because they represent 98.2% attenuation of the incident radiation.

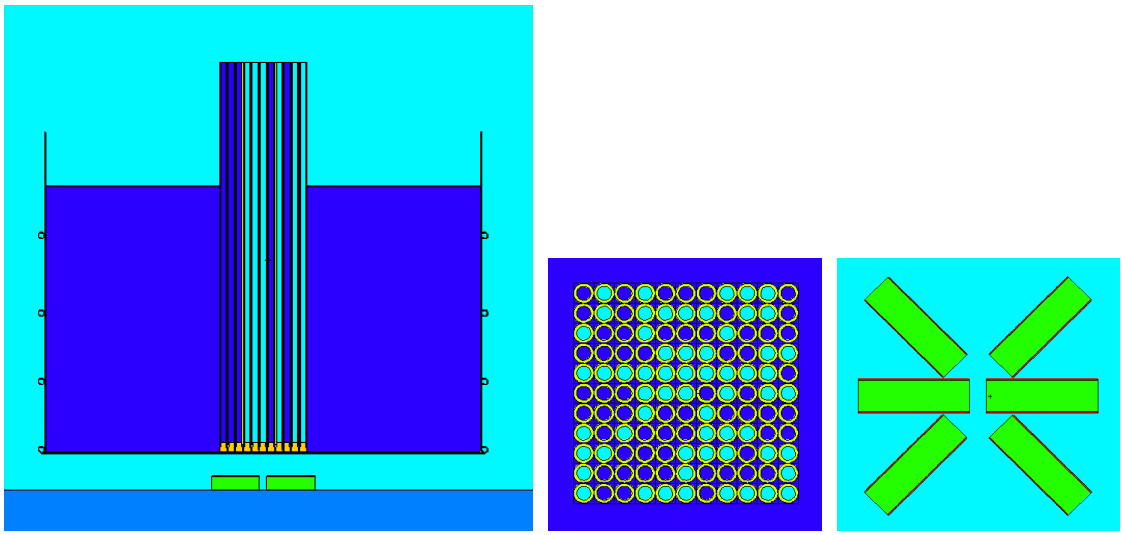

(a) (b) (c)

Figure 6-2. The x-z plane view of the system at y = 0 showing water (blue color) in the tank and in some of the collimator channels, as well as air (cyan color) in the surrounding and in some of the collimator channels (a), the top view of an example of a collimator configuration (b), and the arrangement of the GM detectors underneath the tank (c). Images were generated using the MCNP Visual Editor program.

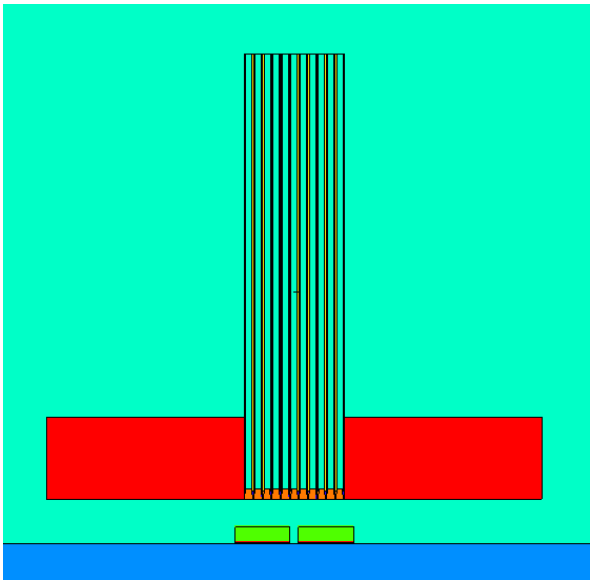

Figure 6-3. The x-z plane view of the test model 1 at y = 0 with an all-empty configuration (all collimator channels filled with air). The tank and the metal cage that holds the tank were removed from the model as they were only needed to contain water in the original model. The material candidate is denoted by the red-color block with the respective calculated four mean free paths as its thickness. Image was generated using the MCNP Visual Editor program.

Table 6-1. The material candidates, their densities and the respective calculated thicknesses (four mean free paths).

Material	Density (gcm^{-3})	Thickness (cm)
Aluminum (Al)	2.70	19.75
Iron (Fe)	7.87	6.87
Copper (Cu)	8.96	6.11
Tungsten (W)	19.30	2.06
Lead (Pb)	11.35	3.10

Expected counts were simulated in MCNP for an all-full collimator configuration and an all-empty configuration. The all-full configuration was when all of the PVC pipes were filled with water and the all-empty configuration was when the pipes were all filled

with air. Simulations were performed for three cases, which were when the ^{137}Cs point gamma source was placed (1) in the center and on top of the collimator, (2) in the center and 27.94 cm above the collimator, and (3) in the corner and on top of the collimator. These positions are depicted in Fig. 6-4. For each of these cases, the expected counts for the all-full and all-empty configurations were determined.

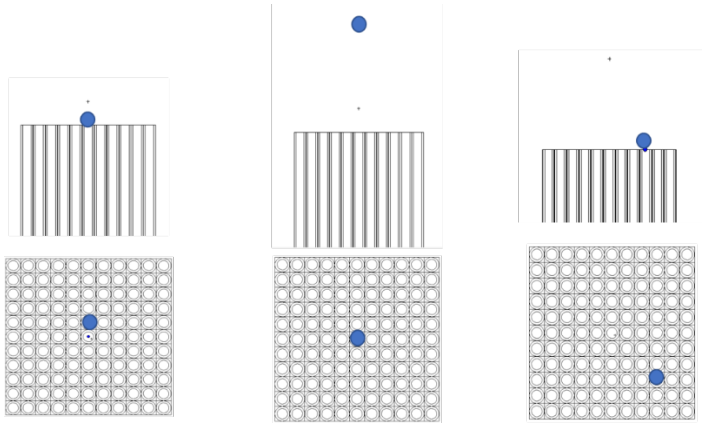

Figure 6-4. The location of the ^{137}Cs source (blue dot) for cases (1) center, (2) above and (3) corner case (from left to right). The top images show the side view of the collimator, and the bottom images show the top view.

The desirable results from these simulations were minimum expected counts with the all-full configuration and maximum expected counts with the all-empty configurations. These characteristics mean that the material is shielding as much source gammas as possible when the radiation is meant to be shielded and allowing a maximum reach the detector as possible when the radiation is not meant to be shielded. Consequently, to capture these two requirements, materials with the higher all-empty-to-all-full ratios were said to be the more efficient material candidates. The ratios were then reported for each material candidate in each case for the test model 1. A material was then

chosen to substitute water and the collimator material to make the test model 2, which has further reduced size compared to that of the test model 1.

6.2.3. Sensitivity analyses

The test model 2 is depicted in Fig. 6-5 with lead as the substitute material for water and PVC in the original design for different source-to-detector distances. This was done to see the effect of increasing source distance from the detector on the reconstructed image for test model 2 set up. The first case was 25% of the original source-to-collimator distance (d = 29.3 cm), the second was 12.5% of the original source-to-collimator distance and the third had the source directly on top of the collimator. The images were plotted as the number of configurations, m used for the reconstruction, increased up to m = 50 to identify the m value resulting in the correct source localization.

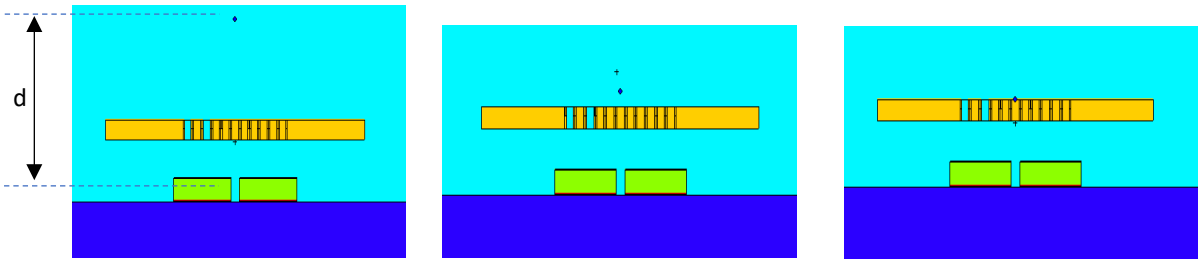

Figure 6-5. The location of the ^{137}Cs source (blue dot) for test model 2 at (a) d = 29.3 cm, (2) d = 14.66 cm and (3) d = 12.1 cm.

Next, the collimator channel radius for the test model 2 was varied by reducing it to 25% and 12.5% of the original radius (1.27 cm or ½"). The ^{137}Cs point source was positioned 15 cm away from the center of the detectors. Figure 6-6 depicts the top view and the side view of two different channel radii with the same 11-by-11 total pixels. Image

reconstruction was also performed with increasing m for both radii to see the effect on source localization. Finally, using one selected channel radius, the number of total pixels for test model 2 were varied to see the effect on image reconstruction and source localization. The collimator sizes simulated were 19-by-19 and 43-by-43. The reconstructed images were also compared for these aforementioned collimator sizes with different total pixels.

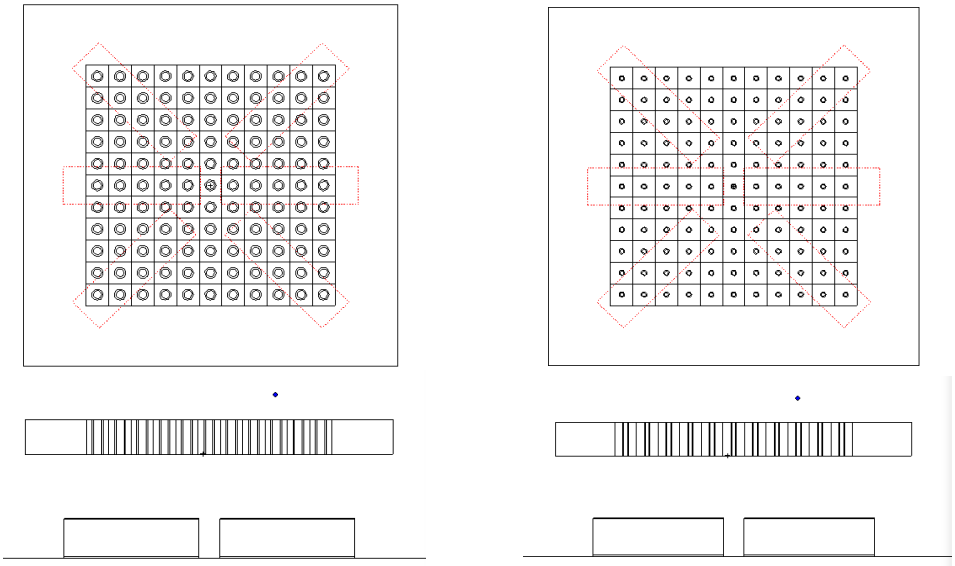

Figure 6-6. The 11-by-11 lead collimator with 0.635-cm (¼") pipe radius (left) and 0.3175-cm (⅛") pipe radius (right) for test model 2. The top images show the top view of the collimator, with the six GM detectors underneath the collimator outlined with red dotted-lines and the bottom images show the side view collimator and the detector on the x-z plane at y = 0.

6.2.4. Detector systems

Another aspect of interest in improving the original design of the system was to investigate the use of spectroscopy data for image reconstruction. Simulations were done to study the effect of having different detectors on source localization. In addition, the number of detectors was also reduced from six to just one detector and the collimator

channel was changed to have a square shape. The GM detector has a length of 13.2 cm and a radius of 1.905 cm. Figure 6-7 shows the top and cross-sectional side view of the test model 3 with two different types of detectors, a GM detector and a NaI detector. Simulations were performed for a point ^{137}Cs source, which was 2.56 cm away from the surface of the collimator in the center, corner, and (4, 8) positions. However, only the corner position results are used for described below as it is the more challenging problem where the gamma source position does not align with the detector position. Reconstructed images were plotted with increasing m for these cases.

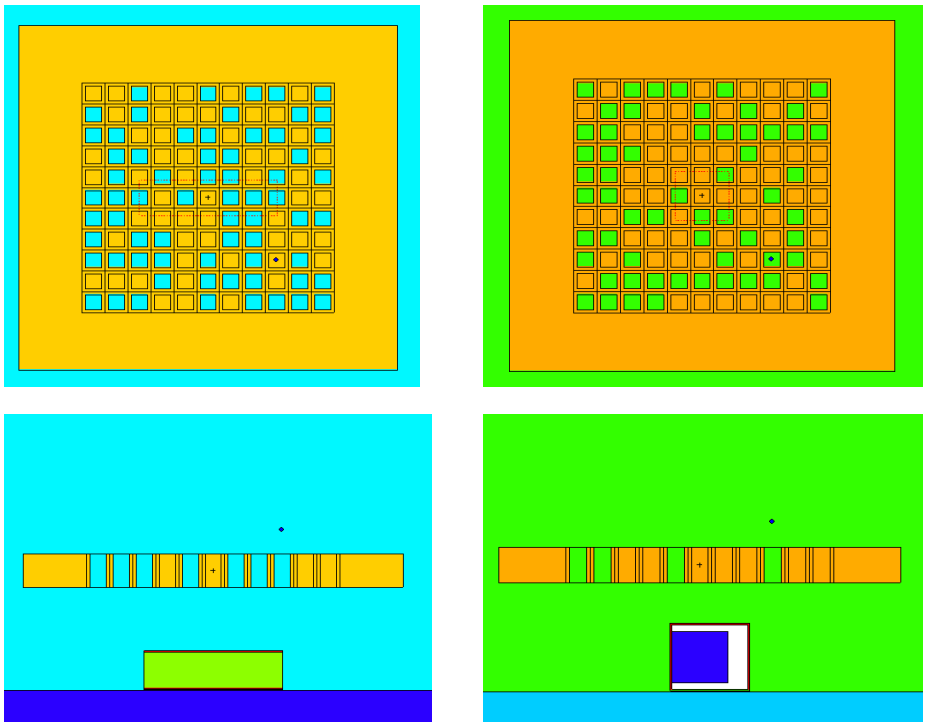

Figure 6-7. The test model 3 for localization of a point ^{137}Cs source (blue dot) placed in the corner position with a GM detector (left picture) and a NaI detector (right picture). Pictures in the top row are the top view of the set up (x-y plane) with the detector outline shown, and bottom row pictures are the cross-sectional side view of the set up on the x-z plane at y = 0.

The NaI detector used with the test model 3 was a 2”-by-2” NaI crystal enclosed in an aluminum casing filled with vacuum. The FT8 GEB entry was enabled with the parameter values associated with the crystal size. Image reconstruction was done using the 662-keV photopeak counts and results with the two different detectors were compared.

6.2.5. An example of design improvement

It was proposed to surround the detector with a lead collimator in order to facilitate detection and imaging within 360° view. This was inspired by a recent product released by ANSTO [1]. In order to test the performance of the proposed model, simulations were made using a 5.2”-by-8.3” NaI detector and a uniform disk source with a radius of 10 cm. Figure 6-8 shows the top view and the cross-sectional views of test model 4. The FT8 GEB entry in the source definition (SDEF) MCNP input was turned off due to the unknown parameter values for the size of the NaI crystal used in the simulation.

Considering a conservative approach due to the complexity of the design relative to the test model design, the gamma source energy was reduced to a value that maximizes energy deposition in the crystal, instead of 662 keV. The four-mean-free-paths value for a 662-keV gamma is more than the diameter of the crystal (13.26 cm versus 13.2 cm). So, a gamma energy of 300 keV was chosen to ensure that gammas are absorbed within the crystal (four-mean-free-paths value is 6.58 cm). Images produced through these three steps were then shown side by side for comparisons at m = 50 for each source distance, using the photopeak counts.

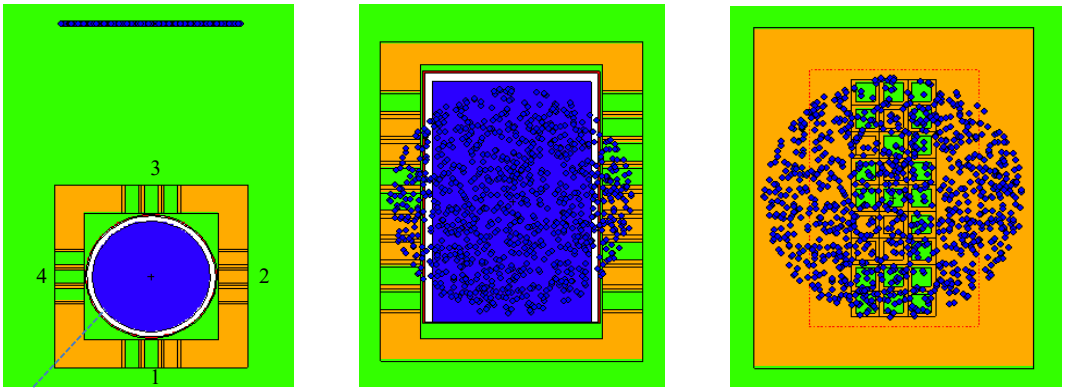

(a) (b) (c)

Figure 6-8. The test model 4 schematics with a 5.2”-by-8.3” NaI detector (blue) surrounded by a lead collimator (orange), showing (a) the top view of the set-up depicting the position of the disk source, (b) the cross-sectional view of detector on the x-z plane at y = 0 and (c) the cross-sectional view of the collimator, outlining the detector position and size relative to the collimator. The blue dots show the sampling positions that make the uniform disk source. Each side of the collimator is labeled as side 1, 2, 3 and 4 as indicated in (a).

6.2.6. High-level design recommendations

Based on the presented results, a set of high-level design recommendations was developed to guide the process of designing a radioactive source imaging system that uses compressed sensing principles. High-level design helps translate product objectives and requirements to the overall general system design, resulting in high-level design solutions. High-level design solutions are then used for low-level design, which describes the subsystems and components needed in detail. Therefore, it would be beneficial to develop high-level design recommendations that can serve as guidance to design the product which could be one of the four categories outlined in Section 6.1.2. These recommendations list down aspects to be considered in the design process and are elaborated in 6.3.5.

6.3. Results and Discussion

6.3.1. System model size reduction

Figure 6-9 shows the ratio of the expected counts from the all-empty configuration to the all-full configuration for each case. Lead has the highest ratio, followed by tungsten for all of the cases. The ratios are higher in Case 1 (center) and Case 3 (corner) than those of Case 2 (above) because of the shorter distance between the source and the detector. As intensity generally decreases with increasing distance between the source and the detector, the expected counts with the all-empty configuration in Case 2 would be lower than those in the center and corner cases. This resulted in the statistically lower ratios for Case 2.

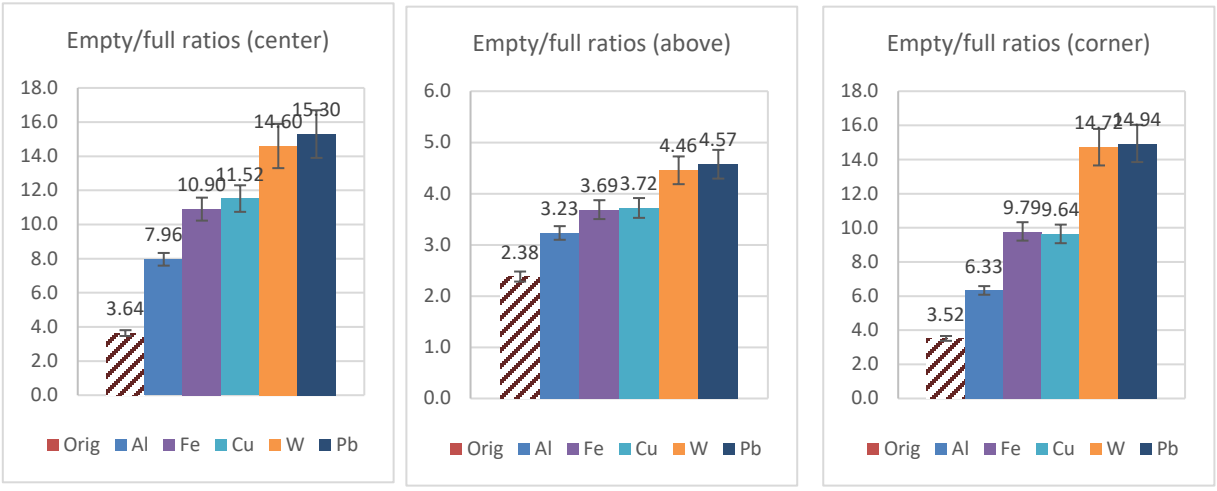

Figure 6-9. The all-empty-to-all-full ratio for each material candidate in Case 1 (left), Case 2 (middle) and Case 3 (right).

The results in Figure 6-9 suggest that lead and tungsten are the most efficient among the material candidates. Since lead has the highest all-empty-to-all-full ratio in all cases, simulations of test model 1 were performed for the three cases as defined in Fig. 6-4 with lead as the substitute for water surrounding the collimator. Random combinations

of water and air were again employed in these simulations and image reconstruction was performed with the number of configurations, m until 30.

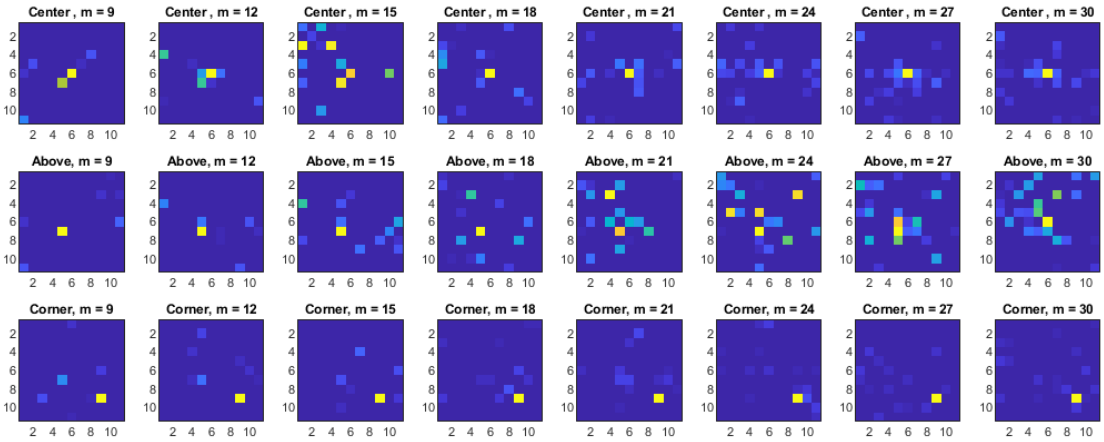

Figure 6-10. The localization of a ^{137}Cs gamma source for Case 1 (center), Case 2 (above) and Case 3 (corner) using test model 1 with lead as substitute for water.

Figure 6-10 shows the image reconstruction results for the three cases defined in Fig. 6-4. Localization was apparent starting m = 18 for Case 1, m = 30 for Case 2 and m = 9 for Case 3. The noise pixels are 24% of the total pixels in all of the cases at m = 30. Noise pixels with values larger than 0.2 are 0.8%, 10.7% and 0% of the total pixels in the center, above and corner case, respectively. Noise pixels were expected to be higher in Case 2 because of the larger distance between the gamma source and the detectors.

The larger source-to-detector distance caused more scattering events to be detected resulting in higher counts registered, appearing as noise pixels in the reconstructed images. Cases 1 and 3 were expected to give correct localization at lower m compared to Case 2, and this was demonstrated in Fig. 6-10 to be true. Tungsten has statistically the same ratios for all three cases and could be a potential collimator material too. Even though the thickness of a tungsten collimator is less by 1 cm, the mass of it would be 5.9 kg more

than a lead collimator because of its higher density (listed in Table 6-1). With these results, lead was chosen as the material to substitute water in the original design, as well as to replace the PVC material of the collimator. This resulted in a size reduction by 68% compared to the validated original design model (2-by-2 m2 versus 0.36-by-0.36 m2) and mass reduction by 94.6% (852 kg versus 46 kg).

6.3.2. Sensitivity analyses

Figure 6-11 shows the reconstructed images for test model 2 with increasing m for different source distances. At m = 50, the noise pixels are 40.5%, 39.7% and 19% of the total pixels for d = 29.3 cm, d = 14.66 cm and d = 12.1 cm case, respectively. Additionally, noise pixels with values larger than 0.2 in d = 29.3 cm image are 18.2% more than those in d = 14.66 cm case. With the source on top of the collimator, there were no pixels with values larger than 0.2 in the reconstructed image at m = 50.

As the source was moved further away from the collimator surface, higher number of noise pixels was visible in the reconstructed images. As expected, the further the source is, the more scattering events take place and get detected. This resulted in higher amount of noise pixels in the image. These results also show that at a larger distance, more configurations are needed get a more resolved image. The localization was apparent at m = 10 when the source was placed directly on top of the collimator. Further away at d = 14.66 cm, localization was only accurate starting at m = 20. At even a larger distance, localization was not conclusive even with m = 50. However, it was expected that localization would be resolved with higher m value.

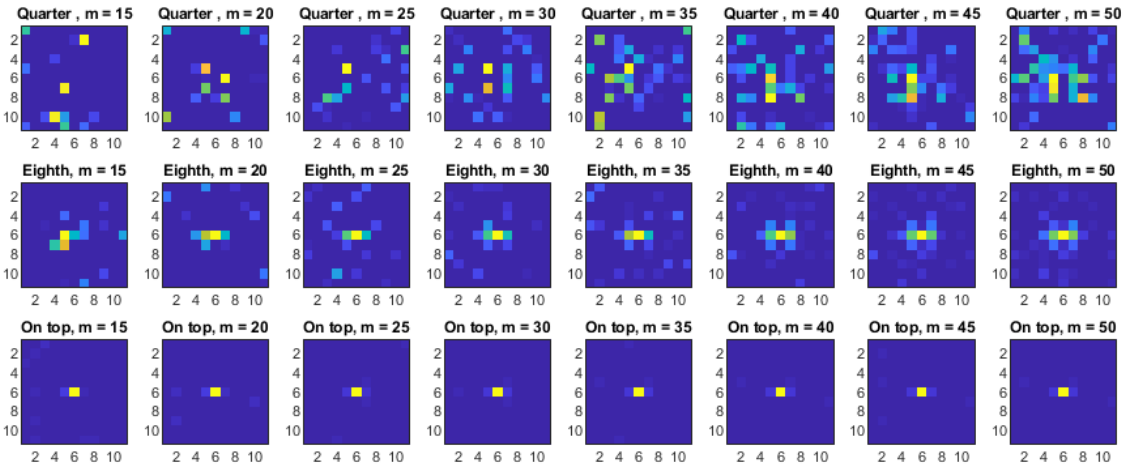

Figure 6-11. The localization of a ^{137}Cs gamma source for test model 2 at a quarter of the original distance, d = 29.3 cm (top row), an eighth of the original distance, d = 14.66 cm (middle row) and at the top of the collimator, d = 12.1 cm (bottom row). All distances, d, are relative to the center of the GM detector.

Figure 6-12 compares the reconstructed images for test model 2 with increasing m for two different pipe radius sizes. The noise pixels are 40.5% of the total pixels for both collimator channels with radii of ¼" and ⅛" at m = 50. However, the noise pixels with values of more than 0.2 in the image produced with ⅛" pipe radius data are 5% more than those of the ¼" pipe radius, as evident in Fig. 6-12. Smaller collimator channel meant that there was more shielding material available, resulting in increased scattering and therefore the appearance of more noise pixels in the image. Smaller channel size also limited the number of photons reaching the detector, causing the need for more m to resolve the localization. This is shown in Fig. 6-12 where the quarter case localization is apparent at m = 20 while the eighth case is at m = 30.

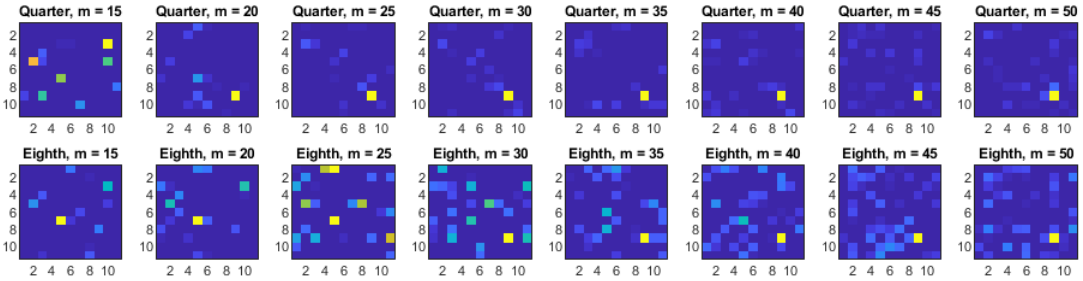

Figure 6-12. The localization of a ^{137}Cs gamma source, positioned 14.66 cm away from the center of the detectors and placed in the corner position, with ¼" pipe radius (top row) and ⅛" pipe radius (bottom row).

Next, the number of total pixels for the test model 2 was varied while keeping the channel radius fixed at ⅛" and the point ^{137}Cs source placed in the corner position. Figure 6-13 shows the images plotted with increasing m for a 19-by-19 collimator and a 43-by-43 collimator. The noise pixels are 13.6% of the total pixels for the 19-by-19 collimator at m = 50 and 8% for the 43-by-43 collimator at m = 150.

The noise pixels with values of more than 0.2 in the 19-by-19 image are 3.4% more than those of the 43-by-43 image at the highest m for each case. Since a higher number of total pixels requires higher number of measurements to accurately localize the gamma source, the test model 2 with 43-by-43 collimator was expected to localize the source at a higher m. This is evident in Fig. 6-13 that localization was resolved at m = 134 for the test model 2 with 43-by-43 collimator compared to at m = 50 for the 19-by-19 collimator.

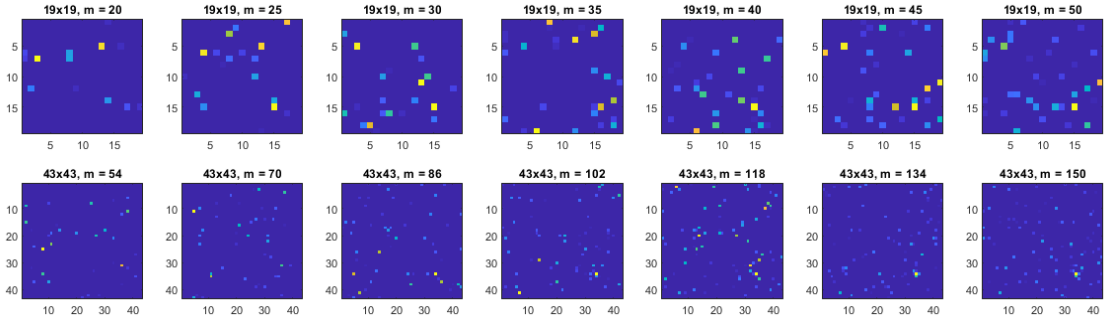

Figure 6-13. The localization of a point ^{137}Cs source placed in the corner position, 15 cm away from the collimator surface, with collimator channel radius of ⅛" for increasing m. The collimator sizes simulated were 19-by-19 (top row) and 43-by-43 (bottom row).

6.3.3. Detector systems

Figure 6-14 shows the comparison between test model 3 with a GM detector and a NaI detector with a point ^{137}Cs source placed in the corner position. The images were plotted with increasing m until m = 30 for both detectors. The noise pixels are 24% of the total pixels for both detectors at m = 30. However, noise pixels with values larger than 0.2 are 0.8% more in the GM image compared to that of the NaI image. It is demonstrated that localization was successful in both cases as a single yellow pixel was expected to be in the (8, 8) position in the image. Localization was successful starting at m = 15 in both cases. As shown in Fig. 6-7, even though both detectors were not positioned directly below the point gamma source, the reconstructed image using data from the detectors showed the correct position of the gamma source.

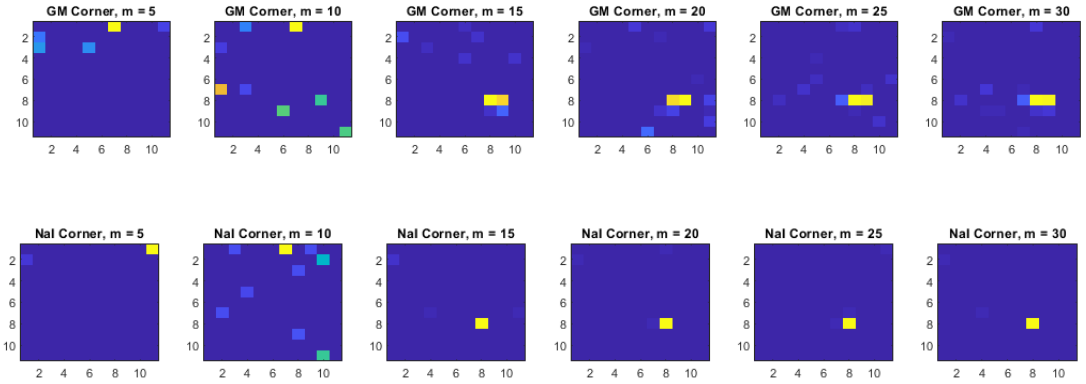

Figure 6-14. The localization of a ^{137}Cs gamma source 2.56 cm away from the collimator surface using test model 3 with ¼" channel opening width for the corner case with a GM detector (top row) and a NaI detector (bottom***).***

Based on the results in Fig. 6-14, the NaI simulated counts resulted in a more conclusive image that accurately pinpoints the position of the gamma source. The GM simulated counts resulted in an extra yellow pixel next to the one in the correct position, as well as more noise pixels. This was due to the fact that the GM detector counts included the scattered photons compared to the NaI counts, in which only the photopeak counts were used in the image reconstruction.

The scattering effects seen by the GM detectors and appeared as noise pixels in the reconstructed images were shown to be limited by using spectroscopy data as it is possible to filter out counts that are due to scattering interactions. This proves that spectroscopy data is useful in minimizing the noise pixels due to scattering effects in reconstructed images. However, the GM detector result did not deviate from the correct solution. This suggests that if limited budget was an issue, the use of a proposed imaging system with one or multiple GM detectors could also be practical.

6.3.4. Example of design improvement

The design factors found from various test model results were incorporated in this improved design example. The same collimator material used in the test models, lead, was used in this design. A square collimator channel opening with twice the width of test model 3 was used to maximize gamma detection in the crystal. The number of channels were also minimized according to the size of the NaI detector used (5.2”-by-8.3”) resulting in a collimator face with 9-by-3 channels on each side. Since the design was intended to be used with a much larger standoff distance compared to the distances tested with previous test models, a NaI detector was chosen as the detection system to minimize distortion in the reconstructed images produced.

Source localization was done by going through three steps of image reconstruction. Each step uses a different number of collimator sides for image reconstruction. The first step was by using all four collimator sides (faces). The image produced using four sides is shown in Fig. 6-15 (b) where the first three columns of pixels in the left side of the image represent side 1, followed by side 2, side 3 and side 4. This gives a 9-by-12 image with 108 total pixels, since each side has 9 rows and 3 columns of channels (9×3×4). One way to help visualize which area in the reconstructed image refers to which collimator side is to imagine cutting along the dotted blue line in Fig. 6-15 (a), pull the cut edge of side 4 in a clockwise direction, turning the 4 sides into one, single side and then lay the collimator flat on its inner side. If a disk source was placed facing side 3 as shown in Fig. 6-15 (a), all of the pixels in columns 7 through 9 in the 9-by-12 image are expected to be yellow in color.

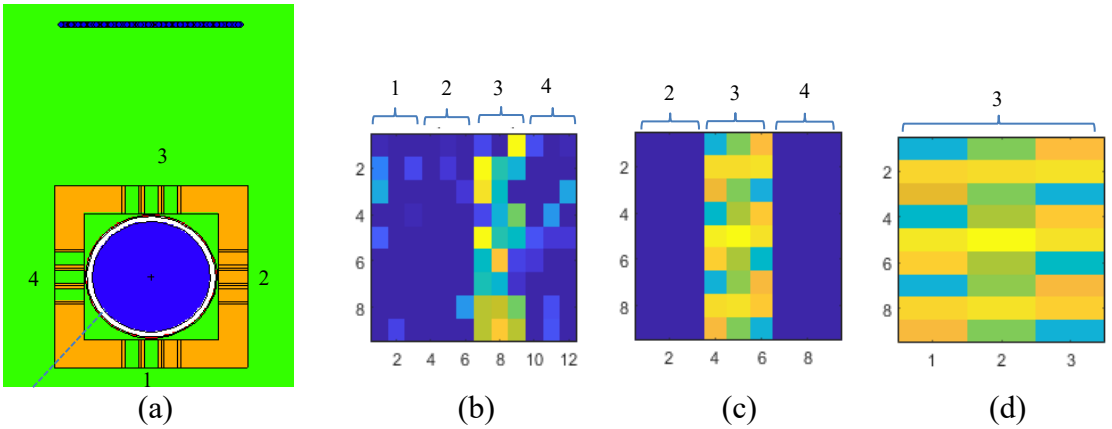

Figure 6-15. The test model 4 schematics with a 5.2”-by-8.3” NaI detector (blue) surrounded by a lead collimator (orange), showing (a) the top view of the set-up depicting the position of the disk source with the collimator sides labeled. The corresponding sides in the reconstructed images by (b) using all four sides (108 pixels), (c) using three sides (81 pixels), and (d) using one side (27 pixels) of the collimator.

Once it was determined that the source was facing side 3, the second step was to reconstruct the image by using only three sides of the collimator, which are the side facing the source and the two adjacent sides of it. This then gives a 9-by-9 image as shown in Fig. 6-15 (c), and it was expected that pixels in the fourth column until the sixth column would be yellow in color because these three columns in the middle represent side 3. And finally, image reconstruction was done using only one collimator side that is facing the source. This results in a 9-by-3 image and for the disk source in Fig. 6-15 (a), all pixels within this 9-by-3 image shown by Fig. 6-15 (d) were expected to be yellow in color.

Figure 6-16 shows images reconstructed through the three steps described previously. The results are displayed with increasing number of measurements, m for a monodirectional uniform disk source. Since the diameter of the disk source was as big as one side of the collimator face, it was expected that pixels in columns that represent the location of the source would be gradually filled with non-blue pixels as m was increased.

The first step in the localization process was to use all sides of the collimator in reconstructing the image. As shown in the top row of Fig. 6-16, the portion of the picture that represents the side facing the disk source consisted of a color mixture suggesting that a source was detected in the associated direction (side 3). Due to the higher number of pixels in the images produced from all collimator faces (108 pixels), more measurements were needed to produce an image with the expected result, which was yellow pixels in all rows between the 7th and the 9th columns.

The next step was to perform image reconstruction using three faces of the collimator that indicated the presence of the disk source. Based on the image at m = 50 in the top row of Fig. 6-16, the sides to be used for image reconstruction in the second step were sides 2, 3 and 4. As shown in the middle row of Fig. 6-16, when reconstructed using three faces of the collimator, the middle section of the picture (the collimator side facing the disk source) turned yellow at m = 50. Since there was a smaller number of channels used for reconstruction (81 pixels), localization converged at a lower m compared to that in the first step.

The third step was to reconstruct the image using the side that indicated the location of the disk source, which was side 3. This can be seen in the bottom row of Fig. 6-16 where the reconstructed image shows all-yellow pixels starting at m = 30. Since the number of channels used in reconstructing the images was even less (27 pixels), localization was achieved at a lower m compared to that in step 2.

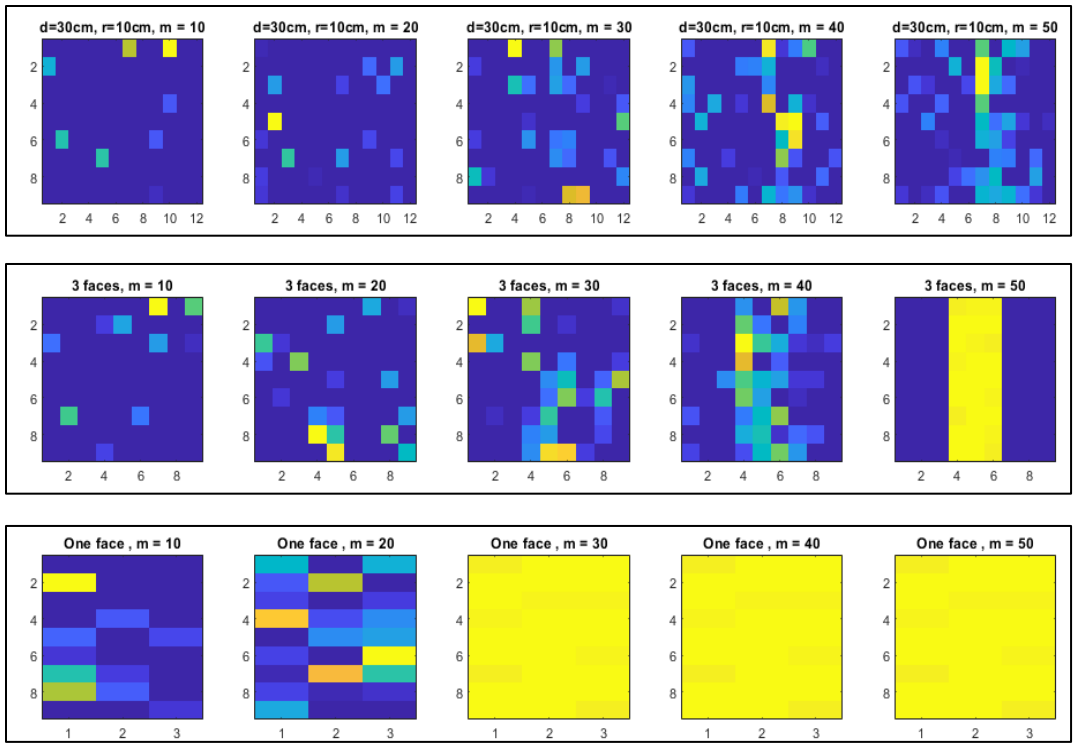

Figure 6-16. The localization of a 300-keV monodirectional uniform gamma disk source with a radius of 10 cm, placed 30 cm away from the center of the detector. Images were plotted for increasing number of measurements, m considering all sides of the collimator (top row), three sides of the collimator (middle row) and only one side of the collimator (bottom row).

Another three simulations were performed with a 300-keV isotropic uniform gamma disk source at a distance, d = 30 cm, 60 cm and 120 cm. Figure 6-17 shows the image reconstruction comparisons at m = 50 for these simulations. At d = 30 cm, the image of the monodirectional disk source is more resolved than that of the isotropic disk source. The scattering due to photons entering the collimator from different directions resulted in count increase or decrease with each collimator configuration. This led to noise pixels to appear in the reconstructed image. As the isotropic uniform disk source was moved further away from the detector and collimator, the images started to be filled with more yellow

pixels when reconstructions were done with a single face and with three faces of the collimator. This was as expected because as the source was placed further away, photons arriving at the collimator appeared to come from a monodirectional uniform disk source.

In Section 6.3.2, the results showed that the further the gamma source away from the detector, the larger the number of noise pixels appear in the images. Therefore, the results in this section are interesting because it means that imaging a radiation source that is far away from the detector and collimator is possible with a spectroscopic detector. Figure 6-17 shows that the larger distance is beneficial in producing more conclusive images. However, the downside of imaging from a larger distance is that longer measurement time is needed for sufficient counts as radiation intensity drops by square of distance. For this design, these three steps of plotting the reconstructed images can be utilized to help determine the position of the source with respect to the 360° view.

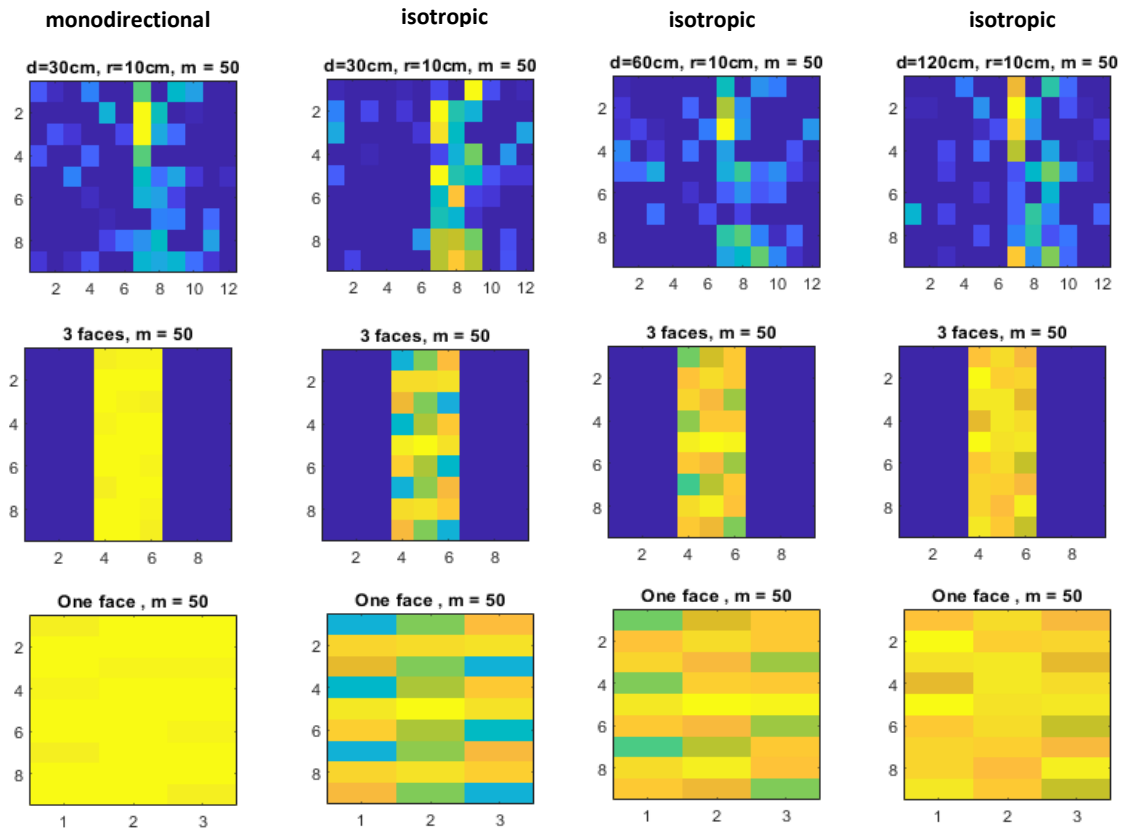

Figure 6-17. The comparison of images reconstructed using photopeak counts for each of the four cases; (left to right) a monodirectional uniform disk source 30 cm away from the center of the NaI detector, an isotropic uniform disk source 30 cm away, an isotropic uniform disk source 60 cm away and an isotropic uniform disk source 120 cm away from the center of the NaI detector.

6.3.5. High-level design recommendations

Based on these results, a list of high-level design recommendations was developed to guide the design process for a radioactive source imaging system using compressed sensing principles. The design process starts with the product objectives and requirements, which differ based on the type of equipment the developer chooses to design or build. The equipment type can either be a stationary installation system such as the RPM, a portable system or a hybrid system. In summary, the factors to be considered in the design process

are the materials used for the collimator, the collimator channel size, the number of collimator channels, the source-to-detector distance and the type of radiation detector used for measurements. These factors should be considered together including economic constraints and regulatory requirements. The high-level design recommendations that can be generally used for any specific product objectives are provided and listed below.

6.3.5.1. The all-empty-to-all-full counts ratio should be optimally maximized when choosing a collimator material

When choosing a material for the collimator, the ratio of the simulated detector counts from a fully-open collimator to a fully-closed collimator is maximized. This is to ensure that minimal photons get detected when the collimator channels are fully closed and to maximize the detection of photons that are supposed to get registered. The system dimensions and mass requirements have to be considered as well when choosing between multiple material candidates with statistically the same all-empty-to-all-full counts ratio. For example, a square collimator with 36 cm width each side weighs 51.5 kg if it was made of tungsten, and 45.6 kg if it was made of lead. The 6-kg difference makes a big difference if portability was one of the product requirements.

6.3.5.2. The collimator channel opening should be maximized

Depending on the application of the product and the resolution requirement, the collimator channel openings should be maximized so that number of measurements and measurement time needed can be minimized. Smaller channel opening size gives higher image resolution (more pixels available to portray the image). Larger number of pixels

requires larger number of measurements to get a resolved image, and therefore needs a longer measurement time. Additionally, smaller channel opening size for channels that are far apart from each other means that there is more shielding material surrounding the channel and this contributes to more scattering to occur. If a counting detector such as a GM detector was used, this would result in higher number of noises in the reconstructed images.

6.3.5.3. Short measurement time requirement should employ minimal number of collimator channels

The resolution of the reconstructed image depends on the number of total pixels available for image production. The total pixels are determined by the number of collimator channels. The larger the number of collimator channels, the higher the reconstructed image resolution will be. Higher resolution requires larger number of measurements, which means larger number of random collimator configurations for the image reconstruction to be meaningful. Unless there is a novel way of switching collimator configurations seamlessly with minimal mechanical movements, aiming for a high-resolution reconstructed image can be disadvantageous and unworthy. Therefore, based on the objectives of the source imaging system, the number of collimator channels should be optimized in such a way that will ensure minimal configurations are adequate without compromising the localization capability associated with the reconstructed image resolution.

6.3.5.4. Large standoff distance application should use spectroscopic detection system

The effect of source-to-detector distance on the reconstructed image was found to be dependent on the type of detector used. The radiation source distance from the detector is to be minimized when using counting detectors, such as GM detectors, to reduce noise pixels due to the higher scattering counts registered at a larger distance. However, the use spectroscopic detectors, which allows for image reconstruction utilizing the photopeak counts, will not suffer from excessive noise pixels in the image. In fact, for a source with a larger surface compared to a point source, such as the simulated uniform disk source with a radius of 10 cm, the larger source-to-detector distance is beneficial in making the multidirectional nature of the gamma source to appear as a monodirectional source traveling straight into the detector. As demonstrated, a radiation source emitting gamma in only one direction towards the detector had less noise pixels in the reconstructed image due to the lower number of undesired scattered photons being detected. The downside that comes with larger source-to-detector distance is the longer measurement time needed to ensure sufficient counts were collected as the intensity of the radiation source drops by square of distance.

6.4. Conclusion

The objective of this paper was to study design factors that affect the performance of a compressed-sensing-based gamma source imaging system. Simulations were performed for the validated model with the aim to reduce its size by substituting water surrounding the collimator with five material candidates. This set up was called test model

1 and simulations of it resulted in lead to be chosen to replace water component, as well as the collimator material. This resulted in a system size reduction by 68%, and this set up was called test model 2.

Simulations were done for test model 2 with varying source-to-detector distances, varying channel pipe radii and varying total numbers of collimator channels. Test model 2 was then modified into test model 3 by reducing the number of GM detectors used from six to one, and changing the collimator opening into a square shape instead of circular. Test model 3 was also simulated with another type of detector, which was a 2”-by-2” sodium iodide (NaI) detector. Comparisons were made between the results from these two different detectors.

Finally, an example of an improved design, inspired by a recently commercialized gamma source imaging system that operates with similar principles was examined with a 5.2”-by-8.3” NaI detector. Image artifacts in terms of noise pixels were found to vary with source-to-detector distance depending on the type of detector being used. With a spectroscopic detector, noise pixels in the reconstructed image were less than those with a counting detector for large source-to-detector distances. This was due to the ability to only record photopeak counts and discount scattered photons. It was also shown that higher image resolution (more collimator channels) will require a greater number of measurements for image reconstruction, hence more measurement time needed.

These results show that the objective of studying the design factors to improve the gamma source imaging system was fulfilled. Collimator material and geometry, number and size of collimator channels, the source-to-detector distance, as well as the detector

type used for measurements are the factors that can be explored to improve the design of the validated proof-of-concept system model for gamma source imaging. These factors were translated into high-level design recommendations for improving any compressed-sensing-based gamma source imaging.

The recommendations are (1) the ratio of all-empty-to-all-full counts from simulations should be optimally maximized when choosing a collimator material, (2) the collimator channel opening should be optimally maximized, (3) short measurement time requirement should employ optimally minimal number of collimator channels, and (4) large standoff distance application should use spectroscopic detection system. These recommendations can be used to develop supporting technologies for nuclear security, which could come in the form of a fixed radiation imaging installation or a portable radiation imaging instrument.

6.5. References

[1] "CORIS360 Online Brochure." Australian Nuclear Science and Technology Organisation (ANSTO), Aug. 2021. Accessed: Sep. 13, 2021. [Online]. Available: https://www.ansto.gov.au/sites/default/files/2021-08/CORIS360-Online-Brochure-Aug2021.pdf

[2] "Nuclear smuggling deals 'thwarted' in Moldova," BBC News, Oct. 07, 2015. Accessed: Sep. 16, 2021. [Online]. Available: https://www.bbc.com/news/world-europe-34461732

[3] "The fuel for a nuclear bomb is in the hands of an unknown black marketeer from Russia, U.S. officials say," Center for Public Integrity.

https://publicintegrity.org/national-security/the-fuel-for-a-nuclear-bomb-is-in-the-hands-of-an-unknown-black-marketeer-from-russia-u-s-officials-say/ (accessed Sep. 16, 2021).

[4] M. AP, "Nuclear smugglers tried selling radioactive materials to ISIS: AP," The Daily Star, Oct. 07, 2015. https://www.thedailystar.net/world/nuclear-smugglers-tried-selling-radioactive-materials-isis-153184 (accessed Sep. 16, 2021).

[5] A. Robertson, "Moldovan security forces smash £150,000 uranium smuggling ring," Mail Online, Jun. 25, 2016. https://www.dailymail.co.uk/news/article-3660111/Moldovan-security-forces-smash-150-000-uranium-smuggling-ring-seizing-imposing-quantity-nuclear-material-raid-gang.html (accessed Sep. 16, 2021).

[6] Internationale Atomenergie-Organisation, Combating illicit trafficking in nuclear and other radioactive material: reference manual. Vienna: Internat. Atomic Energy Agency, 2007.

[7] "IAEA Incident and Trafficiking Database (ITDB): 2020 Fact Sheet." International Atomic Energy Agency (IAEA). [Online]. Available: https://www.iaea.org/sites/default/files/20/02/itdb-factsheet-2020.pdf

[8] H. Al Hamrashdi, S. D. Monk, and D. Cheneler, "Passive Gamma-Ray and Neutron Imaging Systems for National Security and Nuclear Non-Proliferation in Controlled and Uncontrolled Detection Areas: Review of Past and Current Status," Sensors (Basel), vol. 19, no. 11, p. 2638, Jun. 2019, doi: 10.3390/s19112638.

[9] Internationale Atomenergie-Organisation, Ed., Detection of radioactive materials at borders. Vienna: IAEA, 2003.

7. CONCLUSIONS

The main research objective of developing a design concept for CS-based radiation source imaging system was achieved through six milestones. This device was conceptualized through a series of design processes using MCNP simulations. The results showed that an initial rudimentary design of an 11×11 array of PVC pipes placed upright in a water-filled tank and two ^{3}He detectors was feasible for neutron source imaging. MCNP simulation results showed that image quality allowing for neutron source shape identification and localization was obtained with as low as 50% of the total pixels required for the conventional raster scan method. Preliminary experiment measurements were performed by imaging a 3.7 MBq point ^{252}Cf neutron source after a physical system of the MCNP model was built. Due to interference in neutron measurements from another ongoing experiment at the location, it was decided that further study was to be done for gamma sources instead, with GM detectors replacing the ^{3}He detectors.

In order to ensure that the MCNP simulation model works as close as possible to the physical model, a detailed investigation on methods to model the GM detectors was performed. Two ways of estimating counts from GM detectors using MCNP simulations were proposed; by using the F4 tally or the *F4 tally. The counts estimate using F4 tally method was found to resemble the measured counts more closely compared to the *F4 method because the F4 tally results were all within 20% of agreement with the measured counts. The modeling of GM detectors using the proposed F4 method was shown to agree with the measurements, especially in terms of the behavior trends. The F4 method, which

has never been used to model GM detectors before, was then selected as the standard way to simulate the proposed imaging system.

After the simulation of the detector system was examined and validated, the benchmarking of the MCNP model of the proof-of-concept gamma source imaging system with experimental measurements was then performed. The validation was done for four cases with different gamma source locations. The physical set up was tested with an "unknown" source position without any simulation results for comparison. The discrepancy between simulation and experimental results at each configuration was less than a factor of two when compared to the corresponding experiment measurement, except for at most five extreme datapoints (in the above metal case). The localization was successful in both simulations and experiments for all four defined cases, as well as the "unknown" source location in the experiment.

Finally, the design factors that affect the performance of a CS-based gamma source imaging system were studied. The system's size was reduced by 68% as the water surrounding the collimator and the collimator material were substituted with the selected material candidate, lead. Collimator material and geometry, number and size of collimator channels, the source-to-detector distance, as well as the detector type used for measurements are the factors that can be explored to improve the design of the validated model for gamma source imaging. These factors were translated into high-level design recommendations that can be used to develop supporting technologies for nuclear security, which could come in the form of a fixed radiation imaging installation or a portable radiation imaging instrument.

This research of employing CS principles in designing a radiation source imaging system has produced a design concept or a core idea that is still new in the nuclear security field. The proof-of-concept design was demonstrated to perform well in simulations, and was validated with experimental measurements. A set of high-level recommendations was established to serve as guidance for system developers to design a CS-based radiation source imaging system. The importance of this work is that it supports integration of a broader set of tools to counter terrorism and encourages further exploration on the design concept to support nuclear security activities. This research is unique because of the use of the NNLS method for image reconstruction instead of the typical l_1-minimization method used in CS problems. The findings from this research is also significant in offering a relatively cheaper alternative for such imaging system with the use of affordable GM detectors for radiation measurements. It is hoped that this design concept will be further explored so that more design solutions that are relatively cheap will be available. This will hopefully facilitate technology transfer and incentivize involvement by Member States to strengthen current global nuclear security program.

APPENDIX A

AN EXAMPLE OF MCNP INPUT FILE

```
c*********************************************************************
c Rectangular PE tank filled with water with a point source on top of the grid (center),
c 11x11 PVC grid in the middle of the tank - all filled with water,
c each tube's ID is 1.53 cm and OD is 2.155 cm. Each tube has a rubber stopper
c fitted at one end at the bottom of the tank.
c Height of water in the tank is 74 cm.
c*********************************************************************
c Cell Cards
c*********************************************************************
1    0  400 -401 402 -403 302 -203                    fill=1 imp:p=1
10   5 -0.0012 -101 103                                u=2 imp:p=1 $ cylindrical air
11   7 -1.4064 -102 101 202 103                        u=2 imp:p=1 $ PVC shell
12   1 -1 -204 (101:-103) (102:-101:-202:-103) 103     u=2 imp:p=1 $ water
13   5 -0.0012 102 204                                 u=2 imp:p=1 $ air
14   8 -1.1 -103                                       u=2 imp:p=1 $ rubber stopper
20   1 -1 -101 103                                     u=3 imp:p=1 $ cylindrical water
21   7 -1.4064 -102 101 202                            u=3 imp:p=1 $ PVC shell
22   1 -1 (102 -204 103):(-202 101 103)                u=3 imp:p=1 $ water
23   5 -0.0012 102 204                                 u=3 imp:p=1 $ air
15   8 -1.1 -103                                       u=3 imp:p=1 $ rubber stopper
2    0  500 -501 502 -503 -203 302                     lat=1 u=1 imp:p=1
     fill=-5:5 -5:5 0:0
C Start Modifications
     2 3 2 2 2 3 3 3 3 2 2
     2 2 3 3 2 3 3 3 3 2 3
     3 2 3 2 2 3 3 3 3 3 3
     3 3 3 2 3 2 2 3 3 2 2
     3 2 2 2 2 3 3 2 2 3 3
     2 2 2 3 3 2 2 3 3 3 3
     3 3 2 3 2 2 3 2 3 3 2
     2 2 3 2 2 2 3 2 2 2 2
     2 2 3 3 3 2 2 2 2 2 3
     2 3 2 3 3 2 2 3 3 3 2
     2 2 2 3 3 2 2 3 2 2 2
C End Modifications
4    9 -8 611 -612                                    imp:p=1 $ horizontal cage bars
41   like 4 but trcl=(0 0 19.05)                      imp:p=1 $ parallel to x
42   like 4 but trcl=(0 0 38.1)                       imp:p=1
43   like 4 but trcl=(0 0 59.69)                      imp:p=1
44   like 4 but trcl=(0 102.2 0)                      imp:p=1
45   like 4 but trcl=(0 102.2 19.05)                  imp:p=1
46   like 4 but trcl=(0 102.2 38.1)                   imp:p=1
47   like 4 but trcl=(0 102.2 59.69)                  imp:p=1
6    9 -8 613 -614                                    imp:p=1 $ parallel to y
61   like 6 but trcl=(0 0 19.05)                      imp:p=1
62   like 6 but trcl=(0 0 38.1)                       imp:p=1
63   like 6 but trcl=(0 0 59.69)                      imp:p=1
64   like 6 but trcl=(121.2 0 0)                      imp:p=1
```

```
65   like 6 but trcl=(121.2 0 19.05)              imp:p=1
66   like 6 but trcl=(121.2 0 38.1)               imp:p=1
67   like 6 but trcl=(121.2 0 59.69)              imp:p=1
3    9 -8 615 -616                                imp:p=1 $ vertical cage bars
301  like 3 but trcl=(-15.875 0 0)                imp:p=1 $ along x
302  like 3 but trcl=(-36.83 0 0)                 imp:p=1
303  like 3 but trcl=(17.78 0 0)                  imp:p=1
304  like 3 but trcl=(33.655 0 0)                 imp:p=1
305  like 3 but trcl=(54.61 0 0)                  imp:p=1
306  like 3 but trcl=(0 105.82 0)                 imp:p=1
307  like 3 but trcl=(-15.875 105.82 0)           imp:p=1
308  like 3 but trcl=(-36.83 105.82 0)            imp:p=1
309  like 3 but trcl=(17.78 105.82 0)             imp:p=1
310  like 3 but trcl=(33.655 105.82 0)            imp:p=1
311  like 3 but trcl=(54.61 105.82 0)             imp:p=1
312  like 3 but trcl=(71.3 17.94 0)               imp:p=1 $ along y vertical
313  like 3 but trcl=(71.3 32.545 0)              imp:p=1 $ right
314  like 3 but trcl=(71.3 73.185 0)              imp:p=1
315  like 3 but trcl=(71.3 87.79 0)               imp:p=1
316  like 3 but trcl=(-53.55 17.94 0)             imp:p=1 $ left
317  like 3 but trcl=(-53.55 38.895 0)            imp:p=1
318  like 3 but trcl=(-53.55 66.835 0)            imp:p=1
319  like 3 but trcl=(-53.55 87.79 0)             imp:p=1
5    1 -1  -201 #1                                imp:p=1 $ water
7    6 -0.93 -301 201 309 #1                      imp:p=1 $ tank
30   9 -8 -600                                    imp:p=1 $ metal cage base
31   2 -2.3 -404                                  imp:p=1 $ concrete floor
33   4 -0.000839 -800          vol=150.49         imp:p=1 $ GM volume filled with neon
34   like 33 but trcl=(15.2 0 0)                  imp:p=1 $ GM
37   like 33 but trcl*=(-2.0 -2.9 0 45 45 90 135 45 90 90 90 0)    imp:p=1 $ GM
38   like 33 but trcl*=(-2.0 2.9 0 45 135 90 45 45 90 90 90 0)     imp:p=1 $ GM
39   like 33 but trcl*=(2.0 2.9 0 135 135 90 45 135 90 90 90 0)    imp:p=1 $ GM
40   like 33 but trcl*=(2.0 -2.9 0 135 45 90 135 135 90 90 90 0)   imp:p=1 $ GM
51   3 -2.7 800 -801           vol=25.587                          imp:p=1 $ GM Al case
52   like 51 but trcl=(15.2 0 0)                                   imp:p=1 $ GM Al case
53   like 51 but trcl*=(-2.0 -2.9 0 45 45 90 135 45 90 90 90 0)    imp:p=1 $ GM case
54   like 51 but trcl*=(-2.0 2.9 0 45 135 90 45 45 90 90 90 0)     imp:p=1 $ GM case
55   like 51 but trcl*=(2.0 2.9 0 135 135 90 45 135 90 90 90 0)    imp:p=1 $ GM case
56   like 51 but trcl*=(2.0 -2.9 0 135 45 90 135 135 90 90 90 0)   imp:p=1 $ GM case
8    5 -0.0012 -700 404 (-309:301) 600 #1
     #4 #41 #42 #43 #44 #45 #46 #47 #52 #53
     #6 #61 #62 #63 #64 #65 #66 #67 #54 #55 #56
     #3 #301 #302 #303 #304 #305 #306 #307 #308
     #309 #310 #311 #312 #313 #314 #315 #316
     #317 #318 #319 #33 #34 #37 #38 #39 #40 #51                    imp:p=1 $ air
99   0  700                                                        imp:p=0 $ kill zone

c*********************************************************************
c Surface Cards
c*********************************************************************
101  CZ  0.765                                  $ PVC inner radius (air)
102  CZ  1.0775                                 $ PVC outer radius (shell)
103  TRC 0 0 0.3  0 0 2.635 .9625 0.709         $ Rubber stopper
```

```
201  RPP -59.39 59.39 -49.865 49.865 0.3 74.3        $ Water
202  PZ  2.35                                        $ Bottom of pipe grid
203  PZ  108.94                                      $ Top of the pipe grid
204  PZ  74.3                                        $ Water height
301  RPP -59.69 59.69 -50.165 50.165 0 89.535        $ Tank, thickness = 0.3 cm
302  PZ  0.3
303  PZ  0
304  PZ  89.535
305  PX  -57.97
306  PX  57.97
307  PY  -48.445
308  PY  48.445
309  RPP -59.39 59.39 -49.865 49.865 74.3 89.535
400  PX -11.99
401  PX  11.99
402  PY -11.99
403  PY  11.99
404  RPP -200 200 -200 200 -70 -10.4                 $ Concrete floor
500  PX -1.09                                        $ Parallelepiped for grid
501  PX  1.09
502  PY -1.09
503  PY  1.09
600  RPP -60.59 60.59 -51.065 51.065 -0.12 0         $ Metal cage base
611  RCC -61.59 -51.1 0.9 122.98 0 0 0.73            $ Parallel to x
612  RCC -61.59 -51.1 0.9 122.98 0 0 0.9
613  RCC -60.6 -50.165 0.9 0 100.33 0 0.73           $ Parallel to y
614  RCC -60.6 -50.165 0.9 0 100.33 0 0.9
615  RCC -8.89 -52.91 0 0 0 61.5 0.73                $ Vertical third left front
616  RCC -8.89 -52.91 0 0 0 61.5 0.9
800  RCC -14.2 0 -8.3 13.2 0 0 1.905                 $ GM length=13.2 cm
801  RCC -14.2 0 -8.3 13.2 0 0 2.0606                $ Al case 0.06125 in (0.15558 cm)
700  RPP -200 200 -200 200 -70 250                   $ Kill zone

c*********************************************************************
c Data Cards
c*********************************************************************
MODE p                          $ Photon problem
nps 20000000                    $ Run number of particle histories
c~~~~~~~~~~~~~~~~~~~~~~~~~~~~~~~~~~~~~~~~~~~~~~~~~~~~~~~~~~~~~~~~~~~~~~~
c Source definition
c~~~~~~~~~~~~~~~~~~~~~~~~~~~~~~~~~~~~~~~~~~~~~~~~~~~~~~~~~~~~~~~~~~~~~~~
SDEF ERG=0.662 POS=0 0 109 VEC= 0 0 -1 PAR=2 DIR=d2  WGT=2 $ Cs-137 discrete PS
SI2 -1 0 1
SP2 0 0.5 0.5
SB2 0 0 1
c~~~~~~~~~~~~~~~~~~~~~~~~~~~~~~~~~~~~~~~~~~~~~~~~~~~~~~~~~~~~~~~~~~~~~~~
c Materials
c~~~~~~~~~~~~~~~~~~~~~~~~~~~~~~~~~~~~~~~~~~~~~~~~~~~~~~~~~~~~~~~~~~~~~~~
m1   1000 0.66667 8000 0.33333                       $ Water using atomic fractions
m2   1000  0.168038 8000  0.563183 11000 0.021365   $ (Regular) Concrete floor
     13000 0.021343 14000 0.203231 20000 0.018595
     26000 0.004246
m5   7014 0.7843 8016 0.2109 6000 0.0001             $ Air with N, O, C atomic fractions
```

```
m4   10000 1                                        $ Neon NTP,rho = 0.000839 g/cm3
m6   1000 0.6667 6000 0.33333                       $ PE Rubbermaid bin with H,C atomic fractions
m7   1000 0.499995 6000 0.33334 17000 0.166665     $ PVC with H, C Cl atomic fractions
m8   1000 0.666653 6000 0.333347                    $ EPDM rubber stopper (Rubber butyl)
m9   6000 0.006356 14000 0.018057 24000 0.188773
     25055 0.018462 26000 0.683520 28000 0.083616    $ Stainless steel 304
m3   12000 0.011162 13000 0.977325 14000 0.005796  $ Aluminum alloy 6061
     22000 0.000499 24000 0.001017 25000 0.000435
     26000 0.001987 29000 0.001174 30000 0.000606
     30000 0.000606
c~~~~~~~~~~~~~~~~~~~~~~~~~~~~~~~~~~~~~~~~~~~~~~~~~~~~~~~~~~~~~~~~~~~~~~~~~~~~~~~~~~~~~~~~~~~~
c Tallies
c~~~~~~~~~~~~~~~~~~~~~~~~~~~~~~~~~~~~~~~~~~~~~~~~~~~~~~~~~~~~~~~~~~~~~~~~~~~~~~~~~~~~~~~~~~~~
F4:p 33 34 37 38 39 40                  $ Gammas through GM volume
*F14:p 33 34 37 38 39 40
FM4  2.815e13                           $ Gammas per second per 400 uCi (BR 85%)
FM14  1.258e7
DE4  log 0.01   0.03   0.05   0.07   0.1     0.15   0.2     0.25
       0.3    0.35   0.4    0.45   0.5     0.55   0.6     0.65
       0.7    0.8    1.0    1.4    1.8     2.2    2.6     2.8
       3.25   3.75   4.25   4.75   5.0     5.25   5.75    6.25
       6.75   7.5    9.0    11.0   13.0    15.0
DF4  log 3.96E-06 5.82E-07 2.90E-07 2.58E-07 2.83E-07 3.79E-07 5.01E-07
       6.31E-07 7.59E-07 8.78E-07 9.85E-07 1.08E-06 1.17E-06 1.27E-06
       1.36E-06 1.44E-06 1.52E-06 1.68E-06 1.98E-06 2.51E-06 2.99E-06
       3.42E-06 3.82E-06 4.01E-06 4.41E-06 4.83E-06 5.23E-06 5.60E-06
       5.80E-06 6.01E-06 6.37E-06 6.74E-06 7.11E-06 7.66E-06 8.77E-06
       1.03E-05 1.18E-05 1.33E-05
```

APPENDIX B

AN EXAMPLE OF IMAGE RECONSTRUCTION CODE

```
% Written by: Justin Romberg, Caltech
% Email: jrom@acm.caltech.edu
% Created: October 2005
% Modified by: Linda Anuar
% Modified: Nov 15, 2020

clear
clc

path(path, './Optimization');
path(path, './Measurements');
path(path, './Data');

load b7 % .mat file containing count readings
load A4 % .mat file containing the collimator configuration matrix
% --------------------------------
% Specify the data to be used for A matrix
% (each row represents each map)
% -> A(from row #:to row #, from column #: to column #)
% Specify the data to be used for b matrix
% (row # represents measurement using map #)
% -> b(from row #:to row #, from column #: to column #)
% b column for gamma sims
% 1: Simulation case 1 ANSI
% 2: Simulation case 2 ANSI
% 3: Simulation case 3 ANSI
% 4: Simulation case 4 ANSI
% 5: Experiment case 1
% 6: Experiment case 2
% 7: Experiment case 3
% 8: Experiment case 4
% 9: Experiment case 5 - unknown
% --------------------------------

At = [];
n = 11;
N = n*n;
c = 50;  % cases 1,2,4 c = 50, case 3 c = 40
m = 55;  % cases 1,2,4 c = 55, case 3 c = 46
p = 1;   % (Sim) put the corresponding b column #
q = p+4; % (Exp) put the corresponding b column #
time0 = clock;
u = 1;

% set i to be the number of images to plot
for i = 1:10
    b0{i} = b7(c:m,p:p);
    btd{i} = b7(c:m,q:q);
```

```
    tic;
    x1{i} = lsqnonneg(A4(c:m,1:N),b0{i},optimset('Display','notify'));
    xtd{i} =lsqnonneg(A4(c:m,1:N),btd{i},optimset('Display','notify'));
    toc;

    I1{i} = reshape(x1{i}, n, n);
    I1{i} = imrotate(I1{i}/max(max(I1{i})), 270);
    I{i} = reshape(xtd{i}, n, n);
    I{i} = imrotate(I{i}/max(max(I{i})), 270);

    subplot(2,10,u),imagesc(I1{i},[0 1]), title(['Sims, m =
',num2str(m-c+1)])
    subplot(2,10,u+10),imagesc(I{i}, [0 1]), title(['Exp, m =
',num2str(m-c+1
    u = u + 1;
    m = m + 5; %for cases 1,2,4 m=m+5, case 3 m=m+6
end
```